Drying of Multiphase Single Droplets in Ultrasonic Levitator

Vom Fachbereich Maschinenbau
an der Technischen Universität Darmstadt
zur
Erlangung des Grades eines Doktor-Ingenieurs
(Dr.-Ing.)
genehmigte

Dissertation

vorgelegt von

M. Sc. Belal Ali Al Zaitone

aus Souf, Jordanien

Berichterstatter:	Prof. Dr.-Ing. C. Tropea
Mitberichterstatter:	Prof. Dr.-Ing. P. Stephan
Tag der Einreichung:	01. March 2009
Tag der mündlichen Prüfung:	20. May 2009

Darmstadt, 2009

D17

For my mother and father with love and gratitude

Acknowledgments

The present research work has been conducted at Chair of Fluid Mechanics and Aerodynamics, *Technische Universität Darmstadt* between August 2005 and February 2009.

First of all I would like to take this opportunity to express my heartfelt thanks and appreciation to my advisor Prof. Dr.-Ing. C. Tropea for his invaluable guidance, encouragement, and patience. The confidence he offered me beside his inspiring ideas provided a great opportunity to develop my research skills and gain experience in experimental work.

I want to thank Prof. Dr.-Ing. P. Stephan, Chair of Technical Thermodynamics, Technische Universität Darmstadt, for his prompt willingness to review this dissertation.

The financial support of *Deutsche Forschungsgemeinschaft* "DFG" through the Graduiertenkolleg "*Optische Messtechniken für die Charakterisierung von Transportprozessen an Grenzflächen*" (GRK1114) is gratefully acknowledged. I would like also to thank Prof. Dr.-Ing. Nils Damaschke, Christian Heinisch, Frau Monika Medina and Karl Wunderle for their support and the cooperation within GRK1114.

I am grateful to Dr. Guillaume Castanet for his assistance during the first year of my doctoral research; I admire his help, motivation and illuminating instructions. I am more than grateful for Prof. A. Yarin for the fruitful discussions, advice and his significant help.

I would like to thank Dr. Bruno Frackowiak for his suggestions and contribution that definitely helped me to advance my work. I owe special thanks for Dr. Hubert Marschall for his help and being ready to answer my questions.

I would like also to thank other colleagues Nils van Hinsberg, Andreas Lembach, Lars Opfer and Erika Saffer for their help. I would like also to thank Mrs. S. Lath and Ms. S. Wallenr for the arrangement of many administrative matters.

I would like to thank my friends. Especially the people I have met while in graduate school either in Erlangen or Darmstadt, who have become my closest and dearest friends, their support to this work is not insignificant, and to all I give my love and thanks.

I would like to end by thanking my dearest family. My parents have always inspired me and helped me reach my goals. I owe them everything and I wish I could show them just how much I love and appreciate them. I hope that this work make them proud.

Darmstadt, February 2009 Belal Ali Al Zaitone

Abstract

Spray drying is widely used in many industries, e.g. chemical, food and pharmaceutical processing, in which the spray generation is followed by solvent/liquid evaporation leading to a final powder product.

As the liquid component evaporates, the droplet weight decreases. This evaporation process is accompanied by phase change of the volatile component. For a multiphase droplet, solid material is suspended or dissolved in the liquid phase. In such cases, it is important to have knowledge of transport phenomena for single droplets as it pertains to their evaporation and component distribution.

The investigation of the evaporation of single droplets is particularly applicable to the study of spray drying and atomization. There are several different measurement techniques that can be used to analyze droplets of various components such as pure liquids, mixtures, solutions, and colloidal suspensions.

The principle of ultrasonic levitation is unique in that it allows the isolation of a single droplet in space rather than a myriad of droplets. Having a multiphase droplet suspended in the acoustic field facilitates the study of the drying rate at different operational parameters, and tracking the morphological changes during the course of the drying process.

The experiments conducted in this work were performed for a single droplet or separation of two single droplets. Single droplet analysis allows for characterization of the droplets drying rate. The multi-droplet analysis is pertinent to sound pressure level calibration.

Understanding the sub-models for these processes is largely beneficial to the advance of modeling the overall spray drying process.

In the present work, the drying of further example systems has been studied, and a characterization of the outer crust formed at the end of the first drying stage is presented. These are accompanied by "quasi" 2-D model formulations for the simulation of individual drop drying to describe the solid concentration profiles and the creation of the crust at the end of the constant rate period, when the solids concentration at the surface exceed the saturation concentration.

Zusammenfassung

Schwerpunkte der vorliegenden Arbeit, die im Rahmen des Graduiertenkollegs GRK 1114 "Optische Messtechniken für die Charakterisierung von Transportprozessen an Grenzflächen" durchgeführt wurde, waren Untersuchungen über die Trocknung von mehrphasigen Tropfen, wie sie in der Sprühtrocknung vorkommen. Dabei wurden die Trocknungsrate und die Morphologie des getrockneten Pulvers im Detail untersucht. Die Arbeit beinhaltet sowohl experimentelle Untersuchungen wie auch eine mathematische Modellierungen der beobachteten Vorgänge.

Technische Prozesse wie das Sprühtrocknen sind weit verbreitet in der Chemischen, Lebensmittel- oder Pharmazeutischen Industrie. Hierbei werden die Flüssigkeiten mit gelösten Feststoffen in das Gas gesprüht. Verdunstet die flüssige Komponente, verringert sich die Tropfenmasse. Dieser Verdunstungsprozess wird begleitet von einem Phasenwechsel der flüchtigen Komponente. Für einen Mehrphasentropfen wird festes Material in einer flüssigen Phase suspendiert.

In diesen Fällen ist es wichtig, die Transportphänomene der einzelnen Tropfen zeitabhängig zu kennen, insbesondere die Verdunstung und Verteilung der Komponenten.

Im Vordergrund der experimentellen Arbeiten stand daher das Trocknen einzelner Tropfen in einem akustischen Levitator, der eine berührungslose Fixierung des Tropfens ermöglicht. Aus Beobachtungen an einzelnen Tropfen könnten dann Sub-Modelle für die Verdunstung und Verteilung der Tropfenkomponenten mit der Zeit aufgestellt werden, nicht nur für reine Flüssigkeitstropfen sondern auch für komplexere Tropfen wie Suspensionen oder Emulsionen.

In den Experimenten wurden auch zum Teil zwei getrennte Tropfen gleichzeitig im Levitator beobachtet. Somit konnte auch der veränderliche Schalldruck online gemessen und in der Auswertung berücksichtigt werden.

In der vorliegenden Arbeit werd die Trocknung weiterer Beispielsysteme mit untersucht und die Charakterisierung der äußeren Kruste dargestellt. Hierfür wird ein "quasi" 2-D Trocknungs-Model formuliert, mit dem die Konzentrationsprofile und die Bildung der Kruste am Ende der konstanten Trocknungsperiode abgebildet werden konnten.

Contents

Nomenclature

Symbol	Description	Unit
Latin Letters		
a_t	Droplet radius at time, t	m
a_w	Activity coefficient	-
A_{0e}	Amplitude of incident sound wave	dyn/cm^2
B	Gas particle velocity	m/s
B_M	Spalding mass transfer coefficient	-
B_T	Spalding heat transfer coefficient	-
c_0	Sound speed	m/s
C_P	Specific heat	$kJ/(kg \cdot K)$
C_w	Liquid mass fraction	-
C_s	Solid mass fraction	-
D	Droplet diameter	m
D_{core}	Diameter of the core	m
d_{nozzle}	Nozzle diameter	m
F	Correction factor	-
f	frequency	s^{-1}
F_{ac}	Acoustic force	N
F_{drop}	Droplet weight	N
F_r	Radial acoustic force	N

g	Gravity acceleration constant	m^2/s
h_T	Heat transfer coefficient	$W/(m^2 \cdot K)$
k	Wave number	m^{-1}
K_g	Mass transfer coefficient in gas phase	m/s
K_L	Constance of the drying model	$kg/(m \cdot s)$
K_{crust}	Crust mass transfer coefficient	m/s
K_{gc}	Overall mass transfer coefficient	m/s
L	Length of standing wave	m
L_R	Distance between reflector and transducer	m
L_v	Latent heat of vaporization	J/kg
L_x	Distance between two adjacent nodes	m
$\dot{m}$	Mass flow rate	kg/s
$\dot{m}_v$	Vapor mass flow	kg/s
m_s	Mass of the solids	kg
m_t	Mass of the droplet at time, t	kg
$m_{s,core}$	Mass of the solids in the core	kg
$m_{s,crust}$	Mass of the solids in the crust	kg
P	Sound pressure	N/m^2
P^v	Vapor pressure	N/m^2
P_i'	Incident pressure	N/m^2
P_s'	Scattered pressure	N/m^2
Q_C	Convective heat flux	W
Q_L	Heat flux entering into droplet	W
Q_{vap}	Heat flux due to liquid vaporization	W
R	Universal gas constant	$J \cdot K^{-1} \cdot mol^-1$
r	Droplet radius	m
SPL	Sound pressure level	dB
T	Temperature	K or °C
t	Time	s
t^*	Total time to evaporate the liquid	s
u_{ac}	Inner acoustic streaming velocity	m/s

$\dot{V}$	Air flow rate	l/min
V	Air velocity	m/s
V_r	Radial bulk velocity	m/s
v_c	Volume of the crust	m^3
x	Vertical coordinate in the acoustic field	m
X_{liquid}	Mole fraction of liquid	-
$\hat{Y}$	Density ratio	-
y_w	Mass fraction of water	-
Y_{vap}	Mass fraction of vapor	-

Greek Letters

α	Surface tension	N/m
α_d	Thermal diffusivity of the droplet	m^2/s
α_g	Thermal diffusivity of the gas	m^2/s
β	Evaporation rate coefficient	m^2/s
Δ	Difference	-
δ	Boundary layer thickness	m
$\mathscr{D}$	Binary diffusion coefficient	m^2/s
δ_{porous}	Thickness of porous crust	m
ε	Porosity of the crust	-
ϕ	Azimuthal angle	rad
κ	Surface curvature	m^{-1}
λ	Wave length	m
λ_g	Thermal conductivity	$W/(m \cdot K)$
μ_0	Gas viscosity	$Pa \cdot s$
ω	Angular frequency	s^{-1}
ξ	Dimensionless radial coordinate	-
θ	Polar angle	rad
ρ	Density	kg/m^3

Subscripts

0	initial
ac	acoustic field
c	concentration
d	droplet
g	gas
liq	liquid
ref	reference
s	surface
sat	saturation
sol	solution
T	Temperature, Thermal
vap	vapor
w	water

Dimensionless numbers

Bi	Biot number, relates the heat transfer resistance inside and at the surface of a droplet.	-
Gr	Grashof number, ratio of the buoyancy to viscous forces.	-
Le	Lewis number, ratio of thermal diffusivity to mass diffusivity.	-
Nu	Nusselt number, ratio of convective to conductive heat transfer across the boundary.	-
Pe	Peclet number, the ratio of the convective to diffusive flow.	-
Pr	Prandtl number, ratio of momentum diffusivity to thermal diffusivity.	-

Re	Reynolds number, ratio of inertial to viscous forces.	-
Sc	Schmidt number, ratio of momentum diffusivity to mass diffusivity.	-
Sh	Sherwood number, ratio of convective to diffusive mass transport.	-

Chapter 1

Introduction

Spray drying is an essential unit operation widely used in many industries involving particle formation and dry powder production. The principle step in the process of spray drying is to generate droplets of very small size. A large surface area is created to accomplish maximum mass and heat flux and to mix the solution with drying air. *Drying* may thus be defined as the removal of volatile substances from a mixture that yields a solid product (Keey, 1972). Compared to other evaporation process, spray drying has a great advantage that products can be dried without much loss of thermal sensitive compounds i.e. proteins or volatile compounds like aromas; this is especially important in the production of food products such as milk powder or instant coffee (Schuck, 2002).

The capability of spray dryers to handle different types of materials i.e. solution, slurry, paste, gel or suspension, make it the prime industrial unit in many fields e.g. chemical, food, polymer, ceramics and pharmaceutical processing (Mujumdar, 2006, Adhikari et al., 2000).

Spray drying is an ideal process where the end product must comply with precise standards regarding particle size distribution, residual moisture content, bulk density and particle morphology.

The knowledge of the drying kinetics and improvement of the basic understanding of heat and mass transfer is very important for the optimization of spray drying designs. An approach called particle engineering, which is the control of particle size and morphology (Vehring, 2007) is becoming increasingly important in pharmaceuti-

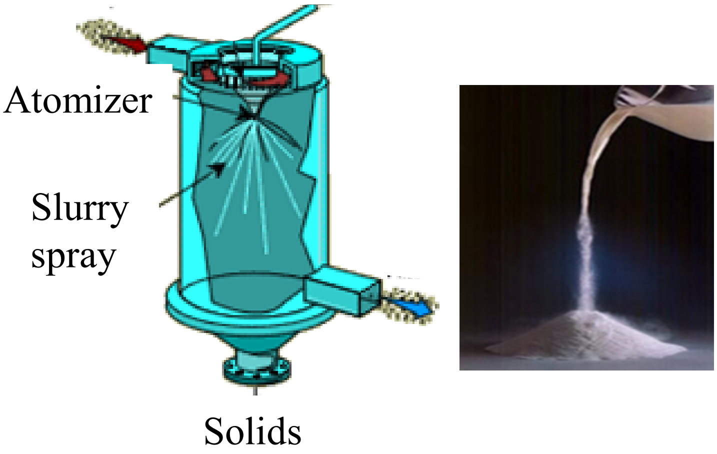

Figure 1.1: Sketch of typical spray dryer.

cal production and development of new products.

An example of this process is the creation of drug delivery particles absorbed by the body through inhalation into the lungs; such particles should be low density to follow the flow streams, on the other hand, they should be large enough to deposit on the surface i.e. porous particles. Spray drying is used in the production of such specifically designed particles.

The entire spray process consists of multiple physical phenomena: primary atomization, spray transport and wall interactions, as well as single droplet processes, i.e. evaporation and heating during spray transport. Through the stochastic nature of the atomization process droplets of various sizes are formed. Because of many difficulties that may be encountered during investigations of spray drying, researchers tend to split these sub-processes into smaller research areas; however, the drying period remains the most important step that influences the end product properties.

Since in-situ investigations inside the spray dryer are very difficult to achieve, studying and theoretically describing the entire drying process of a *single droplet* is of high interest. The acoustic levitator offers a unique method in which a multiphase droplet can be suspended in a controlled environment similar to the operational parameters in spray drying. The observation of a single droplet upon drying enables researchers to track all the physical and morphological changes, this is extremely difficult to realize in a bulk of droplets, i.e. in the spray dryer.

The aim of this research can be summarized as follows:

- Design an experimental facility consisting of an acoustic levitator and other auxiliary units to investigate the drying of multiphase droplets.
- Implement different optical measurement techniques (CCD camera, light illumination and PIV) to measure the size of the droplets and the streaming flow around the droplet.
- Examine the evaporation of pure liquid droplets in order to characterize the experimental device, and compare the results with the existing models for the sake of validation.
- Investigate the drying of different materials e.g. solutions or suspension to study the drying kinetic, and developing a mathematical model to predict the drying kinetic of such materials at various operational parameters.

Thesis outline

The thesis consists of 7 chapters, a review of the previous studies and investigations on the experimental techniques used in the drying of single droplets. First mathematical models on the drying kinetics were reviewed with the emphasis on the studies on single droplet drying models.

In Chapter 3, the basic theory principle of the acoustic levitaion is presented, as well as the characterization of the acoustic levitator to validate the evaporation of pure liquid droplets.

In Chapter 4, the experimental results of pure liquid evaporation are studied and validated with the D^2-law model, further experiments of droplet evaporation attached to glass filament are compared also to the evaporation in the acoustic field.

In Chapter 5, the drying of single multiphase droplet is shown, different process parameters have been investigated to study their influence on the drying kinetics and the formation of the dried particle. In Chapter 6, 1-D and 2-D models are formulated to calculate the solid concentration profiles and to predicts the effect of crust formation on the evaporation of the liquid component.

Finally, in Chapter 7, conclusions and the future perspectives are outlined.

Chapter 2

Literature Review

There has been numerous studies published on both modeling and drying of single droplets. Many experimental techniques and devices are being used to study drying kinetics of single droplets; they can be classified according to the drying material used i.e. pure liquid or multiphase droplets. Wilms (2005) investigated the evaporation of multicomponent single droplet suspended by optical laser beam. However, this technique is suitable only for transparent droplets. Droplets can be suspended by other means, such as by a glass filament (Ranz and Marshall (1952a), Charlesworth and Marshall (1960), Lin and Chen (2002), Chen and Lin (2004)). The droplet mass change is measured by the deflection of a long, thin glass filament and a droplet up to few millimeters can be suspended. Some disturbing effects are introduced, such as the lack of free rotation, bubble formation or heat conducted between the droplet and the filament. Audu and Jeffreys (1975) conduct experiments using a nozzle to fix the droplet against the incoming air flow. In these experiments, the nozzle diameter is comparable to the droplet size, which results in a significant influence to the flow pattern around the droplet. The large surface area contact between the nozzle and the droplet makes the heat conducted into droplet to be substantial.

Single particle drying kinetics can also be determined by using a Falling-Drop dryer (El-Sayed et al., 1990, Seydel et al., 2004, Vehring et al., 2007) , which is also called a mono-dispersed dryer. This technique attempts to mimic spray drying of free falling droplets. A hot gas stream flows upwards, and normally a vibrating orifice generator is used to inject droplets into this stream. The droplet generation is capable of producing droplets of defined size and spacing. The disadvantage of this technique is the possibility of droplet collisions, which may influence the drying rate of each single droplet. Furthermore, the droplets are not stationary in a lab-fixed system, making measurement difficult. A high-speed camera is required to record images of the droplets, thus, diameter or morphological changes can be monitored.

Suspending a droplet in a container-less device by means of an ultrasound field has been already implemented by many researchers. (Furuta et al., 1982, Moeser et al., 2001, Kastner et al., 2000, Tuckermann, 2002, Yarin et al., 2002b, Schiffter, 2005, Zaitone et al., 2006, 2008), in this technique, mechanical intrusion used to suspend the droplet is eliminated, Kastner et al. (2000) calculated the drying kinetics in the second drying stage. The force balance between the acoustic force and droplet weight provided knowledge about the mass loss of the solvent. Recently, Schiffter and Lee (2007a) also used such an ultrasonic levitator to study the drying of a pharmaceutical relevant solute. They investigated the drying of Maltdroxin and aqueous Mannitol to investigate the morphology of the dried particles as function of the operating parameters, temperature, solute concentration and humidity. The acoustic levitator is used to suspend the droplets in the upward air stream.

Spray drying techniques may produce fully filled or hollow particles, depending on the specific operating conditions. Hollow particles provide a means to tailor the manufacturing of low density materials e.g. for applications in drug delivery in lungs where they improve dispersibility and efficiency by lowering the aerodynamic diameter of the particles (Vehring, 2007). Hollow particles form when the evaporation rate is sufficiently high i.e at high temperatures, which leads to an evaporation rate much faster than solute diffusion inside the droplets. Therefore, a high solute concentration gradient develops within the droplet, which results in the formation of hollow particles (Eslamian et al., 2006). Lin and Gentry (2003) reported different methods that lead to solid particle formation, such as nuclei-free environment, using materials of high solubility, low drying rates, lower diffusivity in the solvent and higher solution viscosity. For hollow particle formation, a rapid drying of solution or the decomposition of a gaseous blowing agent trapped in the center of the particle, produces a hollow core. Sano and Keey (1982) developed a model to predict hollow particle formation when a gas bubble formed inside the droplet. Shabde et al. (2005) studied the formation of micro-hollow particles of polymer-like material. They developed a physics-based model of the process to determine the best or optimum operating conditions that will produce hollow particles with desirable properties. Vehring et al. (2007) investigated theoretically and experimentally the drying of terahols and different proteins particles. Two dimensional values were taken into account to study the formation of solid and hollow particles; the Peclet number and the initial saturation of the solute. Large Peclet numbers cause an enrichment of the solute at the surface, which likely leads to shell or skin formation, and if the evaporation rate is high enough, a hollow particle will formed.

Attempts have been made in the last few decades to develop models and to investigate the drying kinetics of single droplets containing either insoluble or dissolved particles and to predict the mass change, morphology, crust formation and temperature history.

Based on such models the development and improvement of the spray drying equipment, as well as the prediction and control of the end product quality, can be carried out more rapidly and economically (Verdurmen et al., 2004). Simulations are generally based on observations from isolated droplets and assuming spherical symmetry (Sirignano, 1999).

The drying process can be divided into two stages (Charlesworth and Marshall, 1960, Nonhebel and Moss, 1971, Kastner et al., 2001). During the first stage, the droplet experiences constant rate drying, where the solvent evaporation rate form the droplet surface is similar to an equally sized pure liquid droplet i.e follows the well-known D^2-law.

However, the presence of solid in the liquid phase will influence the properties of the liquid surface, leading to a decrease in the evaporation rate. Often this stage is called also the wet-bulb drying period, as the surface of the droplet tends to have constant wet-bulb temperature, assuming constant drying conditions i.e gas velocity, humidity and temperature (Nonhebel and Moss, 1971, Farid, 2003).

The size of the droplet will continue to decrease until the solids helps the droplet to maintain a fixed rigid shape. When this occurs the second stage of drying begins. The second stage is called falling rate drying, the mass transfer rate changes drastically

Table 2.1: Single droplet experiments (Adhikari et al., 2000, Lin and Gentry, 2003, Lin and Chen, 2002)

Investigator	levitation method	Drop size	Temperature Re/velocity	Materials
(Frössling, 1938)	-	0.1 - 2 mm	Re= 2-1300	Distilled water
(Ranz and Marshall, 1952a,b)	glass filament	0.6-11 mm	Air at 22-85 °C, 300 cm/s	NaCl, NH_4NO_3
(Charlesworth and Marshall, 1960)	glass filament	1.3-1.8 mm	Air at 31-159°C, 39-157 cm/s	Sodium sulfate, potassium sulfate, ammonium nitrate, calcium chloride, and coffee extract
(Audu and Jeffreys, 1975)	Nozzel 1.6 mm	1-30 mm	Air at 26 -118 °C	water, Sodium sulfate
(Miura et al., 1977)	Floating droplet in an ascending air current	2.9-3.3 mm	7.5-9 m/s	Distilled water
(Furuta et al., 1982)	acoustic levitation	0.9-1.0 mm	0.6-1.99 m/s	NH_4Cl, $(NH_4)_2SO_4$, NH_4NO_3, and $(NH_2)_2CO$
(Sano and Keey, 1982)	glass filament	1.9 mm	100-160 cm/s	Skim milk
(Cheong et al., 1986)	Annealed glass, d = 80-100 μm	1.0-1.5 mm	Air at 20-78 1 cm/s	Slurries of sodium sulfate decahydrate
(El-Sayed et al., 1990)	Annealed glass, d = 80-100 μm	1.4-1.5 mm	Air at 25-250 10 cm/s	Sucrose, maltodextrin, coffee extract, skim milk
(Sunkel and King, 1993)	Flexible silica capillary hollow fiber	0.5-1.8 mm	Nitrogen at 18 °C1.0 l/min	maltodextrin, coffee extract, non-fat milk
(Chen and Xie, 1997)	glass Filament	0.5-1.8 mm	Air at 50-90 °C, 70 m/s	skim milk
(Kastner, 2001)	Acoustic levitator	0.5-2 mm	Air at 30-70 °C, 0.0-1.4 m/s	water, Skim milk, suspension of glass particles in water
(Sckuhr, 2001)	Acoustic levitator	0.5-2 mm	0.0-1.4 m/s	Butylglykol
(Seydel et al., 2004)	Vertical pipe, single droplet generator	270-550 μm	Air up to 200 °C	Sodium chloride, $(NH_4)_2SO_4$

and during it, the evaporation rate is controlled by the migration of the moisture/vapor through solid at the surface (crust formation). This is accompanied by an increase in droplet temperature as some of heat is utilized to heat the core of the droplet. Different approaches divide the drying process into 4 stages (Farid, 2003) or even five stages (Nesic and Vodnik, 1991), but all remain in the frame of the two drying stages mentioned earlier. Models published in the literature followed different approaches to simulate the drying of a single droplet. Charlesworth and Marshall (1960) are considered to be the first to focus on the drying kinetics of droplets with dissolved solids. Their study provided a morphology chart of the droplet during its drying life time for different solutions at different drying conditions. However the semi-theoretical model they proposed, may not be applied to predict the time of solid phase appearance and crust completion (Adhikari et al., 2000). However, the receding interface model they presented has been further developed by other researchers (Sano and Keey, 1982, Cheong et al., 1986, Nesic and Vodnik, 1991). The droplet evaporation is assumed to occur at the crust-core interface, and once the crust is formed, it is assumed to be rigid. Therefore heat is transferred through the crust by conduction and the droplet is assumed to have uniform temperature i.e. small Biot number. Recently Mezhericher et al. (2006) and Dalmaz et al. (2007) proposed a theoretical model describing the drying process. In their model they account for the heating up step at the beginning of the evaporation process, where the Biot number is larger than one. A PDE of energy conservation for both core and crust regions were proposed, including heat absorption by the crust and crust resistance. Dalmaz et al. (2007) assumed a droplet that consists of a wet core (liquid phase and solids of pre-defined porosity) surrounded by a layer of liquid, and calculated the evaporation of the liquid layer until the surface of the wet core is reached. Here, the constant rate period is finished and the falling rate period begins, which means evaporation of the water occurs inside the pores of the shell, where the liquid phase and the gas phase contact each other i.e. diameter of the wet core. The evaporated water then diffuses through the dry part of the pores into the bulk gas phase. This makes the model inapplicable for droplets with dissolved solids i.e. salts. However both models neglect internal circulation.

Luikov (1975) developed a unique approach to describe the drying of porous bodies based on the application of the principles of irreversible thermodynamics. According to Luikov's model, in the falling rate period, the drying material is divided into dry and wet zones, each having a different moisture migration mechanism. The zones are separated by an evaporation front, which recedes as drying proceeds. This approach has the advantage of not requiring the assumption of any controlling mechanism of internal moisture migration. However, the resulting set of the governing differential equations requires the use of the experimentally determined diffusion and thermal conduction coefficients, which puts a limitation on the applicability of the model.

Jaeschke (1964) formulated an analytical model for the drying kinetics of materials with hygroscopic properties in the second drying stage. The vapor diffusion and the capillary fluid diffusion are the controlled mechanisms. Structural changes such as shrinkage and deforming influence these mechanisms. Therefore, it was not specific to the drying of drops. Cai and Zhang (2003) developed an algebraic explicit analytical solutions of drying of an infinite plate of defined thickness, he solved a set of partial differential equations that describe the drying process, he assumed a one-dimensional and unsteady process, his analytical solution is valid for the case of varying diffusion coefficient.

Brenn (2004) proposed an analytical solution for the concentration field in multiphase droplet as a function of time, he regarded the diffusion to be controlled only by mass transfer and by the surface shrinkage of the drying droplet. He assumed a flat temperature profile inside the droplet; however, he did not consider the recirculating motions inside the droplet for mass transfer. Thus the solution is valid for cases with a linear decrease of the droplet surface area with time, i.e., constant rate period.

Wijlhuizen et al. (1979) investigated the drying of pharmaceutical and food products, various studies also concerned with the retention of volatile flavor components, in which the transport of water as well as the volatiles inside the liquid phase are governed by the molecular diffusion. Their model tracked the drying history of skim milk droplet, the model accounts for two different cases, compact particle (fully liquid droplet) and hollow particle (which is a consequence of drying the droplet with an air bubble inside). They were mainly interested in the thermal degradation of phosphate enzymes. The temperature variation within the droplet is neglected, and further, by not allowing the formation of the crust, the study exhibited overestimated results especially in the falling rate period. This work is followed by a new model (Sano and Keey, 1982) taking into account the vapor pressure inside the droplet as the criterion to determine the inflation and the rupture of particle. This model covers the first, second and third stages of drying, including superheating of the droplets to the boiling and bursting point. For prediction of internal concentration profiles they have used the transient convective diffusion equation, including the additional term for convection due to diffusion.

Vehring et al. (2007) studied the formation of microscale particles using monodisperse streaming method, their experimental technique demonstrated the influence of the drying gas temperature on the final product (particles) morphology. Their model simplified the drying process by solving the problem analytically, which has been used to expect the total evaporation rate. Since the analytical model does not describe non-stationary phase of drying process, and due to complexity of the particle diffusion, solvent drying , they also consider a numerical model that takes into account the liquid evaporation as well as the diffusion of the particle as a result of the surface regression. Their assumption of constant evaporation rate by assuming the D^2-law does not seem adequate to follow the drying process when the crust is formed, the resistance to evaporation is not any more a function of the boundary gas layer but more a function of diffusion in the crust. The introduction of a Pecelt number helps to quantify the influence of both competing phenomena, which is the ratio of the diffusion coefficient of the solute and the evaporation rate of the solvent.

Frey and King (1986) model the drying of food products by a foaming technique. They developed a simplified model to describe the drying in the constant rate period to investigate the aroma retention at the end of the drying period. The droplet contains many small bubbles. The estimation of the effective diffusion coefficient of the bubble is important to predict the drying rate of the solvent, and by introducing Pecelt number, they were able to simulate different cases of droplet drying and evaporation. El-Sayed et al. (1990) studied the drying of coffee extract, skim milk and maltodextrin solutions. Drops undergo changes in morphology, size, shape, and appearance as they dry, the effect of different operational parameters were investigated such as air temperature and initial solute concentration. El-Sayed et al. (1990) compared the drying of droplets suspended by glass filament versus falling drop method. They reported that droplet morphology is influenced by the glass filament; it may promote heat transfer and bubble nucleation. Those experiments were compared to a model developed by Wallack et al. (1990). They predict the water content in drying particles, and their model is based on the assumption of viodless sphere which neglects internal circulation.

A model-based analysis of Maltodextrin and trehalos solutions drying is presented by Sloth et al. (2006). They found the diffusion coefficient of water in Maltodextrin by fitting the model to their experimental results, however, the fitting of the diffusion coefficient $\mathscr{D}$ was done for one set of experiments i.e at initial concentration and drying temperature; hence, the diffusion coefficient is valid only for this set of experiments. Ferrari et al. (1989) proposed a procedure to calculate the concentration dependence of effective diffusivity of skimmilk droplets based on the regular regime theory (Schoeber, 1976), which is applicable when concentration profiles and their changes become independent of the initial solvent concentration. A correlation of the effective diffusion coefficient is valid for different process parameters, i.e temperature, solute concentration. This method, however, seems to fail at high solute concentration.

Cheong et al. (1986), applied a receding interface approach to study droplets with dissolved solids. They solved the energy conservation for the wet core and the dry region, and simplified the heat transfer in the crust by a linear gradient. This contradicts the assumed spherical geometry of the droplet; however, an effective diffusion coefficient of water vapor through the crust is assumed, which is a function of crust porosity. Farid (2003) developed a model based on a receding interface. The main assumption of the model was based on the resistance approach which controls the drying rate i.e. the internal conduction and external convection heat resistances. Similarly to Kuts et al. (1996), Farid (2003) assumed the temperature over the crust-wet core interface to be constant and equal to that of wet-bulb temperature. This assumption is considered to be weak, because water vapor concentration at the interface is higher than that at bulk drying gas. Hence, interface temperature should be higher the wet-bulb temperature of drying gas medium.

Ford (1996) presented a model based on a diffusion approach which describes the drying of solution droplets, including the crystallization of salt in a region close to the surface. In his model he took into account the growth of the crystals inside the droplet, and assumed that the second drying period starts (crust formation) when the thickness of the crystals at the surface is two times larger that the crystal size. (Lee and Law, 1991) characterize this stage when the thickness of the crust is three times the solid particles diameter. Furuta et al. (1982) presented two models(perfect mixing model and diffusion model) to predict crystals formation at the surface of different salt materials. Once the concentration at the surface exceeds the critical concentration, crystallization begins. However, he assume that the acoustic field doesn't have any influence on the transfer parameters i.e Sh and Nu numbers (Ranz and Marshall, 1952a). This contradicts with the work presented by (Yarin et al., 1999) and (Lierke, 1995).

Experiments from Charlesworth and Marshall (1960) show that the shell formation begins from the front stagnation point and proceeds rapidly towards the rear stagnation point. The effect of internal circulation on the drying of multiphase droplet is not well understood. The internal circulation enhances the mass transfer of water vapor and shortens the drying time (Hecht and King, 2000, Sirignano, 1999).

Chung (1982), gave an estimate of the characteristic convention time inside the droplets. By comparing it with the shell formation time, they concluded that the internal circulation may play a dominant role in the shell formation.

Despite the fact that drying of single droplet received so far large interests in research, both experimentally and numerically. Most of the experimental techniques tend to use an intrusive methods to suspend single droplets, which has its own deficits, as its influence heat transfer and particle morphology. Beside that, it does not reflect the drying of droplet in spray dryer i.e. container less suspension of droplets and free rotation. Moreover, all models neglect the internal circulation inside the droplets, and assumes a 1-D approach to calculate the solid concentration profiles. Description of the shell formation and growth just before the second drying stage starts receives little interest.

In the present study, an experimental work is devoted to a better understanding of single droplet drying and to characterize the shell formation as it starts to build up. A 2-D numerical model is formulated based on the experimental investigations to describe the accumulation of solids inside the droplet and on the surface, until the crust is formed. This model will take into account the influence of the flow along the droplet surface, it's drying temperature and relative humidity.

Chapter 3

Description and Characterisation of Experimental Facility

In this chapter, the principle and the characterization of the acoustic levitator will be addressed, the experimental setup, mainly the acoustic levitator and other auxiliary facilities will be illustrated; the experimental procedure and the calibration of the air flow, image acquisition and analysis will be explained.

3.1 Experimental facility

3.1.1 Acoustic levitator

The main unit of the experimental facility is the acoustic levitator, it consists of two main parts, the transducer and the reflector. The transducer is attached to a piezoelectric crystal that vibrates at an ultrasonic frequency. These vibrations travel through the air to hit the reflector. Both transducer and reflector are aligned coaxially. Inside the transducer, a central hole of 1 mm diameter is drilled, a syringe is then is inserted through this hole to deliver the droplet into the acoustic field.

The reflector is connected to a traverse micrometer which allows adjustment of the distance between the transducer and the reflector. To achieve a stabile levitation, the vertical distance between the reflector and the transducer must be a multiple of the half wave length of the incident sound wave. The intensity of the acoustic field is

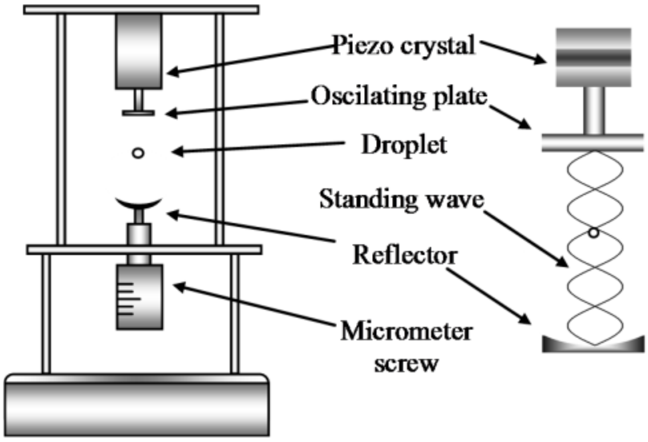

Figure 3.1: Sketch of an acoustic levitator.

controlled via a power supply unit (ultrasonic generator). The ultrasonic generator has a standard operation frequency of 58 kHz and provides 0.65 - 5 Watt. This power supply unit enables the resonance tuning control of the reflector distance at constant transducer amplitude setting. The acoustic levitator is equipped with double-wall glass chamber that is used to isolate the droplet in a controlled environment *i.e.* temperature and humidity.

3.1.2 Humidity, temperature and air flow rate units

An air flow of defined humidity and flow rate is injected from the reflector. The air flow rate is calibrated to reach an optimum value which ventilates the outer acoustic streaming without influencing the acoustic boundary layer, see §(3.3.3).

In order to conduct experiments at various humidities, the incoming air flow is dried to a

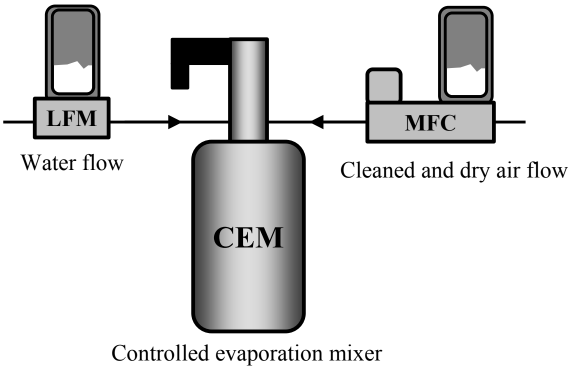

Figure 3.2: Controlled evaporation mixer (CEM) system from Bronkhorst (NL), CEM mix air and water at different ratios in order to generate an air stream with desired humidity value that enters into the process chamber.

very low humidity 1% ±0.50. The drying unit consist of three stages. First, oil aerosols, condensates and solid particle that may exist using a silicagel cartridge (Zander MDK 15) are filtered out. Then, another drying step follows using a tube filled with $MgSO_4$. Finally the air is filtered using a fine filter(Festo) to remove any dust particles.

The air humidity is set by a controlled evaporation and mixing (CEM) unit provided by Bronkhorst (NL). The flow rate of air and water can be adjusted to achieve the desired humidity; air flow can be changed from 1-30 l/min and water flow from 0.2-10 g/h. The evaporater can reach temperatures up to 200 °C. To regulate the temperature of the drying gas, the process chamber is heated using a heated water stream controlled by the water heating system from (launa). Furthermore, the incoming air stream used for ventilation is heated just before it enters the glass chamber using a system of heating wires that surrounds the reflector. The energy required is regulated via a power supply by adjusting the current and voltage of the wire.

Finally both temperature and humidity inside the process chamber are monitored before and after each experiment using a hygrometer device(testo) with accuracy of 0.1% RH and 0.05 °C.

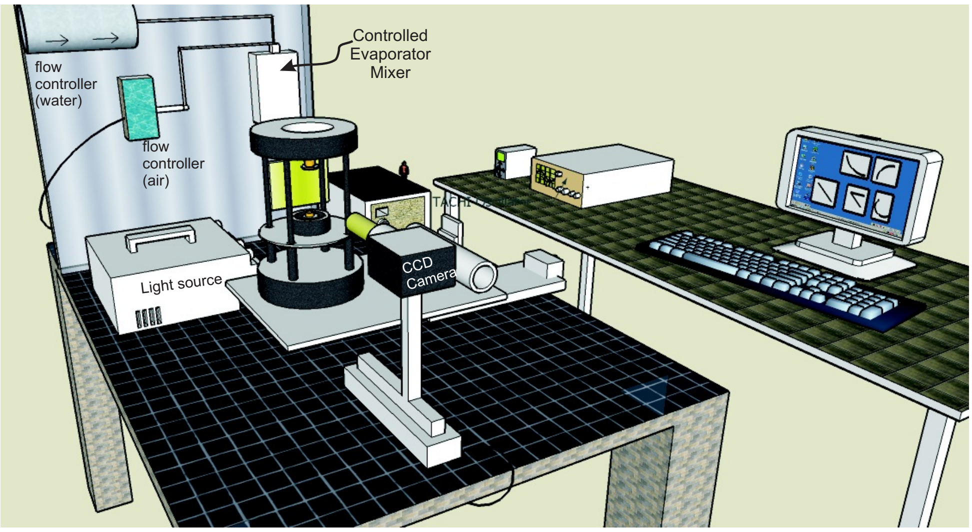

Figure 3.3: Schematic of the experiment rig consist of the acoustic levitator, humidity and image acquisition systems.

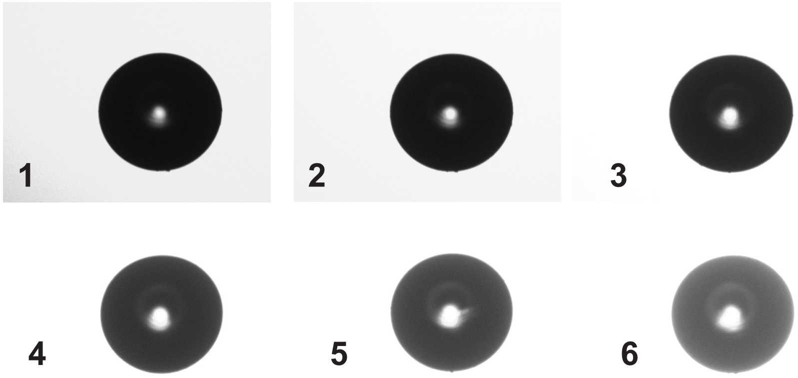

Figure 3.4: Series of shadow images at different light intensities.

3.1.3 Image acquisition and analysis system

To determine the evaporation rate of the droplets, the diameter of the droplet is measured during the evaporation at defined time steps. An imaging system is used to record and analyze the images of the droplet. It consists of CCD camera (Basler A630fc) with 35 fps and 1200 x 1024 resolution, a long-distance microscope, which magnifies the droplet image for better determination of the diameter, and a cold light source for back illumination as shown in figure 3.3. The CCD camera records a series of shadow images of the meridional section of the droplet and sends them to an imaging software for on-line analysis.

The imaging system is calibrated for the best back light illumination, as shown in figure 3.4, Different back illumination shadow images are taken for a glass sphere, the diameter is then calculated and compared with the diameter of the particle in levitation, as depicted in figure 3.5.

In each set of experiments the magnification factor of the long-distance microscope is measured using a high precision microscale etched on glass plate. The magnification factor is then used as an input parameter in the image analysis program. An in-house developed image acquisition and analysis software is used to store images of the droplet. These images are then analyzed to extract the equivalent drop diameter, vertical position and axis ratio. Both image analysis and image acquisition are implemented using Matlab tool boxes.

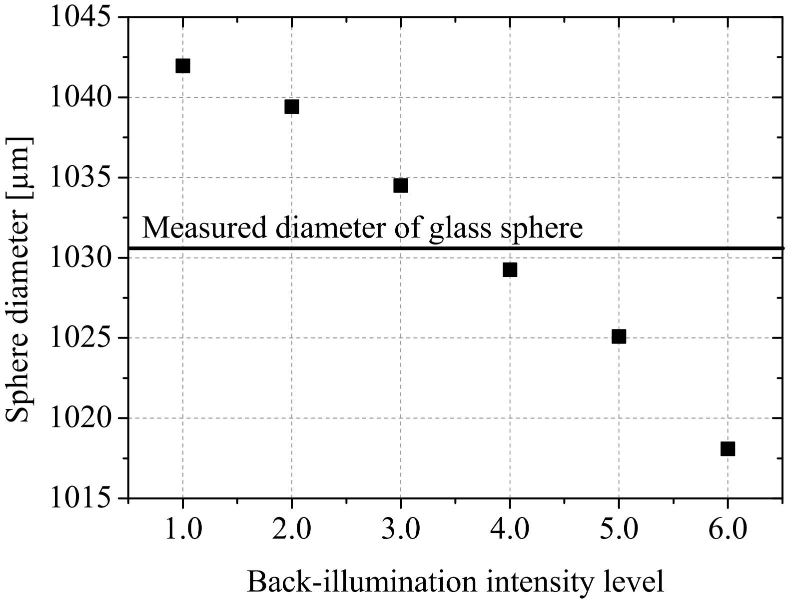

Figure 3.5: Glass sphere diameter calculated at different light intensities.

3.2 Principles and characterization of the acoustic levitator

3.2.1 Acoustic levitation

Acoustic levitation is a method for suspending matter in a medium by using acoustic radiation pressure from intense sound waves in the medium . This type of levitation is possible because of the non-linear effects of intense ultrasonic waves. Samples with diameters of up to a few millimeters can be suspended in a gaseous carrier medium by means of an acoustic standing wave field.

This is useful for many investigations on single liquid droplets or solid particles under well defined environmental conditions, such as temperature, gas pressure and composition and relative humidity. Acoustic levitation has been used for several decades. The first droplet in a standing acoustic wave was realized by Bücks and Müller (1933). Later King (1934) gave the theoretical description of the acoustic levitator. The development of the acoustic levitator as a device for levitation of small objects, was mainly carried out in the mid seventies by the American space agency and the European space agency (Trinh et al., 1996). It has since been used as a precise spatial fixation of small samples under conditions of microgravity and it's application can be found in material

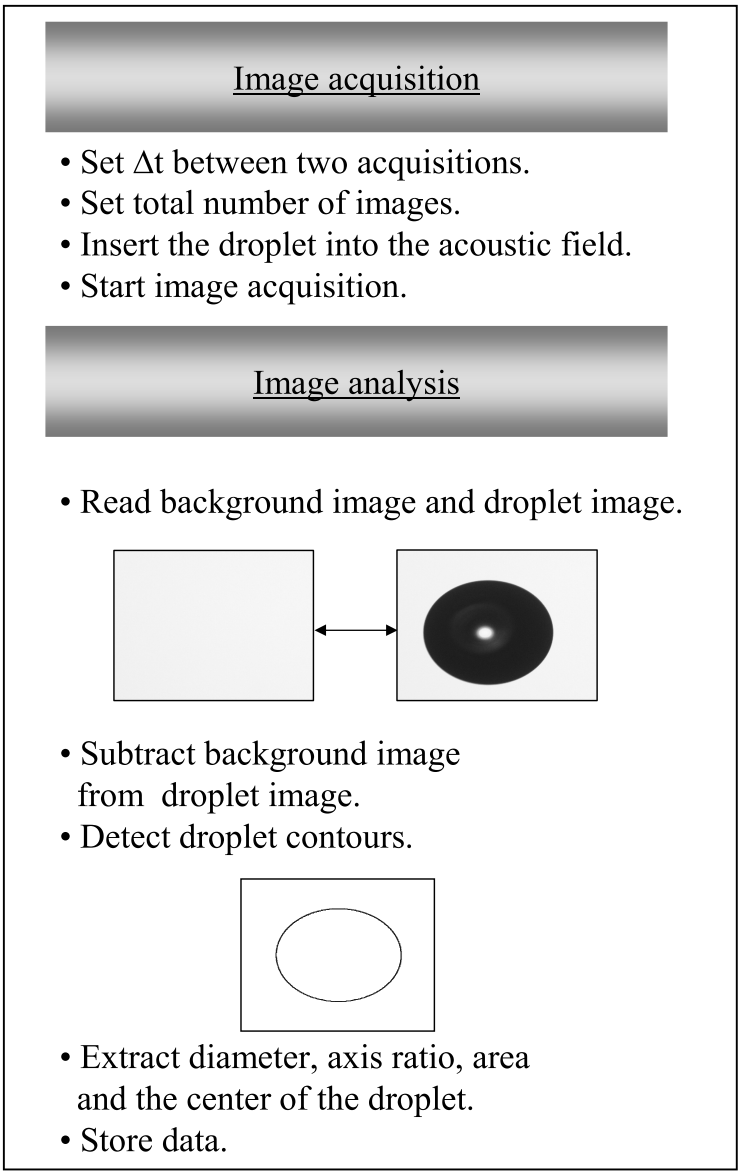

Figure 3.6: Flow diagram of the image acquisition and image analysis program

science, space laboratory, physical and biological experiments.

However, many research areas are also interested in acoustic levitation, starting from analytical chemistry. They work with titration of very small volumes that are sensitive to any side effects or contamination from the wall (Rohling et al., 2000) and liquid/liquid extraction (Welter and Neidhart, 1997). Tian and Apfel (1996) studied the evaporation from 2D droplet arrays electrically charged and suspended in an acoustic field. Crystallization of single droplets in an acoustic levitator were studied by (Brenn et al., 2001, Sacher and Krammer, 2005). Other applications and possibilities of the acoustic levitator are outlined in a review article by Lierke (1996a).

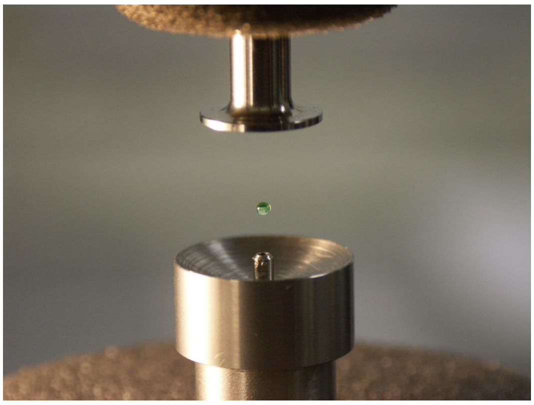

Figure 3.7: Droplet in an acoustic levitator

3.2.2 Standing acoustic wave

Sound is a disturbance or vibration that moves through a medium (air, liquids or solids) in the form of waves. The source of sound is any object that moves or rapidly changes shape which causes the air around the object to vibrate (Strutt et al., 1945). The concept of standing waves is directly dependent on the reflection of sound waves. If the sound travels between two solid parallel walls separated by a given space or distance, the wavelength strikes the right wall and is reflected back towards the sound source. This sound wave is bouncing back and forth between the parallel walls, generating the so called standing acoustic wave. The wave number $\overrightarrow{\mathbf{k}}$ of both waves have the same magnitude, but are anti-parallel, (Benenson et al., 2006).

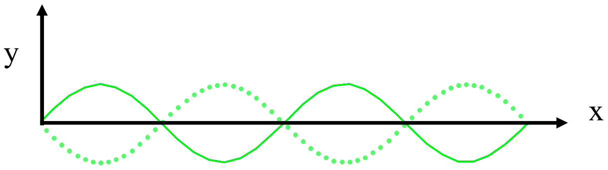

Figure 3.8: Standing wave propagating between two plates.

$$\begin{aligned} y_1(\overrightarrow{\mathbf{r}},t) =& A\cos(\overrightarrow{\mathbf{k}}\cdot\overrightarrow{\mathbf{r}}-\omega t) \\ y_2(\overrightarrow{\mathbf{r}},t) =& A\cos(-\overrightarrow{\mathbf{k}}\cdot\overrightarrow{\mathbf{r}}-\omega t) \\ y(\overrightarrow{\mathbf{r}},t) =& y_1(\overrightarrow{\mathbf{r}},t)+y_2(\overrightarrow{\mathbf{r}},t) = -2A\cos(\omega t)\cos(\overrightarrow{\mathbf{k}}\cdot\overrightarrow{\mathbf{r}}) \end{aligned} \tag{3.1}$$

The effect of the sound waves resonating as depicted in fig. 3.8, is a series of nodes (minimum pressure) and anti-nodes (maximum pressure) at fixed points between the transducer and reflector. The distance from each node to the next, L_x, is related to the wave length λ of the ultrasonic wave, $\lambda = 2 \cdot L_x$. For astanding wave of length L, the wavelengths of the standing waves are:

$$\lambda = \frac{2 \cdot L}{n} \quad n = 1, 2, 3, \cdots \tag{3.2}$$

The standing wave oscillates with frequency f. The relationship between frequency and wave length travelling a the speed of sound c_0 is:

$$\lambda \cdot f = c_0 \tag{3.3}$$

The velocity of sound waves depends on the properties of the material or medium through which the sound waves propagates. In the gas phase it can be described as:

$$c_0 = \sqrt{\frac{P \cdot k}{\rho}} = \sqrt{k \cdot R \cdot T} \tag{3.4}$$

where ρ is the density of the of the gas, R is the universal gas constant, k the adiabatic coefficient, (which is 1.402 for air) , and T, P are the temperature and the pressure of the gas respectively. The change of the sound velocity with the absolute temperature T is the most important factor. The temperature dependency of the velocity of sound in air in the range between -20 ^oC and 40 ^oC may be approximated linearly (Benenson et al., 2006):

$$c_{0,air} = (331.5 + 0.6 \cdot T) \tag{3.5}$$

Many quantities are used to describe the sound wave propagating in a gas medium, such as gas particle velocity B, which can be related to the particle displacement ξ for a single plane wave of frequency f:

$$B = \xi \cdot \omega = \xi(2\pi \cdot f) \tag{3.6}$$

The sound pressure is characterized usually by a reference sound pressure P_{ref} and the ratio is called sound pressure level SPL. It's unit is dB, and used as a measure of sound strength:

$$SPL = 20 \cdot \log_{10} \frac{P}{P_{ref}} \tag{3.7}$$

P is the sound pressure in N/m^2 and $P_{ref} = 2 \cdot 10^{-5} N/m^2$.

3.2.3 Acoustic force

An object in the presence of a sound field will experience forces associated with the field. An acoustic force arises from the scattering of the sound wave by the body. In order to have an object suspended in the acoustic field, the acoustic force should counteract the gravity force i.e, weight of the object. Calculation of the acoustic radiation force has been addressed in the literature. King (1934) calculated the force acting on a rigid sphere by solving the linear wave equation with a scattering correction.

As depicted in fig. 3.9 a droplet is levitated in the acoustic standing wave, the distance between the reflector and the transducer is equal to $k \cdot \lambda/2$.

It's convenient to assume the acoustic field to be a harmonic standing wave of some given amplitude which corresponds to the solution of wave equation for an infinitely long levitator (Yarin et al., 1998). In order to set an intense acoustic field between the transducer and the reflector, acoustic levitators works in a regime close to resonance conditions. There are many resonance modes (Lierke, 1996a), in which the transducer and the reflector are positioned far away from each other, *i.e* a resonance is established when the distance L is multiple of half wave length of the acoustic wave $\lambda/2$. The total pressure perturbation at the droplet surface due to the interaction with the acoustic field can be divided into an incident acoustic wave, P_i' and a scattered acoustic wave, P_s':

$$P' = P_i' + P_s' \tag{3.8}$$

The scattered pressure is expressed by the equation, (Yarin et al., 1998):

$$P_s' = A_{0e} e^{-i\omega t} P_s(\mathbf{r}) \tag{3.9}$$

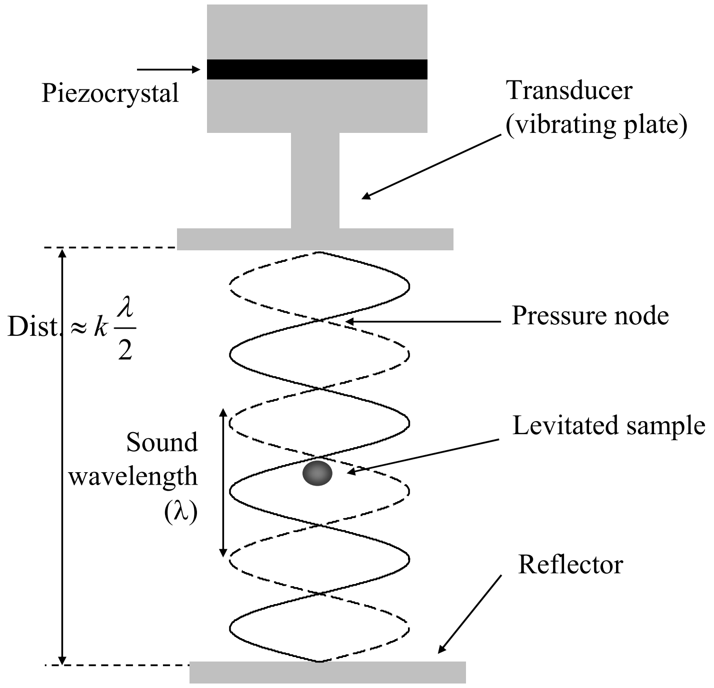

Figure 3.9: Schematic of the standing wave between the transducer and the reflector, piezocrystal oscillates at frequency of 58 kH.

where **r** is the vector radius, P_s can be found with the help of Helmholtz equation:

$$\Delta P_s + \left(\frac{\omega}{c_0}\right)^2 P_s = 0 \tag{3.10}$$

The mathematical solution of eqn. 3.10 can be seen from King (1934) or Yarin et al. (1998) The acoustic field can be calculated by the boundary element method assuming one-dimensional wave equation. With appropriate boundary conditions at the sound source ($x = 0$), and the reflector ($x = L$), it can be used for mathematical description according to Yarin et al. (1998).

$$\frac{\partial^2 P_i'}{\partial t^2} = c_0^2 \cdot \frac{\partial^2 P_i'}{\partial x^2} \tag{3.11}$$

the corresponding boundary conditions at the transducer and the reflector being:

$$\begin{aligned} x &= 0 \quad \Rightarrow P_i' = A_0 \cdot e^{i\omega t} && \text{(sound source)} \\ x &= L_R \quad \Rightarrow \frac{\partial P_i'}{\partial x} = 0 && \text{(reflector)} \end{aligned} \tag{3.12}$$

P_i' is the pressure perturbation of the incident wave, A_0 its amplitude at the source surface, ω the angular frequency corresponding to the ultrasonic range, c_0 the speed of sound in air, t the time, x the vertical coordinate and i the imaginary unit. The axial position of the pressure nodes x within the standing acoustic wave can be calculated by:

$$x = L_R - \frac{c_0}{\omega} \cdot \left(\frac{\pi}{2} + \pi n\right) \qquad n = 0, 1, 2, 3, \ldots \tag{3.13}$$

The solution of eqn. 3.11 and the boundary conditions eqn. 3.12 is given by:

$$P_i' = A_{0e} \cdot e^{i\omega t} \left[\tan\left(\frac{\omega L_x}{c_0}\right) \sin\frac{\omega x}{c_0} + \cos\frac{\omega x}{c_0}\right] \tag{3.14}$$

The solution of eqn. 3.14 can be approximated for the incident wave in an infinite levitator (Yarin et al., 1998, Lee et al., 1991):

$$P_i' = A_{0e} \cdot e^{i\omega t} \cdot \cos\frac{\omega}{c_0} x, \tag{3.15}$$

where A_0e is the effective amplitude of the acoustic field and is calculated by:

$$A_{0e} = -\frac{A_0}{\cos(\omega L_R / c_0)} \tag{3.16}$$

The number of pressure nodes calculated from eqn. (3.15) are equal to number of nodes calculated by 3.14, however, the position of the pressure nodes differs by about 5% (Yarin et al., 1998). Figure 3.10 shows the sketch of the incident acoustic wave, the pressure nodes and the acoustic levitation force.

In order to calculate the acoustic force, the equation for the acoustic radiation pressure given by Landau and Lifshitz (Kastner et al., 2001) defined as:

$$\begin{aligned} P_a &= \frac{\langle P'^2 \rangle}{2 \cdot \rho_{gas} \cdot c_0^2} - \frac{\rho_{gas}}{2} \langle \upsilon' \cdot \upsilon' \rangle \\ \langle P'^2 \rangle &= \frac{A_0^2}{2} \cdot \cos^2\left(\frac{\omega}{c_0} x\right) \\ \langle \upsilon'^2 \rangle &= \frac{A_0^2}{2 \cdot \rho_{gas}^2 \cdot c_0^2} \cdot \sin^2\left(\frac{\omega}{c_0} x\right) \end{aligned} \tag{3.17}$$

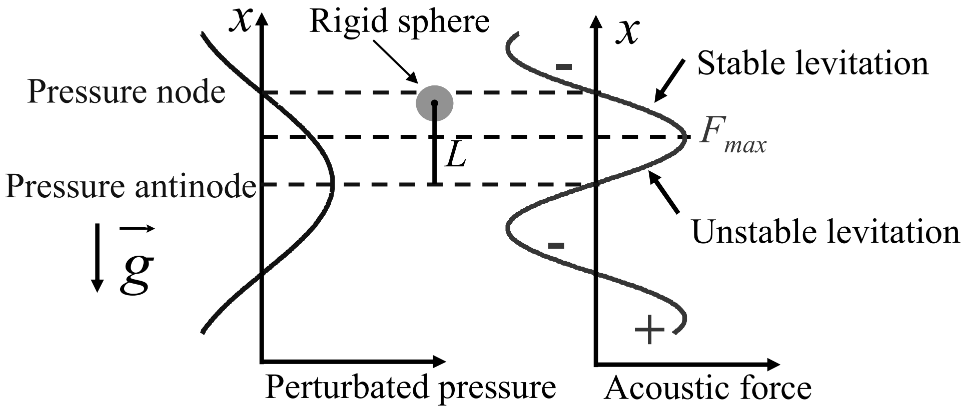

Figure 3.10: Incident acoustic wave with levitation force.

Both values $\langle p'^2\rangle$ and$\langle v'^2\rangle$, which is the squared acoustic gas velocity are time averaged over a period longer than the wave cycle (Yarin et al., 1998) and denoted by $\langle\rangle$. King (1934) as well Yarin et al. (1998) calculated the resulting acoustic force from the acoustic radiation pressure produced by a standing acoustic wave at the droplet or particle surface defined by eqn. (3.9), eqn. (3.15) and eqn. (3.17), the acoustic force reads as:

$$F_{ac} = \pi\rho_{gas} \cdot r_0^2 \cdot \left(\frac{A_0}{\rho_{gas}}\right)^2 \cdot \sin^2(2k \cdot \Delta x_D) \cdot f(\Omega) \tag{3.18}$$

with $\Omega = k \cdot r_0 = (\omega/c_0) \cdot r_0$ and $k = (\omega/c_0)$ is the wave number and Δx_D the distance from the mass center of the droplets to its next upper pressure node. The function $f(\Omega)$ is given by:

$$\begin{aligned} f(\Omega) = \Bigg[& \frac{1}{(\Omega)^3} \frac{(F_0F_1 + G_0G_1)_1}{H_0^2 H_1^2} (\Omega)^2 \\ & - \frac{2}{(\Omega)^5} \frac{(F_1F_2 + G_2G_2)}{H_0^2 H_1^2} \left\{ (\Omega)^2 - 3 \cdot \left(1 - \frac{\rho_{gas}}{\rho_{liquid}}\right) \right\} \\ & + \sum_{n=2}^{\infty} (-1)^n \frac{n+1}{(\Omega)^{2n+}} \frac{(F_{n+1}F_n + G_{n+1}G_n)}{H_{n+1}^2 H_n^1} \left\{ (\Omega)^2 - n \cdot (n+2) \right\} \Bigg] \end{aligned} \tag{3.19}$$

The values F_i , G_i and H_i are functions of Ω and are defined by:

$$\begin{aligned} F_i(\Omega) =& (\Omega)^{1-i} n_{i+1}(\Omega) + \frac{i}{(\Omega)^i} n_i(\Omega) \\ G_i(\Omega) =& (\Omega)^{1-i} j_{i+1}(\Omega) + \frac{i}{(\Omega)^i} j_i(\Omega) \\ H_i(\Omega) =& \left[F_i^2 \Omega) + G_i^2(\Omega)\right]^{1/2} \end{aligned} \tag{3.20}$$

The functions $j_i(\Omega)$ and $n_i(\Omega)$ are the spherical Bessel and Neumann-Functions, respectively. Eqn. (3.20) is valid for all values of Ω (Yarin et al., 1998), it can be approximated into a simpler form when $\Omega << 1$, King (1934) and Lierke (1996b) proposed that $f(\Omega)$ take the following form:

$$f(\Omega) = \frac{5}{6}\Omega \frac{3}{(2\Omega)^2} \left[\frac{sin(2\Omega)}{2\Omega} - \cos(2\Omega)\right] \tag{3.21}$$

3.2.4 Sound pressure level, SPL

In order to conduct experiments of evaporation and drying in the acoustic levitator, and to compare them with evaporation/drying models, a certain knowledge about the acoustic field is required. Sound pressure level (SPL) has been used (see Yarin et al., 1999, Kastner et al., 2001, Tuckermann, 2002, Rensink, 2004) as parameter to characterize the strength of the acoustic field and it's influence on transport processes at droplet surface, mass and heat transfer coefficients, see section §3.3.

The estimation or measurement of the sound pressure level (SPL) is of great importance. As shown from eqn. (3.7), SPL is a logarithmic scale of the sound pressure to P_{ref}. Many methods exist to measure the SPL. Some are direct methods, such as using a microphone to measure the intensity of the of the acoustic field. However, this technique is intrusive and the size of the microphone can't be neglected as it will scattered the acoustic waves (Tuckermann, 2002). The second method called drop out method, is indirect. The acoustic field, i.e. SPL, is calibrated using it's influence on the object (rigid sphere or droplet) suspended in the acoustic levitator (Tuckermann, 2002, Yarin et al., 1998). In this method, sound pressure level is linked to the driving voltage of the piezo-ceramic. The levitation force required to levitate the drop should be large enough to counteract the gravity force, $F_{drop} = \pi/6 \cdot \rho_d \cdot D^3 \cdot g$. The idea of this method is simply to decrease the driving voltage until we reach the minimum acoustic force to hold the droplet suspended and any further decrease in the driving voltage will cause the droplet to fall down. Just at this moment, the droplet is positioned at $\frac{\Delta x_D}{a_0} = \pi/4\Omega$ and $F_{ac} = F_{drop}$, where F_{ac} is the acoustic force, (King, 1934):

$$A_{0e}^2 = \frac{\rho_d \cdot \rho_g (D/2 \cdot c_0^2)}{f_{king}(\Omega) \cdot \sin(2\Omega \cdot L)} \tag{3.22}$$

where L is rendered by a_0 and its the distance between drop center and the pressure antinode, as depicted in fig. 3.10, $L = \frac{\pi}{4 \cdot \Omega}$ at dropout and the amplitude of sound wave can be calculated:

$$A_{0em}^2 = \frac{4}{3} \frac{\rho_{drop} \cdot \rho_g (d_{drop}/2 \cdot c_0^2)}{f_{king}(\Omega)} \tag{3.23}$$

In the dropout method the object is assumed to be spherical, i.e. the drop deformation is neglected. In order to get pressure amplitude at dropout, it must be assumed that the driving voltage is varying linearly with oscillation amplitude (Yarin et al., 1998, Tuckermann, 2002, Lierke, 1996b):

$$A_{0e} = A_{em} \frac{U_0}{U_{0m}} \tag{3.24}$$

where A_{em}, U_{0m} are the pressure amplitude and driving voltage at drop out respectively.

However, applying this method to the acoustic levitator with 58kH working frequency in the present study was not possible since the minimum of the driving voltage is limited and the minimum driving voltage was still be large enough to keep the droplet levitated.

The third method is to estimate of SPL by taking into account the drop shape deformation (Yarin et al., 1998). The forces acting on the droplet are the capillary force, hydrostatic force and acoustic force. The shape of the droplet results from the equilibrium between these forces. The pressure at drop surface is:

$$P_{drop,surface} = P_{h,air} + P_a - \alpha \cdot \kappa \tag{3.25}$$

where α is the surface tension and κ is the surface curvature. The algorithm for calculating sound pressure level is explained by (Yarin et al., 1998).

The effective sound pressure level($SPL_{effective}$) using the correlation of YPT (Yarin et al., 1998) is defined as:

$$SPL_{effective} = 20 \cdot \log(A_{0e}) + 74 \tag{3.26}$$

where A_{0e} is the effective sound wave amplitude in dyn/cm^2. The sound pressure level at the sound source corresponding to the amplitude of the sound source is :

$$SPL = SPL_{effective} + 20 \cdot \log\Big[-\cos(\omega \cdot L_R/c_0)\Big] \tag{3.27}$$

3.3 Interaction of the acoustic field with levitated droplet

Levitation of single droplet (pure liquid or multiphase) in the acoustic field occurs because the acoustic force is counteracting the gravity force, i.e., droplet's weight. The acoustic field will influence the droplet i.e. deformation of the droplet. Moreover, the interaction of the standing acoustic wave with the droplet will induce a secondary flow around surrounds the droplet (Yarin et al., 1998). In order to study the drying kinetics of single droplets those influences have to be understood. (Yarin et al., 1998), (Kastner et al., 2001) and (Rensink, 2004).

3.3.1 Influence of droplet volume on the strength of the ultrasonic field

Droplet evaporation results in volume decrease, a levitated droplet will be deformed to an ellipsoidal shape due to the difference of radial and axial forces acting on the droplet. As the evaporation continues the droplet shape tends to converge to spherical i.e. the aspect ratio approaches unity. Aspect ratio is defined here as the ratio between the horizontal to vertical axis of the drop. Experiments of pure liquid evaporation in an acoustic levitator as depicted in fig. 3.11 show that the sound pressure level, SPL, increases during droplet evaporation. This is explained by the theoretical prediction (Yarin et al., 1999, Trinh and Hsu, 1986). A large deformed droplet in acoustic field results in a resonance shift caused by the scattering from the droplet surface. Typical

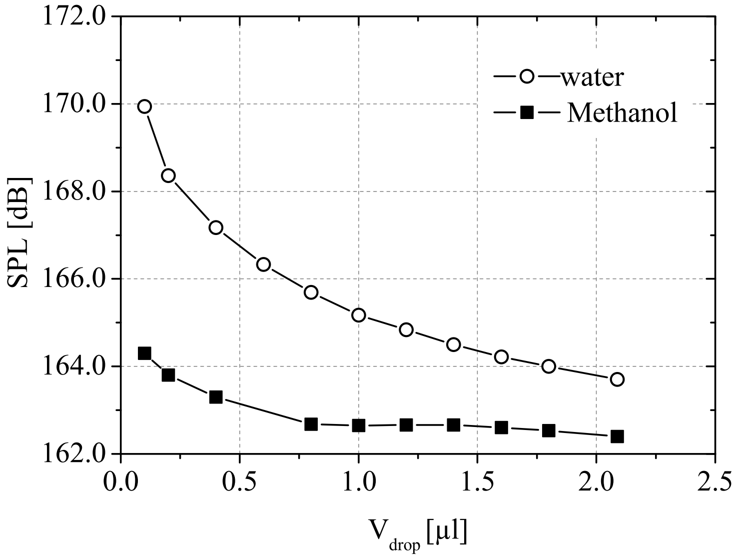

Figure 3.11: Computed evolution of the effective SPL during the evaporation process of drops of water and methanol in the acoustic field.(Zaitone et al., 2006)

results are plotted in fig. 3.11 for water and methanol droplets of 2.5 μl initial volume. It shows that the SPL increases as the water droplet volume decreases, The SPL is deduced directly from the droplet shape, which results from the equilibrium between the capillary force and the acoustic force. Due to the high water density of water when compared to methanol, a higher SPL is generally required for levitation.

3.3.2 Droplet weight influence on the vertical position

In order to suspend a droplet in a standing acoustic wave the acoustic force must be equivalent or larger than the gravity forces i.e. the droplet weight. The droplet is located at equilibrium position below a pressure node in the ultrasonic field. Any increase in SPL values as a result of the droplet evaporation cause the droplet to locate at a new position relative to the adjacent acoustic pressure node.

As the droplet volume decreases, the droplet will get closer to the pressure node. In special cases when the droplet volume stay constant i.e. drying of multiphase droplet (see fig. 3.12 b), the rise of the center of mass of the droplet will be used to deduce the amount of solvent evaporated from the droplet.

$$\frac{4}{3}\pi \cdot r_0^3 \cdot \rho_d \cdot g = \pi \rho_{gas} \cdot r_0^2 \cdot \left(\frac{A_{0e}}{\rho_{gas} \cdot c_0}\right)^2 \cdot \sin(2 \cdot k \cdot \Delta x_D) \cdot f(\Omega) \tag{3.28}$$

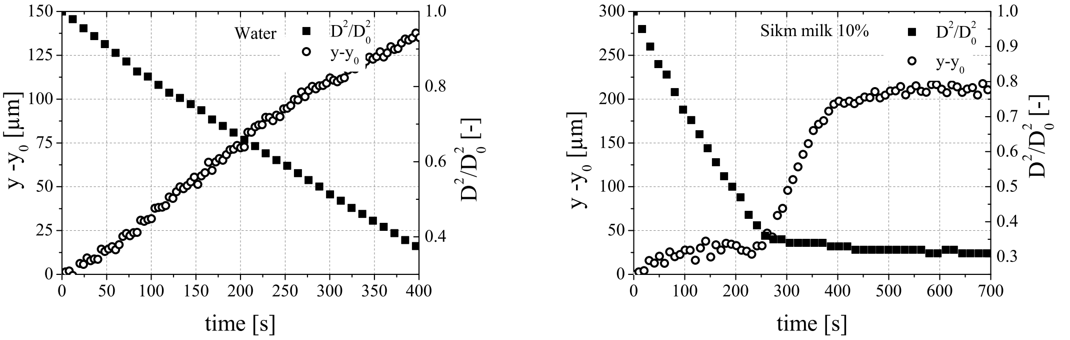

(a) (b)

Figure 3.12: Diagram illustrating the normalized surface area of a) pure liquid droplet and b) multiphase droplet (skim milk 10% initial solids concentration), the change in vertical position of the geometric center of mass of the droplet, in case of multiphase droplet once the crust is formed the vertical distance is only function of the mass loss of the solvent.

3.3.3 Influence of the acoustic field on the heat and mass transfer

Introducing a droplet into the acoustic field generates a secondary flow around the levitated droplets. As depicted in fig. 3.13, it can be divided into inner acoustic streaming and large scale toroidal vortices i.e. outer acoustic streaming.

The inner acoustic streaming generates an acoustic boundary layer. Yarin et al. (1999) calculated the transfer parameters i.e. Sh and Nu numbers around a small droplet, Yarin et.al solves the diffusion equation in the acoustic boundary layer by assuming that the SPL is high enough, thus, inner acoustic streaming dominates free convection, radiation is assumed to be negligible.

$$\langle Sh_{surf} \rangle = 2 \cdot K_{ac} \frac{B}{(\omega_{ac}\mathscr{D})^{1/2}} \frac{\cos^2\theta}{(1+\cos^2\theta)^{1/2}} \tag{3.29}$$

where $\langle Sh_{surf} \rangle$ is the time-averaged Sherwood number over the droplet surface, θ is the angle that starts from the stagnation point ($\theta = 0$) to the rear stagnation point ($\theta = \pi$). The distribution of $\langle Sh_{surf} \rangle$ is symmetrical about the vertical axis. The coefficient K_{ac}

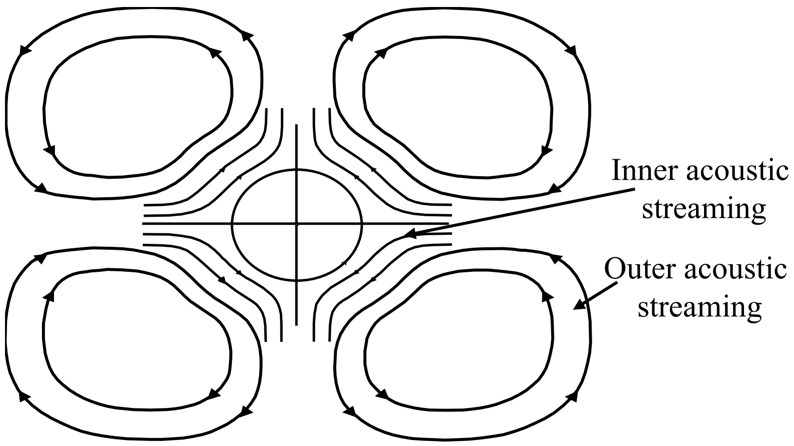

Figure 3.13: Acoustic streaming field around a levitated droplet. The inner acoustic streaming is positioned directly at the acoustic boundary layer, whereas the outer acoustic streaming (outer toroidal vortices) are surrounding the droplet (Yarin et al., 1999).

is a dimensionless factor depending mainly on liquid properties as well as on drop radius, shape and properties of the acoustic wave (Yarin et al., 1999).

$$K_{ac} = \frac{2}{\sqrt{\pi}} \frac{\overline{|\langle \overline{u}_{ac} \rangle| \overline{r}}}{\left(\int_{\overline{x}_2}^{\overline{x}} \langle u_{ac} \rangle \overline{r} \cdot d\overline{x} \right)^{1/2}} \cdot \left(\frac{\omega_{ac} \cdot a / c_0}{A_{0e} / (\rho_{air} \cdot c_0^2)} \right)^{1/2} \tag{3.30}$$

a is the volume-equivalent drop radius and is rendered dimensionless by an initial volume-equivalent drop radius, a_0, and $\overline{|\langle u_{ac} \rangle|}$ is averaged over the whole droplet surface, $\bar{r}$ is the distance of a point on the droplet surface to the semi-minor axis set dimensionless with the initial droplet radius a_0. The term acoustic $\overline{u_{ac}}$ is the inner acoustic streaming velocity and is set dimensionless with the particle velocity B. Yarin et al. calculated $\overline{u_{ac}}$ for small spherical droplet using the approximation:

$$\langle u_{ac} \rangle = \frac{45}{32} \frac{B^2}{\omega_{ac} \cdot r_0} \cdot \sin 2\theta \tag{3.31}$$

$\langle u_{ac} \rangle$ is averaged over multiple cycles of the standing acoustic wave and θ is the perimeter angle measured from the bottom point of the droplet. For droplets of radius much smaller than the wave length of the standing acoustic wave Rensink (2004) and Yarin et al. (1999) estimate $\langle u_{ac} \rangle \sim 1\ m/s$. Therefore, inner acoustic streaming induces an additional convective blowing; hence, the Sh number is expected to be larger according to mass transfer considerations. In order to get the averaged Sh number eqn. (3.29) is

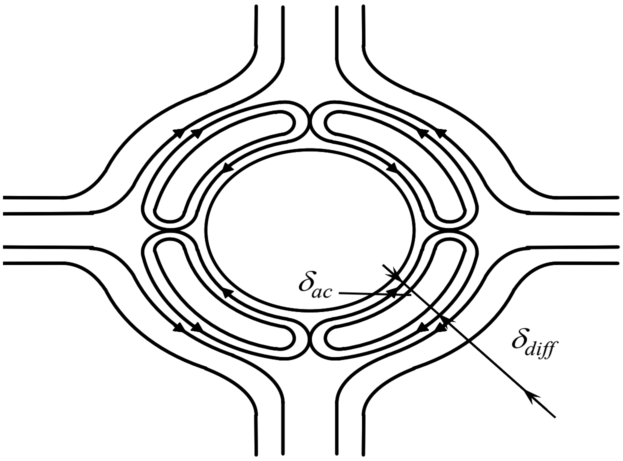

Figure 3.14: Inner acoustic streaming a small sphere positioned at the pressure node of a standing acoustic wave, as well as acoustic and diffusion boundary layer over (Yarin et al., 1999).

integrated over drop surface from $\theta = 0$ to $\theta = \pi$:

$$\overline{\langle Sh_{ac} \rangle} = K_{ac} \frac{B}{(\omega_{ac} \cdot \mathscr{D}_g)^{1/2}} \tag{3.32}$$

K_{ac} is changing as the droplet evaporates and should be re-calculated continuously. For a small spherical droplet levitated directly within the pressure node of a standing acoustic wave, K_{ac} is approximated by $K_{ac} = \left(\frac{45}{4\pi}\right)^{1/2} = 1.89$.

As depicted in fig. 3.14, the inner acoustic streaming form an acoustic boundary layer which has a thickness of order (Schlichting, 1978):

$$\delta_{ac} = \left(\frac{2\mu_{gas}}{\omega_{ac}}\right)^{1/2} \tag{3.33}$$

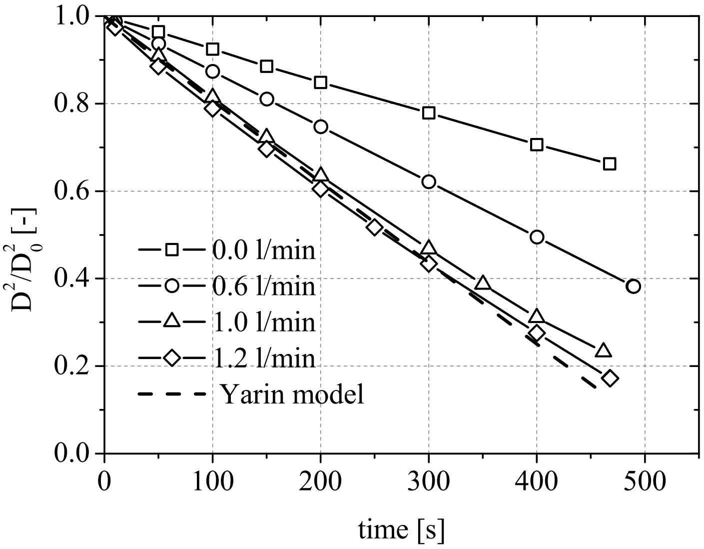

Figure 3.15: Temporal evolution of normalized surface area of water droplets at different ventilation air flow rates, initial droplet volume 2 μl.

Outer acoustic streaming and determination of the optimum ventilation flow

The presence of the toroidal vortices within the vicinity of the droplet acts as a barrier to evaporation and leads to a decrease of evaporation rate. As depicted in fig. 3.13, the outer acoustic streaming surrounding the droplets trap the solvent evaporated from the droplet and thus changing the far field conditions, Yarin et al. (1999) showed that an axial air flow is necessary to blow the accumulated vapor in the acoustic streaming.

Figure 3.15 shows the normalized surface evolution of the water droplet at different air blowing flow rates. Note that without any axial air flow the evaporation of the droplet deviate from the model prediction. In Yarin model, only the influence of the inner acoustic streaming is taken into account.

As the flow rate of air increases, different evaporation rates result. In order to set an optimum air flow to destroy the acoustic streaming, a larger set of experiments were carried out. Air flow rates from 0 to 2.8 l/min were explored; for larger air flow rates the radial position of the droplet is no longer stable and the droplet may jump out of the node. For all of these measurements the evaporation rate β is determined and its evolution as a function of the ventilation flow rate can be seen in fig. 3.16. Different domains can be distinguished in the curve:

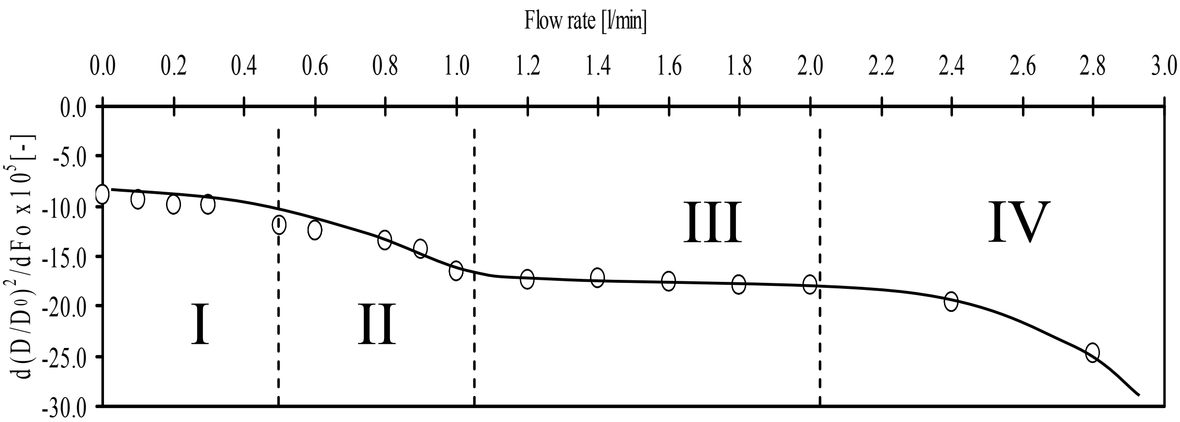

Figure 3.16: Evaporation rate versus air flow rate (water droplet of $1 \mu l$ initial volume).

I. 0.4 l/min <: almost no variation of the evaporation rate can be seen.

II. 0.4 - 1.0 l/min: the evaporation rate increased significantly.

III. 1.0 - 2.0 l/min: nearly no effect of blowing can be observed.

IV. 2.0 l/min >: the evaporation rate starts to increase again with the air flow rate.

The results obtained in fig. 3.16 can be explained by taking into account the influence of the acoustic streaming. In zone I, the evaporation is reduced due to the vapor enrichment of the droplet neighborhood. The vapor coming from the droplet surface is trapped by the vortices of the outer acoustic streaming (see fig. 3.13). In zone II, the ventilation is enough to deplete the vortices and therefore the evaporation rates increase strongly. The air flow must be greater than 0.4 l/min to influence the surface of the droplet. In zone III, the depletion of the vortices is completed. The mass transfer is driven only by the inner acoustic streaming that behaves like a 'shield' preventing the air flow to reach the droplet surface. In zone IV, the ventilation-driven convection begins to play a significant role in the mass transfer. One can expect that the experimental data obtained in zone 3 might be described by Yarin model, which considers an acoustically-driven mass transfer at constant ambient vapor concentration. This assumption is verified by comparing the simulation results to the experimental surface measurements for different air flows as depicted in fig. 3.17. Good agreement can be noticed for flow rates of 1.0 and 1.2 l/min. An experiment with methanol is carried out for a ventilation of 1.2 l/min, i.e. in the middle of zone III. As shown in fig. 3.17, the experimental results are well predicted by the model.

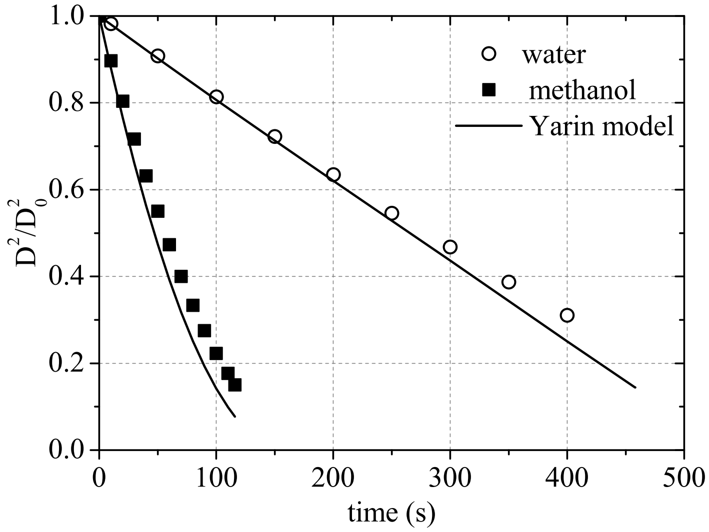

Figure 3.17: Temporal evolution of the normalized drop surface for water and methanol droplets with an initial volume of $1.5\mu l$, $1.1\mu l$ and initial SPL of 163.7 dB, 162.3 dB, respectively.

Visualization of the acoustic streaming

Visualizing of the acoustic streaming has been carried out by many researchers (Trinh et al., 1996, Kastner et al., 2001); however Kastner (2001) visualized the outer acoustic streaming around droplet in a tube acoustic levitator. The tube surrounds the droplet, reflector and the transducer, and has a diameter of 12 mm and height of 30 mm.

In order to visualize acoustic streaming around a droplet levitated in an open acoustic levitator, a continuous laser beam generated from 100 mW Nd:YAG and an arrange-

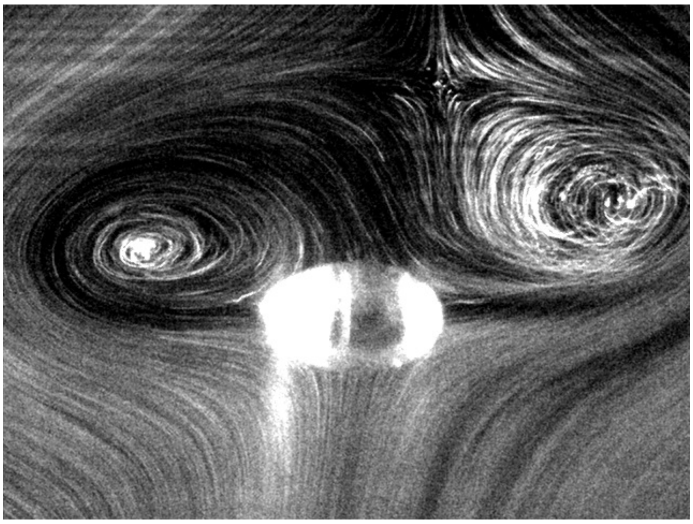

Figure 3.18: Visualization of the acoustic streaming induce by water droplet at ambient temperature of 24 °C, an air mixed with seeding particles is illuminated by laser sheet, droplet volume $2\mu l$.

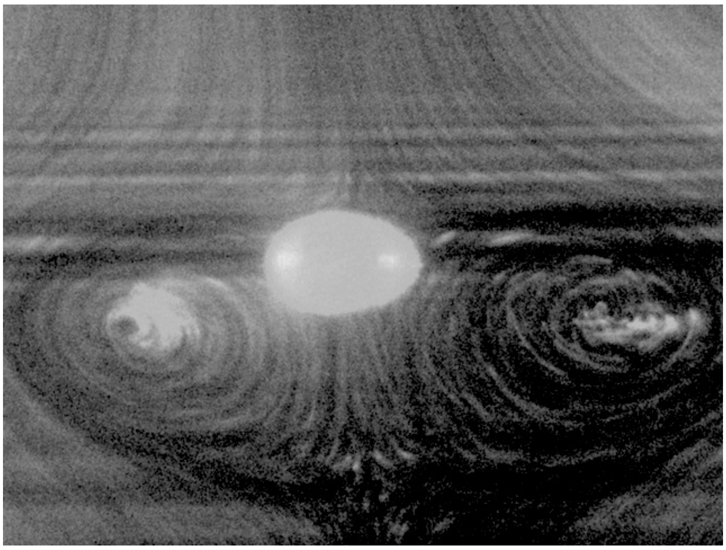

Figure 3.19: Visualization of the acoustic streaming induce by water droplet at ambient temperature of 24 °C, the transducer is located below the droplet.

ment of cylindrical and spherical lens is used to generate a laser sheet of 200 μm thickness. The laser sheet illuminates the area between the second and the third node in the acoustic field. A water droplet of 2 μl is inserted in the acoustic field using a microliter syringe. The volume of the double-wall glass chamber used in our experiments is much larger than the glass tube used by Kastner (2001). Therefore, a seeding system consisting of pressurized air oil seedings is used to purge the glass chamber with the seeding particles. Once the chamber is filled, the air flow is turned off so that the air flow doesn't disturb the acoustic streaming and the visualization becomes possible. Finally, a CCD camera is set perpendicular to the laser sheet and a sequence of images are recorded. As shown in fig. 3.18, the streaming around water droplet (aspect ratio $d_h/d_v = 1.25$) is displayed, the estimated vortex size is two times the droplet diameter. The bright spots in droplet poles are the over-exposed pixels resulting from higher laser intensity, the droplet will be also heated up due to the energy received from the laser beam. It has been noticed that the acoustic streaming below the droplet was difficult to visualize at the same time with the upper acoustic streaming. Note that the transducer is located above the droplet. Moreover, the scattering of the acoustic field because of the droplet and from the reflector surface may result in a lower intensity of the acoustic streaming below the droplet. However, by turning the levitator upside down the acoustic streaming below the droplet can be visualized (see fig. 3.19). The non-symmetry of

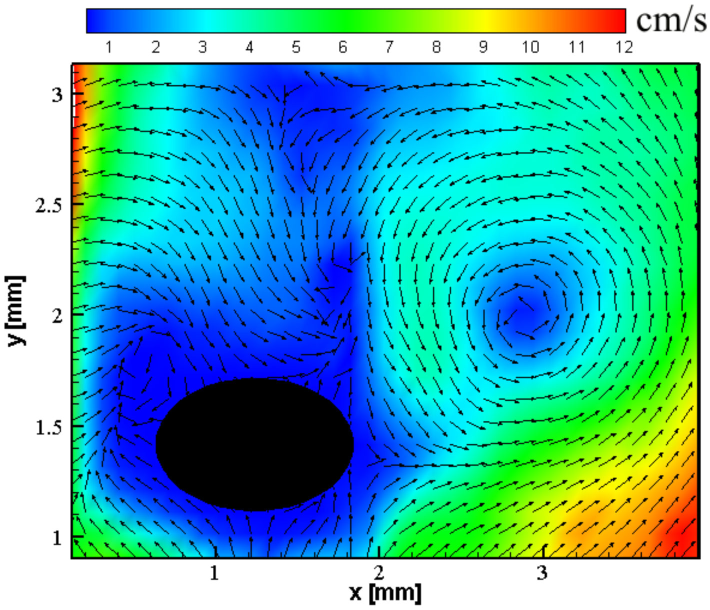

Figure 3.20: PIV image of the outer acoustic streaming of water droplet of 2 μl, the seeding particles are illuminated by laser sheet,ambient temperature 24 °C, velocity measured in cm/s. The non-symmetry of the outer acoustic streaming around the droplet is due to the incoming air flow that inserted into the glass chamber to keep a constant concentration of the seeding particles.

the outer acoustic streaming around the droplet comparing to the theoretical predictions (see fig. 3.13) is due to the incoming air flow that inserted into the glass chamber in order to have a constant concentration of the seeding particles, the images of the outer streaming can be then captured by the camera.

Previous measurements are qualitative, and further measurements have been conducted to quantify the velocity, orientation and influence of the ventilation on the outer acoustic streaming. Particle image velocitmetry (PIV) has been used. This is a technique where planer laser sheet is produced by 30 mJ Nd:YAG laser of 10 ns pulsed length. The laser beam is pulsed twice. Using a high speed and high-resolution SENSICAM camera set perpendicular to the light sheet, images of fine particles lying in the light sheet are recorded at frequency of 30Hz, the time step between the two pulses being 150 μs. From the recorded images, the velocity magnitude and direction are extracted. As displayed in fig. 3.20, the outer acoustic streaming around a water droplet of 2 μl at a ventilation rate of 0.0 l/min. The streaming rotates in counter clock wise manner moves from the north pole entering the region near droplet equator and then moves outward. Figure 3.21 shows PIV measurements at 1.00 l/min.

Based on the analysis from Yarin et al. (1999), for a droplet of 1.3 mm initial diameter

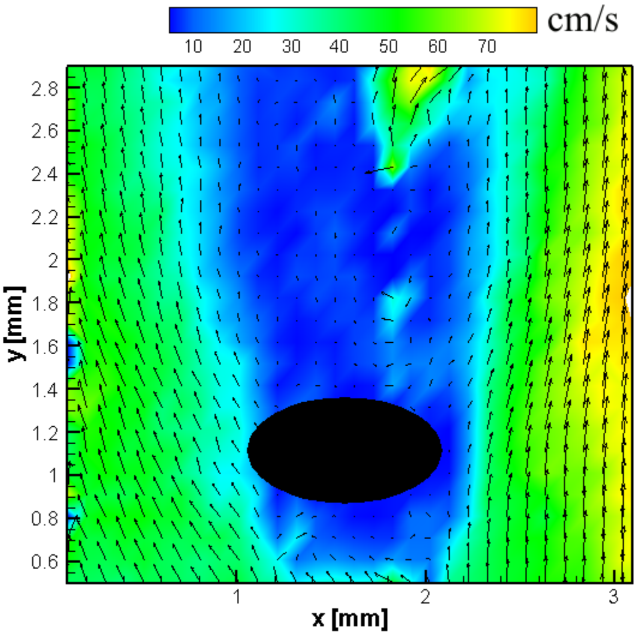

Figure 3.21: PIV image of the of water droplet in the acoustic field, the droplet is ventilated with an air flow rate of 1 l/min (Re = 93), the outer acoustic streaming are blown out (destroyed). velocity measured in cm/s.

and vertical distance of 0.8 cm, the air velocity that droplet would experience if a reflector with central hole of 1 mm diameter is used and a purging flow of 1 l/min can be estimated as:

$$V_{nozzle} = \frac{\dot{V}}{\pi/4d^2_{nozzle}} \tag{3.34}$$

where V_{nozzle} is the air velocity at the nozzle exit, d_{nozzle} is diameter of the nozzle (or hole diameter in case of reflector with multiholes) and $\dot{V}$ if air flow rate (l/min).

The air velocity at the nozzle exit will decrease along the flow axis and along the horizontal cross-section of the jet, the maximum air velocity that would experienced by the droplet (Yarin et al., 1999):

$$V_{drop,max} = \frac{V_{nozzle}}{\alpha^* + 1} \tag{3.35}$$

where α^* is defined as the ratio of the vertical distance between droplet and reflector

(l_y) to the polar distance of the jet, which reads as:

$$\alpha^* = \frac{23.0 \cdot l_y}{d_{nozzle}^2 V_{nozzle} / \nu_0} \tag{3.36}$$

For a droplet of 1.3 mm initial diameter,$\dot{V} = 1\ l/min$, $l_y = 0.8\ cm$, $d_{hole} = 420\ \mu m$ and number of holes in the reflector is 40 holes. The air velocity $V_{nozzle} = 300\ cm/s$ and hence $V_{drop,max} = 48\ cm/s$. As depicted in fig. 3.21, it can be seen that the predicted velocity by eqn. (3.35) is a good approximation. Moreover, the outer acoustic streaming is destroyed, which confirms the working zone obtained in fig. 3.16 to conduct our experiments.

3.4 Reflector geometry

The reflector can be of different shapes i.e. flat, concave, with central hole, nozzle or even with an array of multi-holes. The geometry of the reflector depends on the application, a reflector with bore hole can also serve as a jet nozzle when a gas stream is to be blown axially against the levitated sample.

A separate and exchangeable gas nozzle integrated into the reflector provides a better defined free jet flow and, thus, allows a combination of ultrasonic and aerodynamic levitation (Weber et al., 1993, Yarin et al., 1997).

The reflector with concave shape helps to reduce scattering and concentrates the acoustic wave when it is reflected back. The reflector geometry can be also flat. Even the degree of the curvature can play a significant roll in creating an intense acoustic field (Xie and Wei, 2001, Xie et al., 2002).

To investigate the influence of reflector shapes on the levitation stability and also ventilation efficiency different types of reflectors have been tested. As shown in fig. 3.22 different shapes of reflectors can be used to levitate samples, however, the stability of the levitation is increased for parabolic reflector as most of the acoustic wave is reflected and concentrated into the transducer. Xie and Wei (2001) showed that maximum acoustic force is a function of the reflector shape and by modifying the reflector geometry and transducer, even a sphere of heavy metals can be levitated.

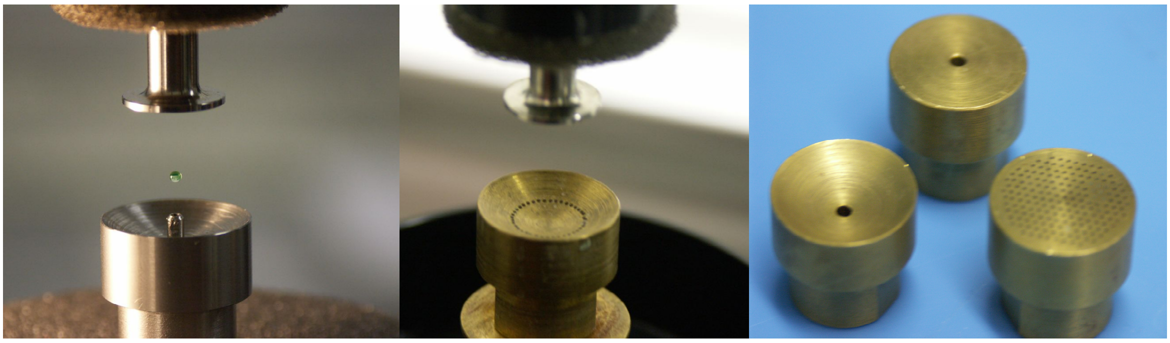

Figure 3.22: Reflectors of diffrent geometries, parabolic, flat or reflector with Nozzel can be used to levitate droplets or spheres in the acoustic field.

The distance between reflector and the transducer is 1.65 cm. Within this distance, the levitation of liquid droplet using a reflector with nozzle became unstable when applying purging flow from the bottom. Even for small flow rate, the droplet will start to oscillate and may jump out of the acoustic field.

Therefore we used a reflector with array of annular holes, the air flow coming out from the reflector will surround the droplet and helps to remove the vapor form the outer acoustic streaming.

Chapter 4

Evaporation of Single Droplets: Pure Liquids

In this chapter, the basic principles of droplet evaporation will be addressed. The film theory model, the D^2-Law and experimental results of evaporation in the acoustic field will be presented. Comparisons with model predictions as well as with droplet evaporation suspend by glass filament are discussed.

4.1 Evaporation model

The evaporation of pure liquid droplets are described by simple evaporation models based on the film theory introduced by (Bird et al., 1960). In the film theory, the entire resistance to mass transfer is assumed to be equivalent to a thin, stagnant region at the interface between the liquid and the gas phase.

As shown in fig. 4.1, within the film, heat is transported solely by diffusion towards the droplet in exchange for mass diffusion from the evaporating droplet in the opposite direction. The film is surrounded by two boundaries. The outer boundary is noted with the subscript ∞ represents the conditions far away from the droplet. In fig. 4.1, the dominant parameters for heat and mass transfer, the temperature, T and the mass fraction, Y_c are indicated. In order to apply the film theory concept the following assumptions have to be considered:

I. Within the film, thermophysical properties are supposed spatially uniform and no chemical reactions are involved.

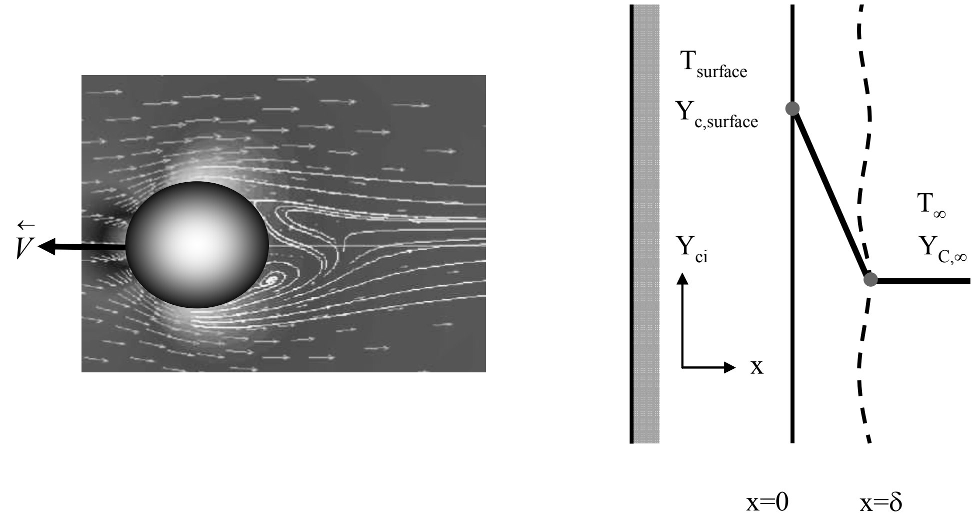

Figure 4.1: Concentration/Temperature profile inside a gas film of thickness δ according to the concept of film theory.

II. The pressure drop influence on the gas phase physical properties is negligible.

III. The temperature and concentration distribution are uniform along the droplet surface and depend only on the distance from the surface, at $x = 0$, $T = T_{surf}, Y_c = Y_{surf}$ and at $x = \delta$, $T = T_\infty, Y_c = Y_{c,\infty}$.

IV. Inside the film the flow is laminar and all transport properties, such as the diffusion coefficient or the thermal diffusivity, are considered constant.

V. Film thickness δ, is assumed to be constant along the surface and independent of the mass transfer rate. Both δ_T and δ_c are adjusted so that the diffusion of the species and conduction of heat inside the film are equal to actual flows exchanged by convection between droplet and the external environment.

For a non-vaporizing droplet, the thickness thermal and diffusional films are defined as:

$$\delta_{c0} = \frac{2 \cdot r_s}{Sh_0 - 2}, \qquad \text{and} \qquad \delta_{T0} = \frac{2 \cdot r_s}{Nu_0 - 2} \tag{4.1}$$

where Sh_0 and Nu_0 are Sherwood and Nusselt numbers, which are defined as a non-dimensional heat and mass transfer coefficients:

$$\begin{aligned} Sh &= \frac{D\frac{\partial Y}{\partial r}|_s}{Y_\infty - Y_s} \\ Nu &= \frac{D\frac{\partial T}{\partial r}|_s}{T_\infty - T_s} \end{aligned} \tag{4.2}$$

Abramzon and Sirignano (1989) developed a model based on the film theory to account for the effect of the convective transport caused by droplet motion relative to the gas and the effects of the blowing (Stefan flow), a correction factor is introduced:

$$F_c = \frac{\delta_c}{\delta_{c0}}, \text{ and } F_T = \frac{\delta_T}{\delta_{T0}} \tag{4.3}$$

F_c and F_T represent the relative change of the film thickness due to Stefan flow. At the droplet surface the liquid vapor flowrate conservation equation may be written by:

$$\dot{m}_v = \dot{m}_v Y_s - \pi D^2 \rho_g \mathscr{D}_g \left.\frac{\partial Y_{vap}}{\partial r}\right|_s \tag{4.4}$$

where Y_{vap} is the mass fraction at the droplet surface which is supposed to be uniform, substitute eqn. (4.2) in eqn. (4.4) and re-arrange:

$$\dot{m}_v = \pi D \rho_g \mathscr{D}_g Sh \left(\frac{Y_{vap,s} - Y_{vap,\infty}}{1 - Y_{vap,\infty}} \right) \tag{4.5}$$

where B_M is the Spalding mass transfer coefficient:

$$B_M = \frac{Y_{vap,s} - Y_{vap,\infty}}{1 - Y_{vap,\infty}} \tag{4.6}$$

The basic phase equations for the conservation of mass, species and energy read as follows (Bird et al., 1960):

$$\frac{d}{dr}(\rho_g \cdot r^2 \cdot U(r)) = 0 \tag{4.7}$$

where U is the radial velocity of the gas surrounding the droplet. Integration of eqn.

(4.7) yields:

$$r^2\rho_g U(r) = \frac{\dot{m}_v}{4\pi} = constant \tag{4.8}$$

the conservation of the species(vapour) of the evporating component:

$$\frac{d}{dr}\left(r^2 \cdot \rho_g \cdot U_r \cdot Y_{vap}\right) = \frac{d}{dr}\left(r^2 \cdot \rho_g \cdot \mathscr{D}_g \cdot \frac{dY_{vap}}{dr}\right) \tag{4.9}$$

substituting eqn. (4.7) into eqn. (4.9) and re-arranging the resulted equation gives the following differential equation:

$$-\frac{dY_{vap}}{1-Y_{vap}} = \frac{\dot{m}_v}{4\pi\rho_g\mathscr{D}_g}\frac{dr}{r^2} \tag{4.10}$$

integrating eqn. (4.10) along the film thickness δ with boundary conditions:

$$\begin{aligned} Y_{vap} &= Y_{vap,s} \qquad at \qquad r = r_s \\ Y_{vap} &= Y_{vap,\infty} \qquad at \qquad r = r_{f,M} \end{aligned} \tag{4.11}$$

$$\ln\left(\frac{1-Y_{vap,\infty}}{1-Y_{vap,s}}\right) = -\frac{\dot{m}}{4\pi\rho_g\mathscr{D}_g}\left(\frac{1}{r_{f,M}} - \frac{1}{r_s}\right) \tag{4.12}$$

re-arrange eqn. (4.12) for $\dot{m}$:

$$\dot{m}_v = 4\pi r_s^2\rho_g\mathscr{D}_g \ln(1+B_M) \cdot \frac{r_{f,M}}{R_s(r_{f,M}-r_s)} \tag{4.13}$$

or

$$\dot{m}_v = \pi D\rho_g\mathscr{D}_g \ln(1+B_M) \cdot \frac{r_{f,M}}{r_s(r_{f,M}-r_s)} \tag{4.14}$$

and by considering the energy flux between the droplet and the surrounding gas $\dot{m}_v$ is defined in terms of Nu^* and B_T (Abramzon and Sirignano, 1989):

$$\dot{m}_v = \pi D \frac{\lambda_g}{C_{p,F}} \ln(1+B_T) \cdot \frac{R_{f,T}}{r_s(R_{f,T}-r_s)} \tag{4.15}$$

where λ_g and $C_{p,F}$ are the thermal conductivity of the gas mixture and the vapor specific heat int the film, respectively. B_T is the spalding heat transfer coefficient:

$$B_T = \frac{C_{p,F}(T_\infty - T_s)}{L(T_s) + \dot{Q}_L/\dot{m}} \tag{4.16}$$

where $L(T_s)$ is the latent heat of vaporization at temperature T_s and $\dot{Q}_L$ is the heat transferred into the droplet. by comparing eqn. (4.13) to eqn. (4.5):

$$Sh = \frac{\ln(1+B_M)}{B_M} \cdot \frac{r_{f,M}}{(r_{f,M}-r_s)} \tag{4.17}$$

The second term of RHS of eqn. (4.17) with the help of eqn. (4.1) and eqn. (4.3) can be written as:

$$\begin{aligned} \frac{r_{f,M}}{(r_{f,M}-r_s)} &= \frac{2(r_s-\delta_c)}{\delta_c} \\ &= 2 + \frac{2 \cdot r_s}{F_c \delta_{c0}} \end{aligned} \tag{4.18}$$

When taking into account the effect of the evaporation, the Nusselt and Sherwood Numbers of isolated droplet can be rewritten according to Abramzon and Sirignano (1989) in the following way:

$$Sh = \left[2 + \frac{Sh_0 - 2}{F(B_M)}\right] \frac{\ln(1+B_M)}{B_M} \tag{4.19}$$

$$Nu = \left[2 + \frac{Nu_0 - 2}{F(B_T)}\right] \frac{\ln(1+B_T)}{B_T} \tag{4.20}$$

The Modified Sherwood and Nusselt numbers are defined as:

$$Sh^* = \left[2 + \frac{Sh_0 - 2}{F(B_M)}\right] \tag{4.21}$$

$$Nu^* = \left[2 + \frac{Nu_0 - 2}{F(B_T)}\right] \tag{4.22}$$

$F(B)$ is a function introduced by Abramzon and Sirignano (1989) which is a universal function that depends on B_M and B_T:

$$F(B) = (1+B)^{0.7}\frac{\ln(1+B)}{B} \tag{4.23}$$

By rewriting eqn. (4.1) for Sh^* and Nu^*, the radii of the thermal and diffusional film defined as:

$$\begin{aligned} r_{f,M} &= \frac{r_s Sh^*}{Sh^* - 2} \\ r_{f,T} &= \frac{r_s Nu^*}{Nu^* - 2} \end{aligned} \tag{4.24}$$

Sh_0 and Nu_0 are empirical functions and defined as:

$$Sh_0 = f(Re, Sc) \tag{4.25}$$

$$Nu_0 = f(Re, Pr) \tag{4.26}$$

Re, Pr and Sc are respectively the Reynolds, Prandtl and Schmidt numbers.

Heat transfer into droplet

The droplet enthalpy evolution is controlled by the variation of the heat fluxes resulting from forced convection with the surrounding gaseous environment and vaporization. The energy balance can be written as:

$$Q_C = Q_{vap} + Q_L \tag{4.27}$$

where Q_C is the convective heat flux exchanged with the gaseous environment, Q_L is the heat flux entering into the liquid phase and Q_{vap} is the heat flux due to vaporization defined by:

$$Q_{vap} = \dot{m} \cdot L_v \tag{4.28}$$

In this expression, the vapor flow rate $\dot{m}$ is of positive sign and L_v is the latent heat of vaporization. Assuming that the temperature at the droplet surface is uniform, the convective heat flux exchanged with the surrounding gas phase at the droplet surface is defined by:

$$Q_C = A_s \cdot h_T (T_{gas} - T_s) \tag{4.29}$$

where h_T is the convective heat transfer coefficient defined by:

$$h_T = \frac{Nu \lambda_g}{D} \tag{4.30}$$

A_s is the droplet surface area and T_{gas} is the ambient temperature corresponding to the gas phase temperature surrounding the droplet which characterizes the heat exchanged between the droplet and its environment.The instantaneous vapor flow rate reads :

$$\dot{m}_v = \pi D \rho_g \alpha_g B_T Nu \tag{4.31}$$

where α_g is the gas thermal diffusivity, ρ_g is the gas density and B_T is the Spalding heat transfer number defined by:

$$B_T = \frac{C_{p,F}(T_\infty - T_s)}{L(T_s) + Q_L/\dot{m}} \tag{4.32}$$

where $L(T_s)$ is the latent heat of vaporization at temperature T_s and Q_L is the heat transferred into the droplet. The comparison between the two expressions, eqn. (4.14) and eqn. (4.31) leads to the following non-dimensional overall energy balance:

$$B_T Nu = Le B_M Sh \tag{4.33}$$

where Le is Lewis number defined by $Le = \frac{\mathscr{D}_g}{\alpha_g}$.

4.2 The D^2-Law

The classical D^2-law is discussed in extensive review by Faeth (1977) and Law (1982). It predicts that the square of the droplet diameter decrease linearly with time. Few assumptions of the D^2-Law must be considered for an evaporating droplet such as: heat and mass transfer between liquid and gas phase are diffusion controlled, spherical symmetry, single liquid component, no Soret, Dufour, or radiation effects take place and, finally, constant and uniform temperature (transient stage of droplet temperature is neglected). In the previous section the mass flux of vapor leaving the droplet surface is calculated, the rate change of liquid droplet mass is expressed as follows:

$$\begin{aligned} \dot{m}_d &= -\frac{dm_d}{dt} \\ \frac{dm_d}{dt} &= -\rho_{drop}\frac{dV}{dt} \\ &= -\rho_{drop}\frac{\pi}{6}\frac{dD_s^3}{dt} = -\rho_{drop}\frac{\pi D}{4}\frac{dD_s^2}{dt} \end{aligned} \tag{4.34}$$

but $\dot{m}_v = -\dot{m}_d$, comparing eqn. (4.14) and eqn. (4.34):

$$\frac{dD^2}{dt} = -4\frac{\rho_g}{\rho_{drop}}\mathscr{D}_g Sh^* \ln(1+B_M) \tag{4.35}$$

for diffusion controlled evaporation the film thickness goes into infinity, hence from eqn. (4.1), $Sh_0 = 2$, the modified Sherwood number Sh^* takes the value 2 after substituting the value of Sh_0 in eqn. (4.21), eqn. (4.35) becomes:

$$\frac{dD^2}{dt} = -8\frac{\rho_g}{\rho_{drop}}\mathscr{D}_g \ln(1+B_M) \tag{4.36}$$

the integration of this equation for an initial condition D_0 at $t = 0$ gives the well known D^2-Law that describe the temporal evolution of droplet surface of pure liquid: z

$$D^2 = D_0^2 - \beta t \tag{4.37}$$

where β is the evaporation rate:

$$\beta = 8 \frac{\rho_g}{\rho_{drop}} \mathscr{D}_g \ln(1 + B_M) \tag{4.38}$$

In addition to the evaporation rate, another important parameter in droplet evaporation is the lifetime of the droplet, also called evaporation time τ_{end} , which can be determined from eqn. (4.37) with $D|_{(t\, =\, \tau_{end})} = 0$:

$$\tau_{end} = D_0^2 / \beta \tag{4.39}$$

4.3 Empirical correlations of Sherwood and Nusselt numbers

The prediction of droplet diameter evolution by D^2-Law is a classic way to model droplet evaporation, Different empirical correlations were developed to account for evaporation of droplet by forced convection, natural convection or even under the influence of the acoustic filed. These corrections are usually written in terms of a Sherwood number that relates mass transfer from moving drop to mass transfer from a stationary droplet, Frössling (1938) showed that for mass transfer from a drop undergoing forced convection should vary approximately linearly with $Re^{1/2}Sc^{1/3}$.

$$\begin{aligned} Sh &= 2 + f_1 Re^{1/2} Sc^{1/3} \\ Nu &= 2 + f_2 Re^{1/2} Pr^{1/3} \end{aligned} \tag{4.40}$$

To find the constant of proportionality, many researchers have investigated the evaporation of drops suspended from a support in a flowing air stream. Frössling (1938) investigates droplets with diameter up to 1.8 mm, at different air velocity. According to his theoretical consideration Sherwood number reads:

$$Sh = 2 + 0.522 Re^{1/2} Sc^{1/3} \tag{4.41}$$

Ranz and Marshall (1952a,b) studied the evaporation of a single droplet suspended by glass filament varying the air flow rate, temperature and the initial diameter of the droplets. The correlation factor for forced convection is given by:

$$\begin{aligned} Sh &= 2 + 0.6 Re^{1/2} Sc^{1/3} \\ Nu &= 2 + 0.6 Re^{1/2} Pr^{1/3} \end{aligned} \tag{4.42}$$

and for natural convection:

$$\begin{aligned} Sh &= 2 + 0.6 Gr^{1/4} Sc^{1/3} \\ Nu &= 2 + 0.6 Gr^{1/4} Pr^{1/3} \end{aligned} \tag{4.43}$$

where Gr is Grashof number.

Yarin et al. (1999) developed new correlations for Sherwood and Nusselt number that take into account the acoustic boundary layer surrounding a droplet levitated in the acoustic field. Both correlations are a function of the sound wave properties as well as droplet size and shape. The derivation of Sh is presented in Chapter 3:

$$\begin{aligned} Sh &= K_{ac} \frac{B}{(\omega_{ac} \cdot \mathscr{D}_g)^{1/2}} \\ Nu &= K_{ac} \frac{B}{(\omega_{ac} \cdot \alpha_g)^{1/2}} \end{aligned} \tag{4.44}$$

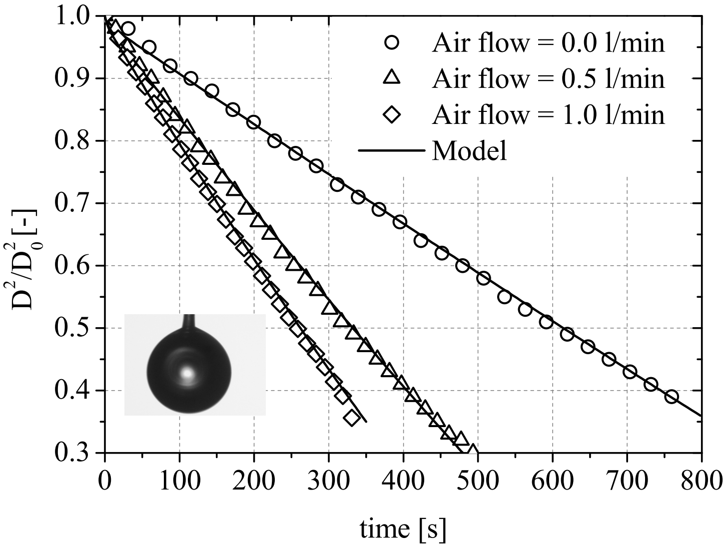

Figure 4.2: Temporal evolution of the surface area of water droplets suspended by glass filament, droplets are ventilated with an air flow 0.0 (diffusion controlled), 0.5 and 1.0 l/min, air ambient temperature is 23 °C and relative humidity is 10%, diameter of the glass filament is 200 μm and initial drop diameter D_0=1.38 mm.

4.4 Evaporation of droplets suspended by glass filament versus acoustic field

Evaporation of water droplets suspended by glass filament have already been investigated by many researchers (Ranz and Marshall, 1952a,b, Charlesworth and Marshall, 1960, Cheong et al., 1986, Lin and Chen, 2002). As depicted in fig. 4.2, different experiments of water droplet were suspended on the tip of thin glass rod (glass filament), which had a diameter of 200 μm.

The tip of the glass filament was coated with wax to prevent the water droplet from creeping up. The suspension of the drop by the tip glass filament has been done with the help of the acoustic force. First, the droplet is levitated in the air by the help of the acoustic force. Then the glass filament is inserted from a hole in the transducer. Once the droplet is attached to tip, the acoustic field is switched off. Using a CCD camera, a series of images were recorded. Fig. 4.2 shows the evaporation of the water droplet at 0.0 air flow(diffusion controlled evaporation). As the air flow rate is increased, the evaporation is driven by convection, as it appears in the second term of RHS of eqn.

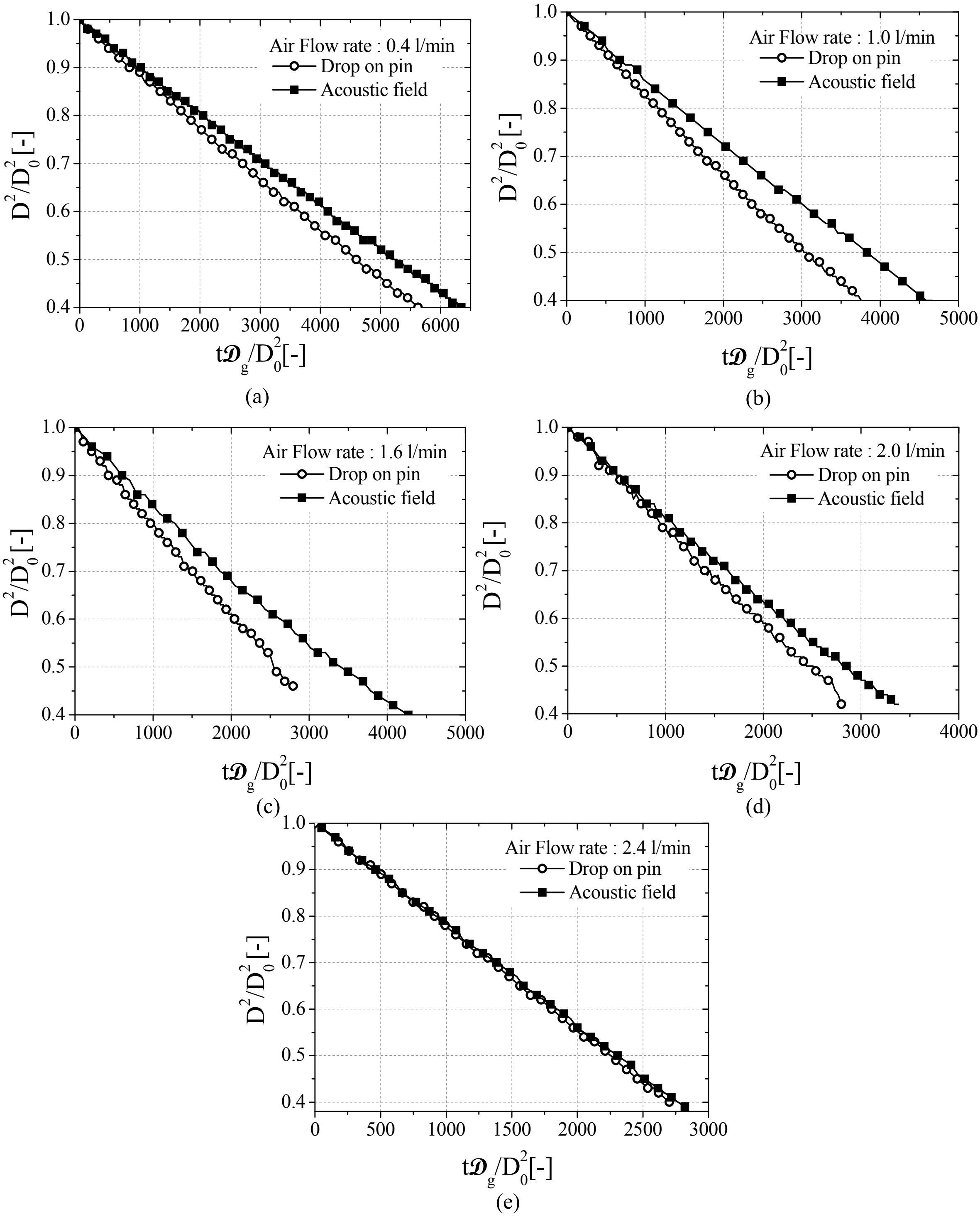

Figure 4.3: Comparison of droplet evaporation of water in standing acoustic wave versus droplet suspended by glass filament. Droplets are ventilated with an air flow. Air ambient temperature is 23 and relative humidity of 10%, diameter of the glass filament is 200μm, (a) 0.4 l/min (diffusion controlled), (b) 1.0 l/min, (c) 1.6 l/min and (e) 2.4 l/min.

(4.43) of Sherwood number. It can be seen that these experiments are well predicted by the model in both cases, diffusion controlled evaporation and convection driven evaporation.

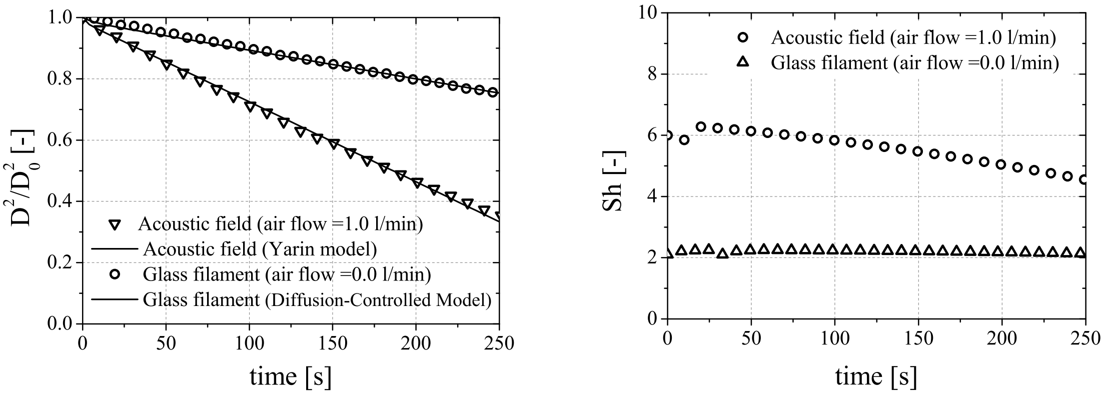

(a) (b)

Figure 4.4: Evaporation of water droplet. (a) Temporal evolution of normalized surface, both experiments compared with theory, controlled diffusion model and Yarin model (SPL_{eff} = 165.3), respectively. (b) Evolution of experimental Sh number for water droplet levitated by a standing acoustic wave, droplet initial diameter= of 1.2 mm, droplet is ventilated by an air flow of 1 l/min, and evaporation of droplet suspended by glass filament experiment, air flow =0.0 and initial drop diameter =1.3 mm. The ambient temperature is 23 °C, air relative humidity is 10%.

Actually, the film theory model is developed to account for high evaporation rate due to high temperature and/or high flow rate such as combustion processes (Sirignano, 1999), where in experiments conducted in the acoustic levitator the convection due to air flow can be predicted even with out applying the film theory modification.

The evaporation of droplets in the standing acoustic field is driven by the convection of the inner boundary layer, as described in chapter 3. A certain amount of air flow is required to blow out the outer acoustic streaming; hence, a comparison with the theoretical model is possible. Fig. 4.3 displays the evaporation curves for both, drop suspended on pin and drop levitated by the acoustic force while air flow rate is varied to scan for the whole range as depicted in fig. 3.16 i.e. 0.0 to 2.4 l/min. It can be seen that the evaporation rate for drop on pin experiment is always higher when comparing to the acoustic field case at the same blowing rate. This can be explained by the existence of the outer acoustic streaming which alters the far field conditions i.e. the vapor concentration near droplet surface. This is not the case for a drop on pin experiment.

As the air flow is increased to 2.4 l/min (which corresponds to zone 4 in fig. 3.16), the air flow is strong enough not only to blow out the vapor from the outer acoustic streaming but also to destroy the inner acoustic boundary layer. Now, the evaporation

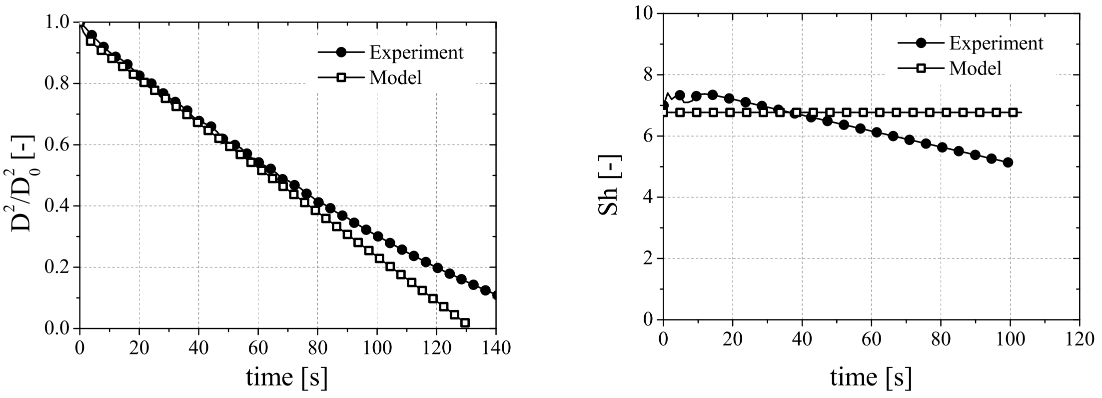

(a) (b)

Figure 4.5: Evaporation of ethanol droplet with initial volume of 1.6 μl in the acoustic filed, droplets are ventilated with an air flow 1.0 l/min, $SPL_{effective}$ = 162.8, air ambient temperature is 23 °C. (a) Temporal evolution of normalized surface, (b) Temporal evolution of Sherwood number.

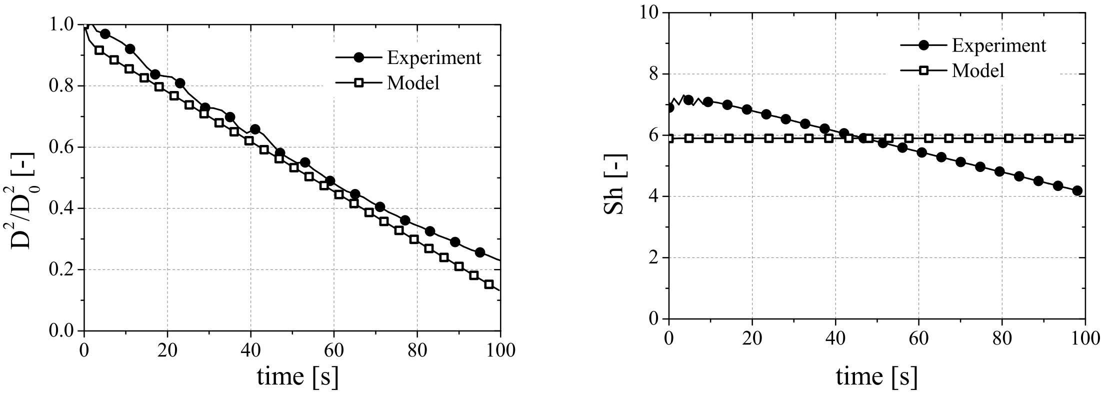

(a) (b)

Figure 4.6: Evaporation of a methanol droplet with initial volume of 1.4 μl in the acoustic filed, droplets are ventilated with an air flow 1.0 l/min, $SPL_{effective}$ = 162.6, air ambient temperature is 23 °C. (a) Temporal evolution of normalized surface, (b) Temporal evolution of Sherwood number.

in both experiments is driven by forced convection. However, the evaporation rate of the droplet due to the inner acoustic streaming i.e. air flow of 1 l/min, is higher than evaporation by diffusion-controlled case i.e. glass filament at 0.0 l/min. As displayed in fig. 4.4, Sherwood number for acoustic driven evaporation is three times larger than diffusion-controlled evaporation.

In figures 4.4, 4.5 and 4.6 different pure liquids, ethanol, methanol and water have been investigated. Temporal evolution ofthe normalized surface area and the Sherwood number are depicted. The experiments are compared to Yarin theory (Yarin et al., 1999).

Calculations are carried out at constant effective SPL_{eff} value, the volume and the axis ratio of the droplet are used to calculate the effective sound pressure level base on YPT model (Yarin et al., 1998), the constant value of the calculated Sherwood number is due to constant SPL_{eff} used in the model, moreover, the value of K (as defined in Sherwood number eqn. (4.44), depends on droplet volume, sound filed strength and droplet's shape. also it will change it's value upon droplet evaporation (Yarin et al., 1999), for small droplets it's approximated by the value 1.89.

Chapter 5

Drying of Single Droplets: Experiments

5.1 Colloid, suspension or solution

Drying of materials in food chemical and pharmaceutical industry includes different material types, which will influence the drying behavior and the drying kinetics of such materials, often, a mixture is a substance made by combining two or more different materials without a chemical reaction occurring, the mixture of the solvent and the solute is defined upon the size of the particles in the liquid phase, and the degree of solubility (Gekas, 1992). Defining those type of mixture take different definition from chemical point of view, typically there are three categories: colloids, solutions and suspensions.

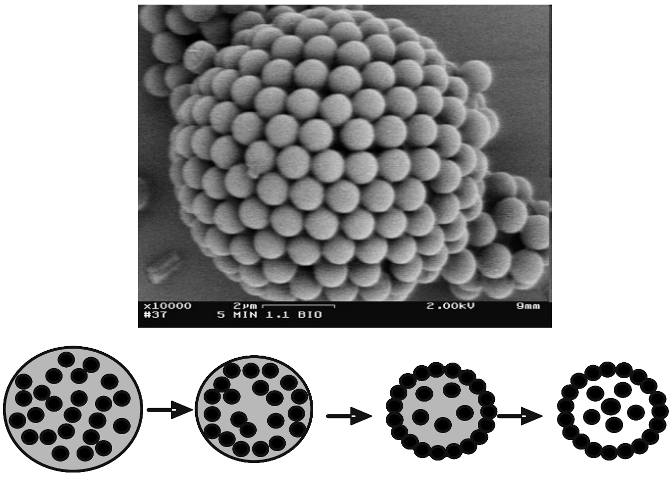

Figure 5.1: An electron microscope image of a "colloidosome," a water droplet coated in colloid (polystyrene) beads. (Image from David Weitz research laboratory at Harvard University)

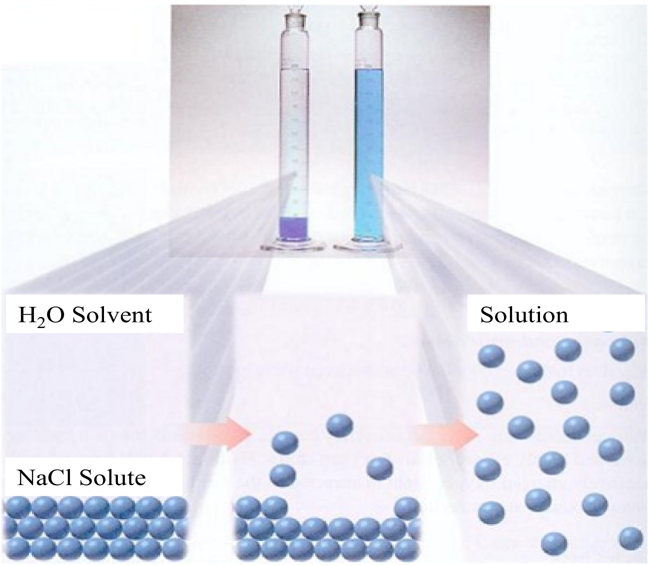

Figure 5.2: Schematic shows the dissolution of NaCl (solute) in water (solvent). As ions dissolve in the water, they spread out and become surrounded by water molecules.

Colloids are homogeneous mixtures, where small solid particles are dispersed in a gas phase, in this case it's called an aerosol and the particle size are less than $90\mu m$, if the solid particle is dispersed in liquid medium such as milk of coffee, the particle size could be in range of $1-10\mu m$, in both cases the solid particles are evenly distributed (Fuchs, 1964).

A suspension is defined as a heterogeneous fluid containing solid particles, the size of those particles is larger than in colloids. The particles will sediment some time after their introduction into the liquid phase. Solution is a homogeneous mixture in which the solute is dissolved in the other substance (solvent) such as salts in water.

5.2 Drying curves

Multiphase droplets exhibit upon drying, changes in many physical properties that influence the product and usage of the dried material, as the solvent evaporates the surface of the liquid recedes, until it reaches the point where the liquid must pass through the solid particles. However, this alters droplet density, viscosity and even at higher solid concentration a porous material emerges.

The drying procedure of a suspension drop can be divided in principle into at least two sections, the first section is characterized by a volume decrease due to the evaporation of the liquid. The droplet temperature reaches the wet bulb temperature — which is defined basically as the temperature that a bulb thermometer would measure if a flowing humid air stream passes a moist porous material (a wick) rapped around the bulb (Felder and Rousseau, 1986), wet bulb temperature depends on the humidity and the temperature of the air — assuming equilibrium between the wetted surface and the surrounding gas, i.e. air, the droplet sustains it's temperature as most of the heat is utilized to evaporate the moisture. As depicted in fig.5.3, the temperature of the evaporated droplet is plotted versus time.

The temperature path from point A to point C represents the first drying period. The end of the constant rate period is also designated by reaching the critical moisture concentration. The water moisture here, recedes inside the particle and the vapor at the end of this stage migrates through the pores to the particle surface. In the case of solutions the volume reduction ceases as soon as the crust is formed on the droplet surface at the end of the first drying section.

In the second section the volume and thus the surface of the drop/grain remains constant and the heat applied to the particle is large enough not only to evaporate the water but even to heat up the particles. The rise in temperature is seen in fig.5.3, point C to point F.

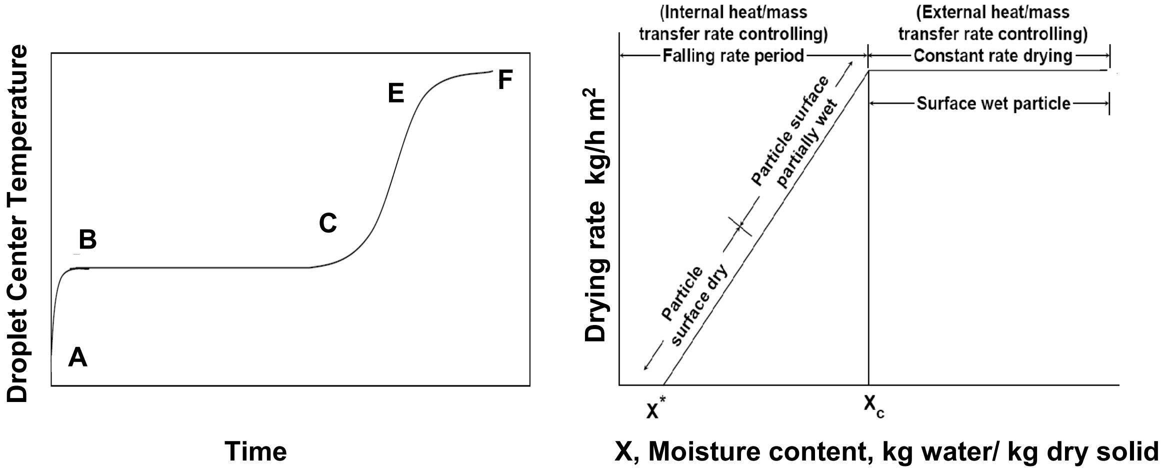

Figure 5.3: a) Drying curve represented by the temperature change of the droplet, Farid (2003). b) The moisture content is plotted versus drying rate. X_c is the critical moisture content where the falling rate period starts, Mujumdar (2006).

In the second drying period the evaporation rate determining step is the diffusion of the vapor in the crust, thus the crust porosity and thickness have to be considered for any model development (Mujumdar, 2006). Once the moisture concentration drops down to the equilibrium moist content the evaporation comes to the end of the falling rate period.

Figure 5.4 displays a set of experiments of drying of sodium sulfate aqueous solution. Two different initial concentrations have been investigated at three different air drying temperatures and relative humidities. It can be seen that for both initial concentrations investigated, increasing the relative humidity results in increasing the drying time of the droplet. For higher relative humidity values, the driving force of the vapor concentration at droplet surface become smaller.

The evaporation coefficient, β for each experiment at ambient air temperature of 28 °C and different values of RH are plotted in fig. 5.4f, β is calculated as defined by eqn. (4.37). It can be noticed that experiments conducted with different initial concentration exhibit the similar evaporation rate at the same relative humidity, the initial solid content determines, however the length of the constant rate period. For experiments carried out at higher temperatures, a faster evaporation rate is observed, as depicted in fig. 5.4e. For either higher temperatures or relative humidity values, the size of the droplet is identical when it enters the falling rate period and it depends only on the initial solid content.

The time when the constant rate period ends and the falling rate period starts is denoted as t_f. Table 5.1 shows the values of t_f recorded for each run; these values are compared with t_{th} which is the total time needed for a complete liquid depletion and formation a full solid grain. t_{th} can be calculated using a graphical method: the D^2 curve in the constant rate period is extended until it intersects with the time axis, where D^2 is equal

Table 5.1: Calculated time required to evaporate water from the multiphase droplet of aqueous solution, 10% initial concentration, t_f is the time at the end of the constant rate period extracted from the drying curves.

Temperature [°C]	t_f [s]	t_{th} [s] (eqn. (5.1))
28	300	402.72
40	212	288.71
55	110	186.65

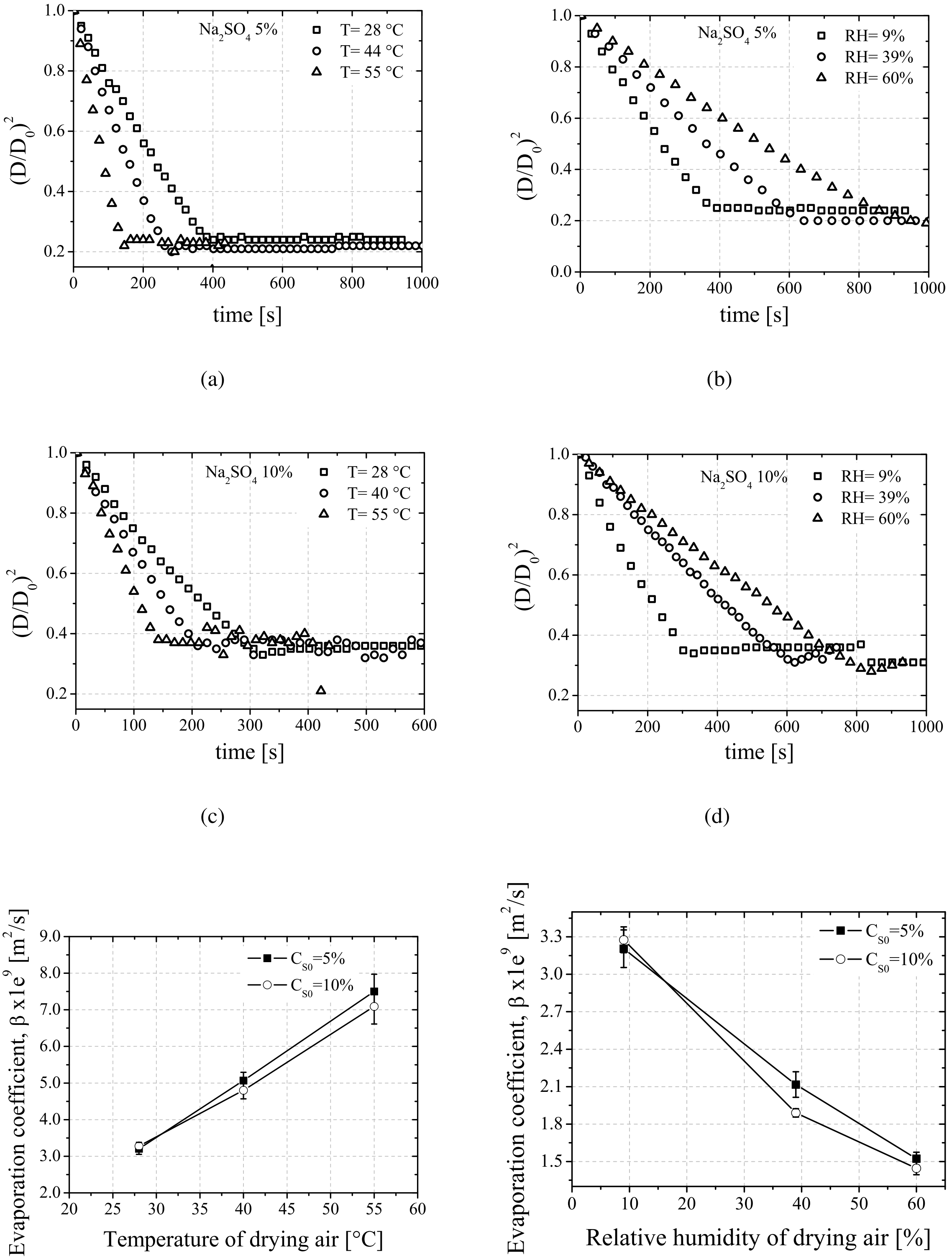

(a) (b)

(c) (d)

(e) (f)

Figure 5.4: Drying of sodium sulfate at different initial solid content, 5% and 10% respectively. Drying air temperature was varied between 28, 40 and 55 °C, relative air humidity set at three different values, 9, 39 and 60%. Droplets of 1.22 mm initial diameter. (e) and (f) show the evaporation coefficient β calculated from drying curve.

to the diameter of a solid sphere, i.e. the volume of the solid material. An estimation of total drying time, t_{th} can be calculated using the following equation, (Yarin et al., 2002b) and (Brenn, 2004):

$$t_{th} = \frac{d_0^2}{\beta}\left(1 - \left[\frac{C_{s0}\cdot\rho_w}{\rho_s + (\rho_w - \rho_s)C_{s0}}\right]^{2/3}\right) \tag{5.1}$$

where C_{s0} and ρ_s are the initial concentration and density of solid material respectively. The time t_f for each run depends on the drying air temperature, relative humidity and the initial solid content.

The time for the total water depletion t_{th} is plotted versus t_f for each initial concentration (C_{s0}, 5%, 10% and 20%). Actually, the time t_{th} predicts the total time for liquid evaporation assuming that evaporation will continues at the same evaporation rate i.e. D^2-law, therefore, it doesn't represent the actual time needed to evaporate the total amount of the liquid as it neglects the resistance of the crust to the evaporation of the liquid . The time t_{th} is then $t_f < t_{th} < t_{f,end}$, where $t_{f,end}$ is the time at the end of the second drying period. In the case of pure liquid evaporation $t_f = t_{th} = t_{f,end}$, fig. 5.5 shows all three different times for drying of multiphase droplet.

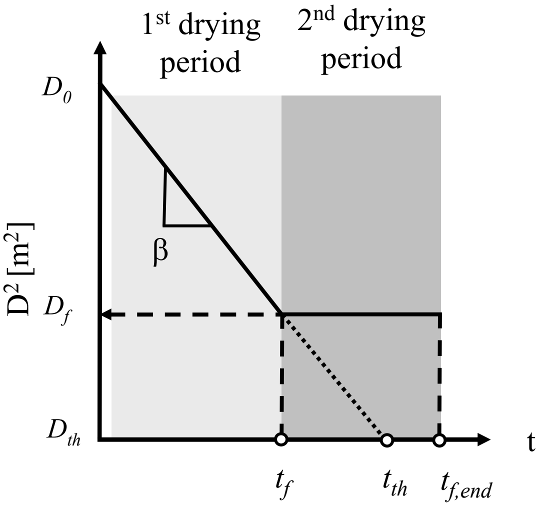

Figure 5.5: Predicted drying times for multiphase droplet.

The comparison between t_f and t_{th} which is depicted in fig. 5.6c, represent experiments carried out at air temperature of 40 °C.

The points correlate to a linear fit with regression $R^* = 0.98$. By repeating the same procedure for other temperatures, a linear fit with slope $A_f(ave.) = 0.43$ is obtained. A linear relation represents t_{th} as a function of t_f can be assumed, $t_{th} = A_T + A_f \cdot t_f$. The intersection A_T is a function of the operating temperature.

The correlation between t_f and t_{th} can be used then to *predict* the end of the first drying period by knowing the evaporation coefficient β and the initial concentration. This can then facilitate the modeling of the full drying time as it occurs in industrial operations.

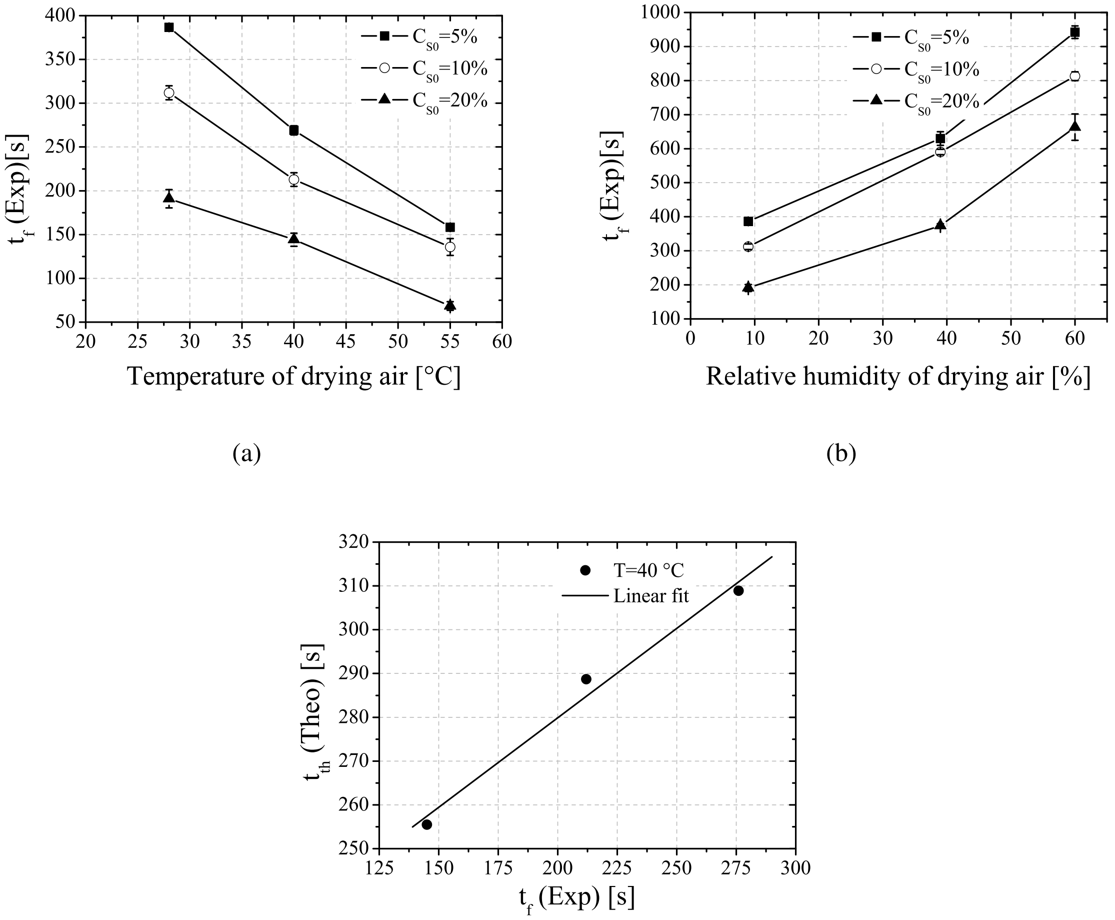

(a) (b)

(c)

Figure 5.6: Predicted time at the end of the constant rate period t_f plotted for a) different drying gas temperatures and b) different drying relative humidities. c) t_f is plotted versus t_{th} for different initial solid concentrations, experiments conducted at 40 °C.

The comparison of initial solid concentrations at a drying air temperature of 28 °C and a relative humidity of 9%, are displayed in fig. 5.7. The evaporation rate of each run in the constant rate period are almost equivalent. The constant rate period; however, is shortened for higher concentration as the shell builds up earlier.

The evaporation rate, $\frac{dm}{dt}$ in the first period can be calculated from the diameter evolu-

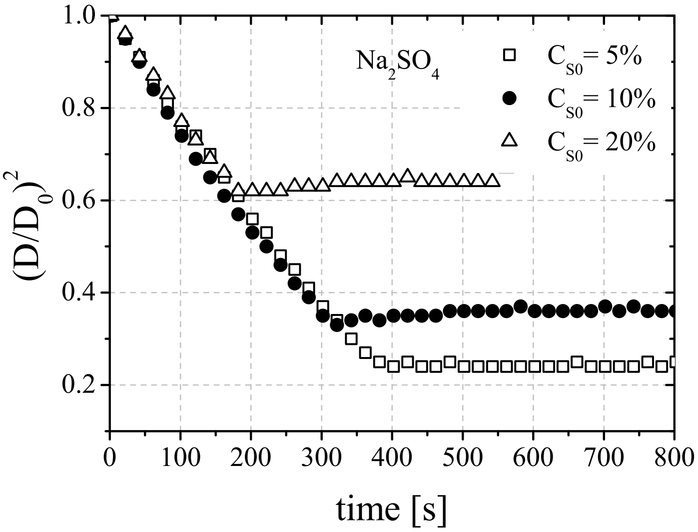

Figure 5.7: Drying of Na2SO4 aqueous solution (C_{s0}: 5%, 10% and 20%) at ambient air temperature of 28 °Cand RH=9%.

tion assuming wet bulb temperature and known liquid properties:

$$\left(\frac{dm}{dt}\right)_{const} = -\frac{\Delta V}{\Delta t} \tag{5.2}$$

where ΔV is the volume change of the droplet extracted from the meridian cross section of the droplet. As the falling rate period begins the diameter does not change; however, as the evaporation continues, the evolution of the vertical position of the droplet in the acoustic field will be used to calculate the drying rate in this period, as mentioned in chapter 3. For a constant volume, the change of droplet density due to solvent evaporation will reduce the droplet weight. The droplet then rises closer to the nearest pressure node above it's equator.

By monitoring the vertical evolution of the droplet position in the acoustic filed information about the mass transfer rate can be found. As depicted in fig. 5.8, the vertical position of the droplet shows a sharp change in the slope. At the end of linear part, when the vertical position and the volume is constant, the droplet is assumed to be totally dried. Once the droplet enters the falling rate period, experimental investigations (Kastner, 2001) have shown that the change in vertical position is a result of the density change of the droplet; the SPL value does not change as the droplet stays at constant volume and shape.

In order to calculate $\left(\frac{dm}{dt}\right)_{falling}$, the mass of moisture is assumed to be zero, all the water is evaporated (neglecting any residual moisture). The mass of the droplet at the beginning of the falling rate period is equal to the mass of the droplet at the end of the first stage, which can be extracted using eqn. (5.2) and the mass of the droplet (or particle) is equal to the mass of solid at the end of the falling rate period. As stated above, since the vertical position in the second period is function of density only, every point in the vertical curve in the second stage represents a decrease in the droplet mass, $\left(\frac{dm}{dt}\right)_{falling}$ is then calculated as (Kastner 2000):

$$\left(\frac{dm}{dt}\right)_{falling} = \frac{m_{const,end} - m_{falling,end}}{Vpos_{const,end} - Vpos_{falling,end}} \cdot \frac{Vpos_{falling,t} - Vpos_{const,end}}{t - t_f} \tag{5.3}$$

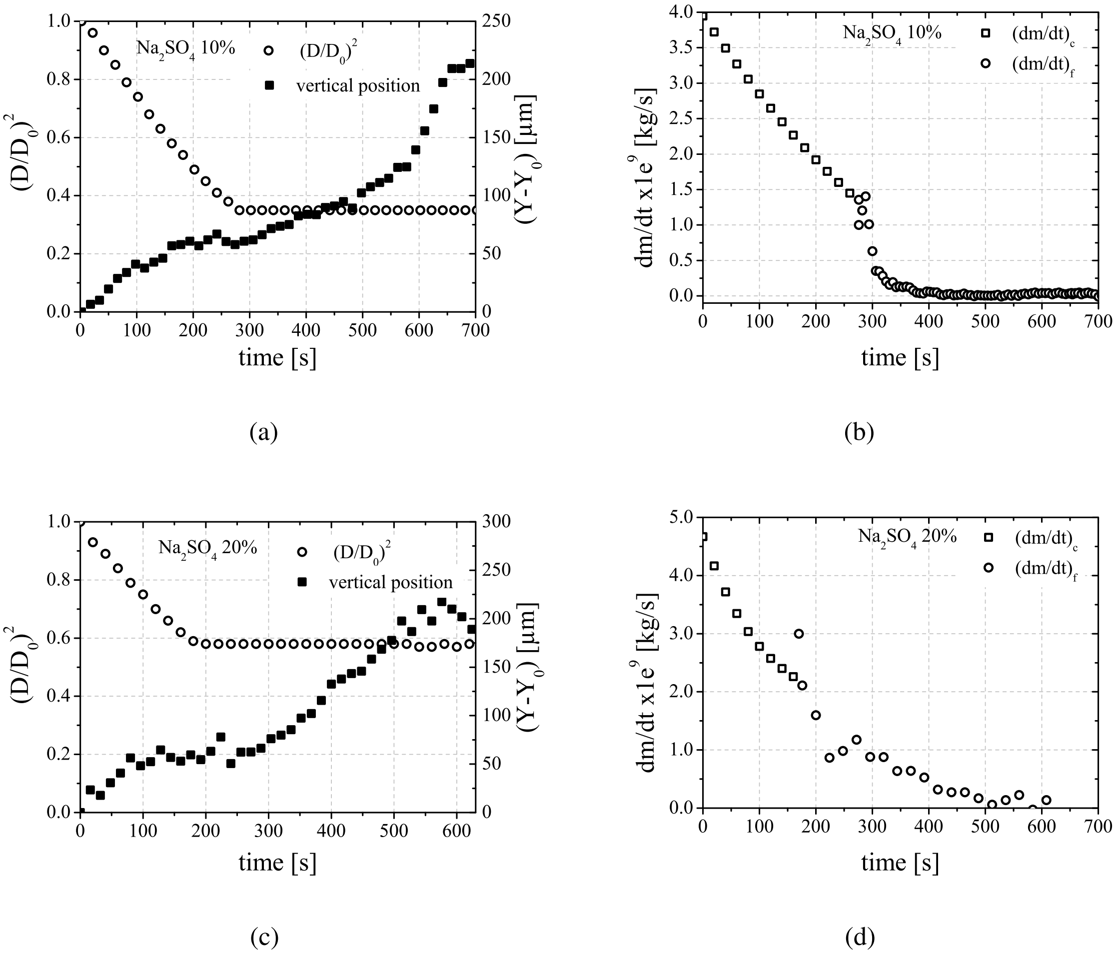

(a)

(b)

(c)

(d)

Figure 5.8: Experimental measurements of drying of multiphase droplet (a), (c) drying curves and evolution of vertical position for 0.1 and 0.2 initial solid content of sodium sulfate, (b) and (d) shows the extracted data of the mass transfer rate in the constant and falling rate periods.

5.3 Drying of suspension solutions

Two different materials have been investigated, skim milk and soyabase. The initial concentration was varied for both materials. As shown in fig. 5.9 the initial concentration effects clearly the duration of the first drying period, being shorter for higher initial concentrations. The rise in vertical position relative to the adjacent pressure node indicates the end of the first drying stage, as the initial concentration increases the falling rate stage starts earlier. However, it can be seen that the droplet diameter in case of soyabase suspension does not cease once the falling rate period begins. The soyabase or skim milk suspension does not form a rigid crust as in the case of sodium sulfate solution, rather, the small dispersed particles near the surface move closer to each other upon drying,the number of these particles increase as more water is evaporated at the

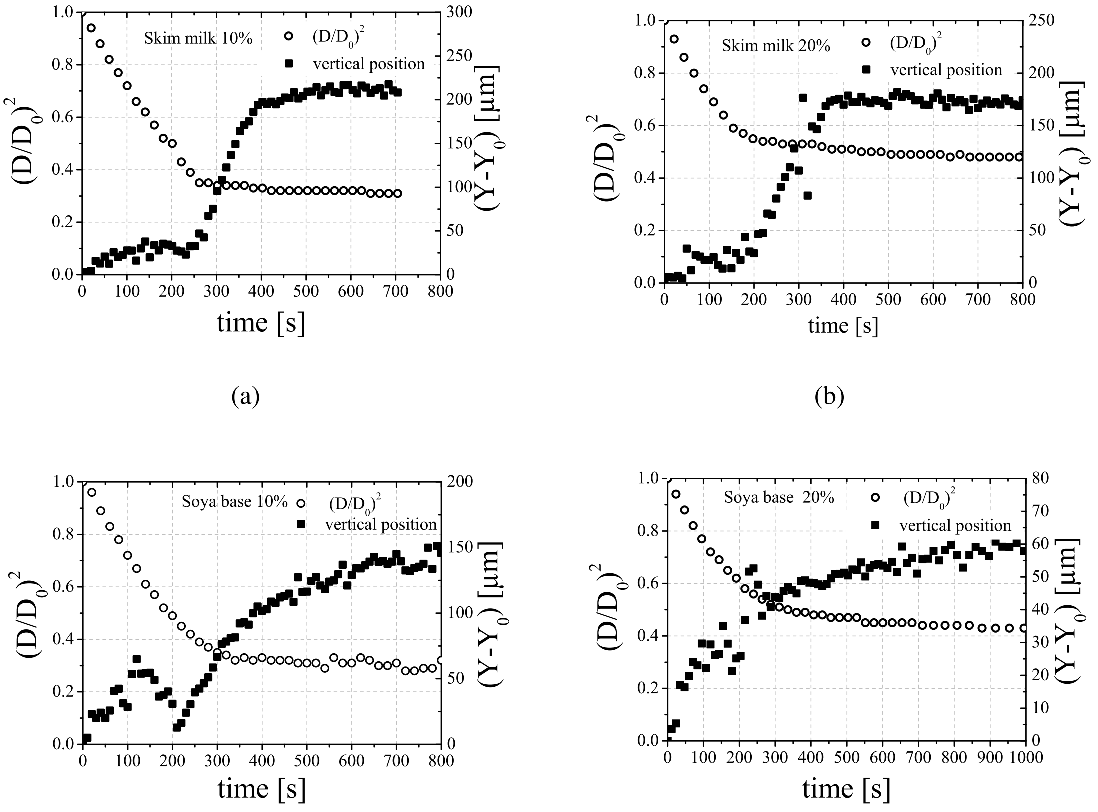

(a)

(b)

(c)

(d)

Figure 5.9: Temporal evolution of normalized droplet surface, the drying curves represent two different initial concentrations of a) skim milk $C_{s0} = 0.1$ and b)skim milk $C_{s0} = 0.2$. suspension. c) soya base $C_{s0} = 0.1$ and d)soya base $C_{s0} = 0.2$. Drying parameters are 28 °C and 12 % relative humidity, The vertical position of the droplet to the adjacent upper pressure node shows when the second drying stage begins.

surface. The moist now must diffuse between the particles, which leads to smaller evaporation rate. The droplet diameter decreases by 10% relative to the value at the end of the constant rate period designated by the rise of the droplet vertical position in the acoustic field.

Figure 5.9 shows the drying curves for skim milk and soyabase powders. Two experimental data ($C_{s0} = 0.1$ and $C_{s0} = 0.2$) are displayed, the ordinate which represents the Normalized droplet surface . The normalization is applied based on the initial diameter. The D^2-law is valid at the initial stage of drying i.e. constant rate period. The solid content in this stage is still small enough to influence the evaporation of the water dramatically as in the falling rate period; however, the evaporation rate in the first drying period is still lower comparing to an evaporation of pure liquid droplet at the same operational parameters.

The acoustic field will act on the droplet forcing it to be oblate, a series of shadow pictures are depicted in fig. 5.10 at different time steps. These pictures show that droplet shape deviate from a spherical shape. The shape of the droplet depends on the SPL value applied during the drying process. The droplet ends up with a disc-shape particle.

The internal structure of skim milk particle of 30% wt. initial concentration has been investigated under a scanning electron microscope (SEM), the droplet first is picked up from the levitator and glued into glass sheet. Then a layer of $10-30\mu m$ is wiped from the particle using a microtome knife, which is able to cut layers of thickness down to $10\mu m$, removing few layers enable us to uncover the internal structure of the particle.

SEM pictures of skim milk particles are depicted in fig. 5.11, the cross section shows clearly a full particle resulted from the drying process. While the liquid evaporates the

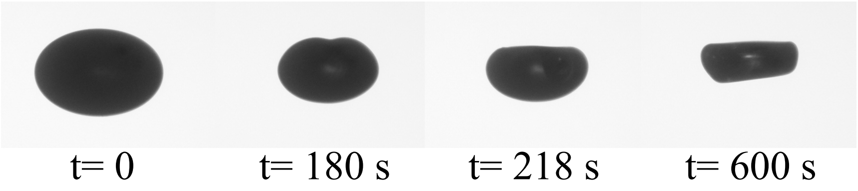

Figure 5.10: Images of skim milk droplet at 20% initial concentration. Images are captured at different time steps. Images show the shape evolution of the droplet upon drying. Ambient air temperature and relative humidity are 28 °Cand 10%, respectively.

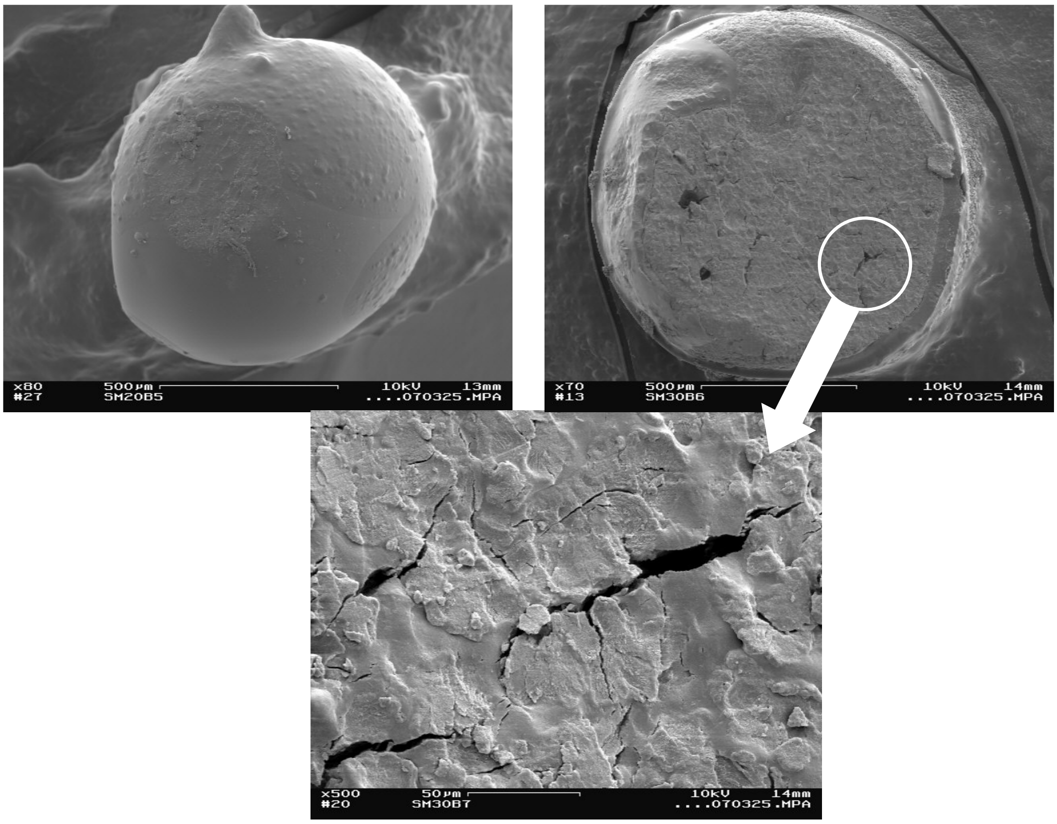

Figure 5.11: SEM images of skim milk particle 30% initial solid concentration, pictures have a magnification factor of 80×, 70× and 500×, respectively, Image (b) shows internal macrostructure of droplet, (c) enlarged view of the internal cracks.

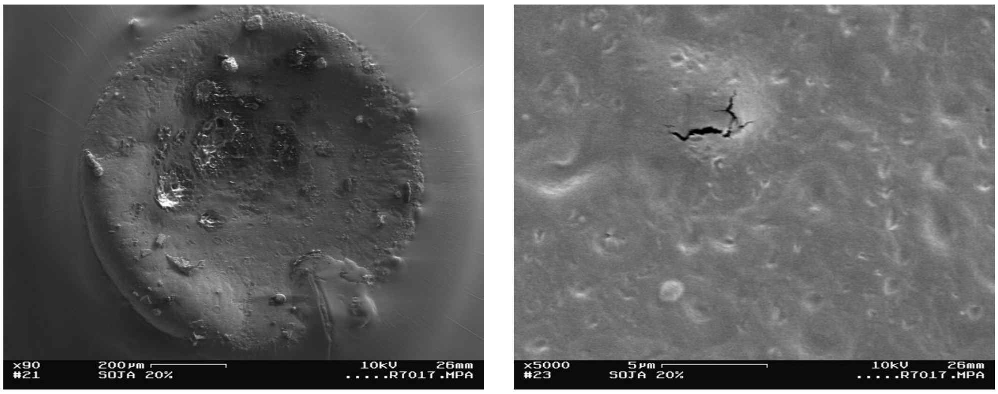

Figure 5.12: SEM images of soyabase particle of 20% initial concentration, outer surface with a magnification factor of 90× and 5000×, respectively, pictures(b) shows the a crack on the particle surface that occurred as a result of higher vapor pressure inside the droplet during the drying process.

small solid particles move inward the droplet center to form a denser and packed grain. Internal cracks shows that the moisture may follow preferred paths to move outward into the droplet surface. In fig. 5.12 SEM images of soyabase suspension of 20% initial solid concentration shows the morphology of a dried particle. It can be observed that the cracks on the surface that result from inflation, at a certain point when the equilibrium vapor pressure inside the droplet becomes larger the shell will burst, the vapor leaks through the clefts.

5.4 SPL Calibration

The comparison between modeling and experiment of drying requires the knowledge of the sound pressure level (*SPL*) Yarin et al. (1998). In case of pure liquid droplet the *SPL* resulting from the acoustic force can be calculated if the surface tension, density and shape of the droplet are known, The procedure is presented by Yarin et al. (1998). Those physical properties of the liquid does not change, therefore *SPL* can be determined; however, for an evaporating multiphase droplet, it exhibits a change in composition, this results in change of the surface tension and other physical properties also, the YPT method can't be used directly.

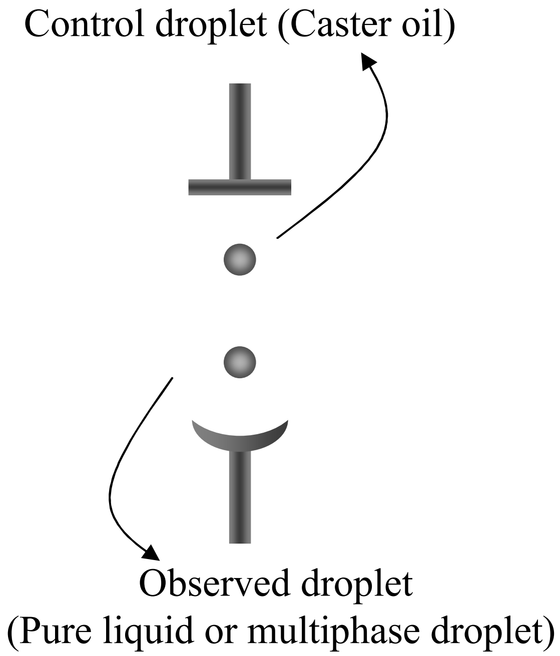

Figure 5.13: Sketch of two droplet levitaed in the acoustic field.

A method is suggested by Yarin et al. (2002a) to calculate the sound pressure level felt by binary liquid droplet during evaporation, *SPL* calibration of multiphase droplet rely on the idea that the interaction between two levitated pure liquid droplet can be correlated. As depicted in fig. 5.13, two droplets are levitated at the same time at two dif-

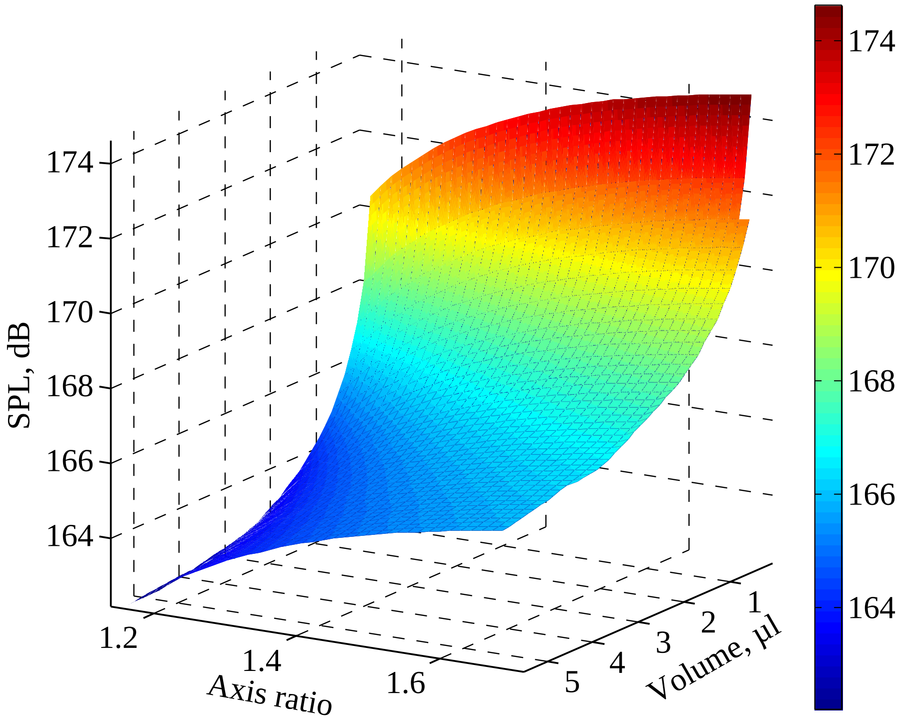

Figure 5.14: 3-D representation of *SPL* for water droplet, calculations carried out for different volume and droplet's shape.

ferent acoustic nodes, the upper droplet denoted as control droplet. This upper droplet is chosen to have a very small vapor pressure, the evaporation rate is small enough that no change in the droplet volume occurs. The lower droplet is the droplet under observation which may be a pure liquid droplet, multicompnent pure liquid droplet or even multiphase droplet. The control droplet is caster oil, which has a surface tension of 39 mN/m, other liquids used for calibration are listed in table 5.2, in each calibration experiment the following steps are taken into account:

- Control droplet must have always the same volume $1.5 \mu l$.
- The initial axis ratio (Horizontal diameter / vertival diameter), D_h/D_v of the control droplet is set to be 1.5, this is done by tuning the applied power to the piezocrystal.
- Volume of the observed droplet is kept the same in every experiment.
- The vertical distance between the reflector and the transducer is 1.2 cm (see Ch. 3).

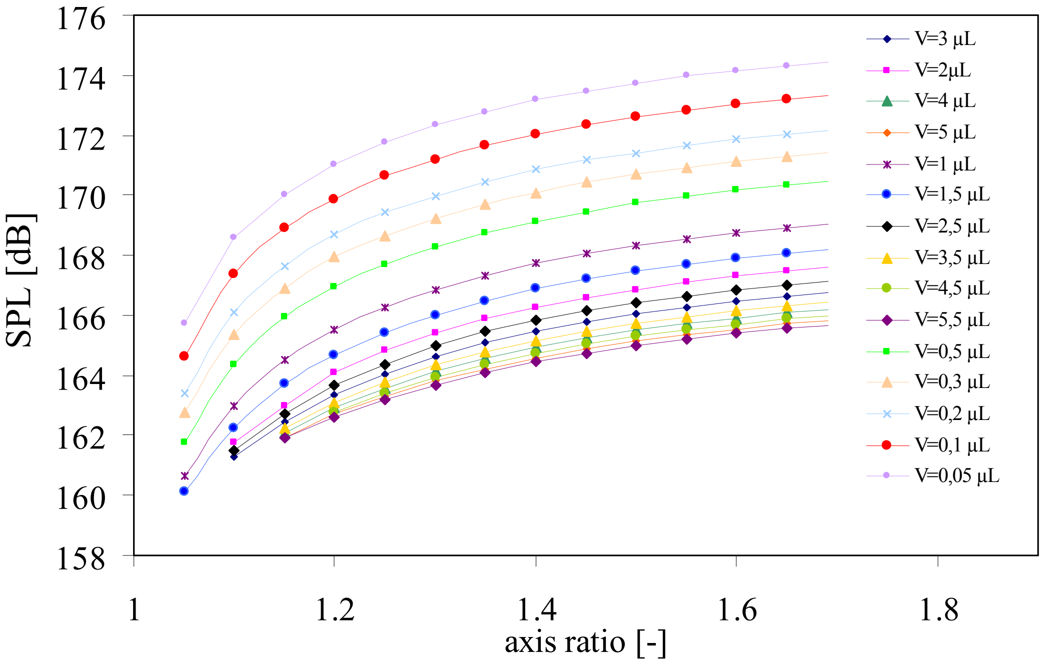

Figure 5.15: 2-D representation of calculated *SPL* values for water droplet at different volumes and droplet's shape.

Three different liquids were used, ethanol, methanol and iso-propanol. The volume change of caster oil droplet and droplet under observation is plotted versus time. The volume of the caster oil remains constant, as the observed droplet evaporates, it's volume decreases; hence, it scatters the acoustic field less and therefore the SPL value felt by the control droplet is increased, since the volume of the control droplet doesn't change. The force balance on the droplet surface increases causing the shape of the droplet to become more oblate and the value of the axis ratio (D_h/D_v) will increase with time. The droplet under observation continues to evaporate, the volume decreases and the shape of the droplet tends to reach an equilibrium value approaching a spherical shape of axis ratio equal 1.

5.4.1 Calibration curve

The method presented by (Yarin et al., 2002a) to calculate *SPL* for binary liquid mixtures will be adopted to estimate *SPL* values for multiphase droplets upon drying. The value of the *SPL* of the observed droplet is calculated for each sample (volume and axis ratio values) at every time step. This is also carried out for the control droplet.

Figure 5.14 displays numerical calculation of SPL values as a function of droplet vol-

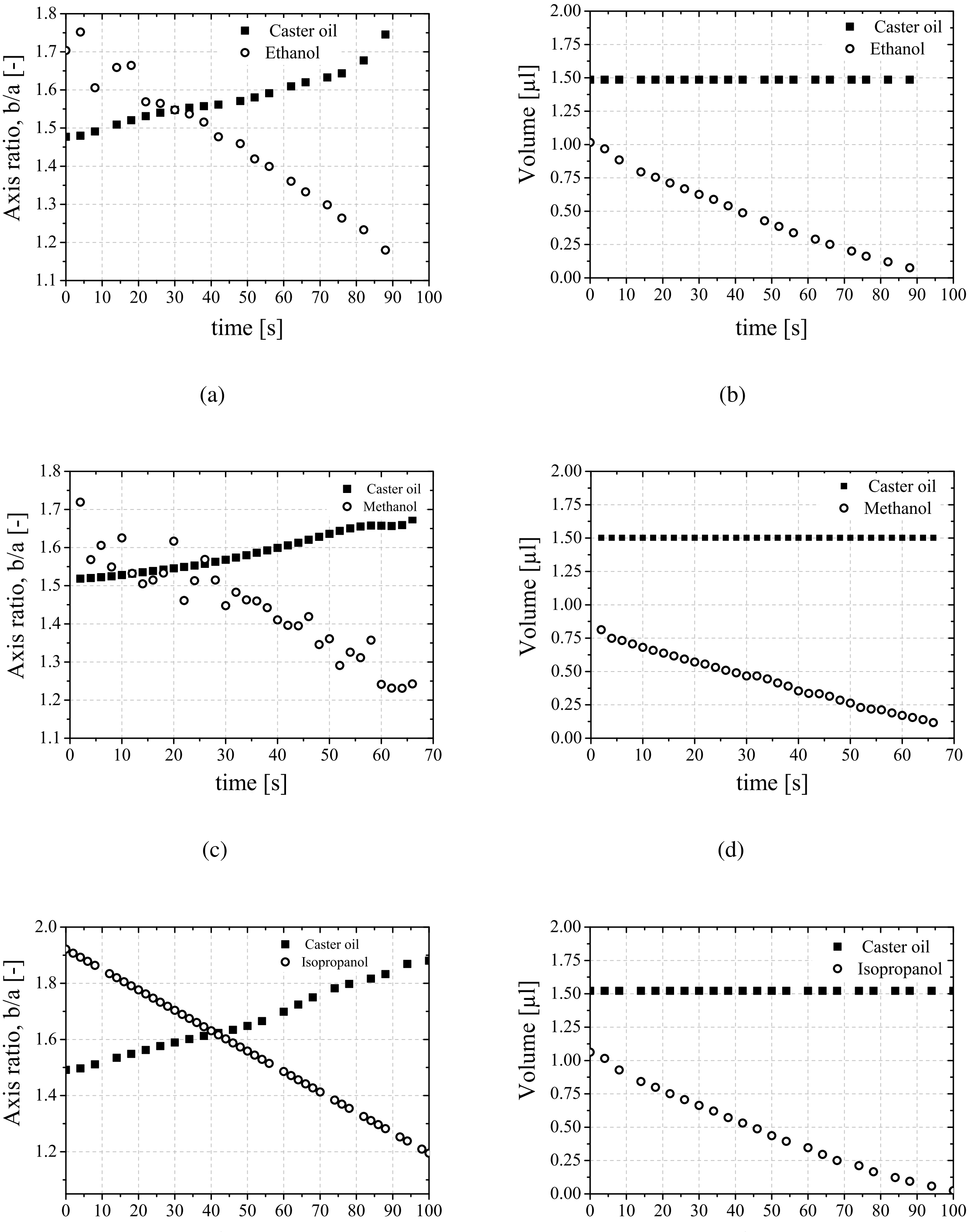

(a) (b)

(c) (d)

(e) (f)

Figure 5.16: Experimental results for ethanol, methanol and iso-propanol evaporation. The caster oil droplet is set as control droplet with an initial volume of 1.5 μl.

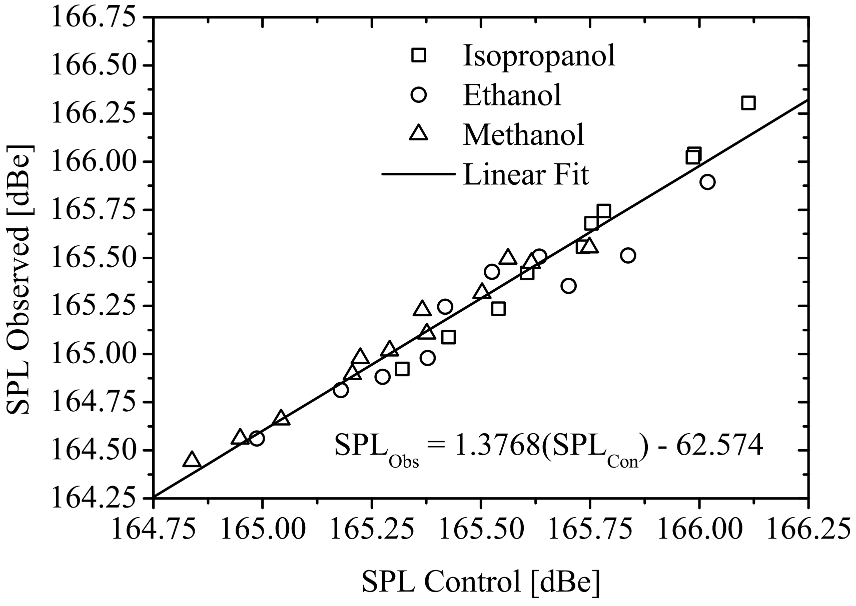

Figure 5.17: SPL calibration curve for pure liquids (ethanol, methanol and iso-propanol) and caster oil droplet as a control droplet, SPL values are obtained at different time steps.

ume and axis ratio, which are chosen to cover different situations of droplet shape and sizes that may result from experiments. It can be seen that SPL tends to increase as the droplet shape approaches a spherical shape for a constant volume. The SPL is higher for a small droplet volume; this is due to less scattering of the acoustic field by the smaller and spherical-like droplet.

A similar 2-D representation is depicted in fig. 5.15, both graphs are generated using the YPT algorithm (Yarin et al., 1999) and it can be calculated for each liquid.

Experimental results depicted in fig. 5.16 show the temporal evolution of axis ratio and volume of ethanol, methanol and iso-propanol droplets. Just after the droplet insertion in the acoustic filed the evaporation begins, the volume decreases and the droplet shape changes towards being spherical. In the case of caster oil the volume remains constant; however, its axis ratio increases, the droplet becoming more oblate. In this case the acoustic force applied to caster oil droplet become larger as the alcohol droplet evaporates.

A 2-D interpolation algorithm is implemented to calculate the SPL value of both caster oil droplets and other alcohol droplets during the course of evaporation. The calculated SPL are depicted in fig. 5.17; the values of SPL for the caster oil droplet versus SPL$_{observed}$ is shown. It can be seen that the points can be correlated to a linear fit that takes the form, $SPL_{obs} = 1.376 \cdot (SPL_{obs}) - 62.57$ with a correlation coefficient $R^{*} = 0.934$.

Table 5.2: Surface tension of studied liquids

Liquid	surface tension [mN/m]
Caster oil	39.0
Methanol	22.0
Iso-propanol	23.0
Ethanol	22.3
Water	72.0

5.4.2 SPL estimation for multiphase droplet

SPL estimation of multiphase droplets (sodium sulfate, skim milk and soyabase) were carried out applying the same procedure presented previously for the alcohol droplets. The conditions were kept as before e.g. caster oil control droplet initial volume and axis ratio are 1.5, vertical distance between reflector and transducer and the configuration of the observed and control droplet.

As depicted in figures 5.18-5.21. The temporal evolution of the axis ratio for both droplets is shown. Different materials and initial concentrations were investigated.

The sound pressure level of the observed droplet was estimated. First, the SPL values of the control droplet is calculated. Each pair (volume and axis ratio) from the experiments is used to calculate numerically the corresponding SPL. The SPL value for the observed droplet is estimated by applying the correlation found in fig. 5.17. It can be seen that as the multiphase droplet evaporates, the volume decreases and the scattered acoustic field becomes less. This is reflected by the caster oil droplet; the axis ratio increases, the droplet takes an oblate shape. The method presented for SPL accounts for the shape and size change to estimate the corresponding SPL value, it neglects the surface tension or any other influence.

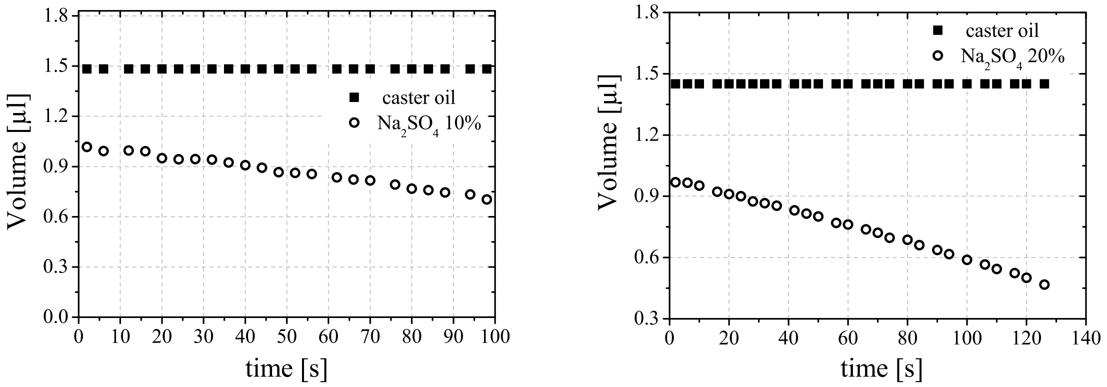

(a) Na_2SO_4 10%

(b) Na_2SO_4 20%

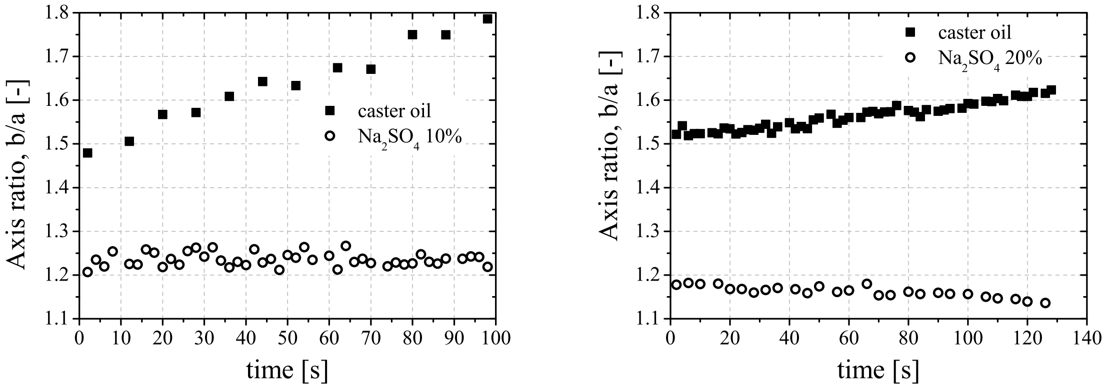

(c) Na_2SO_4 10%

(d) Na_2SO_4 20%

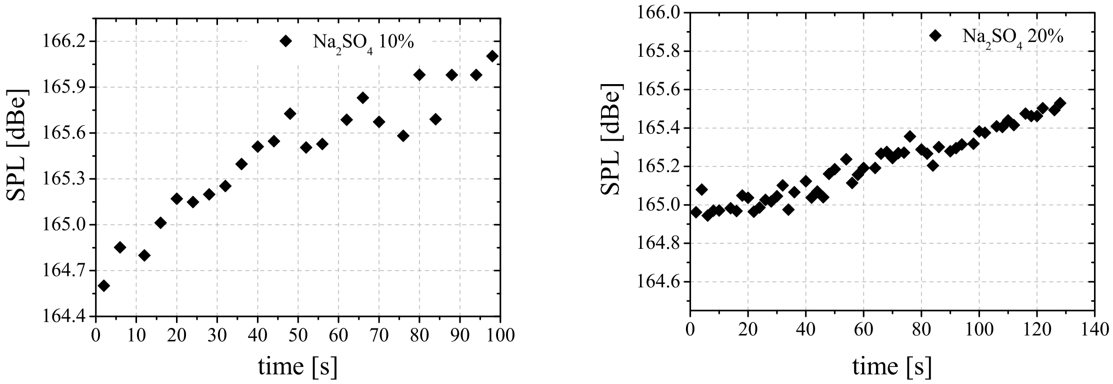

(e) Na_2SO_4 10%

(f) Na_2SO_4 20%

Figure 5.18: Calculated SPL for an aqueous droplet of Na_2SO_4 at initial solid concentration of 10% and 20% mass fraction, respectively, caster oil droplet is set as a control droplet with an initial volume of 1.5 μl.

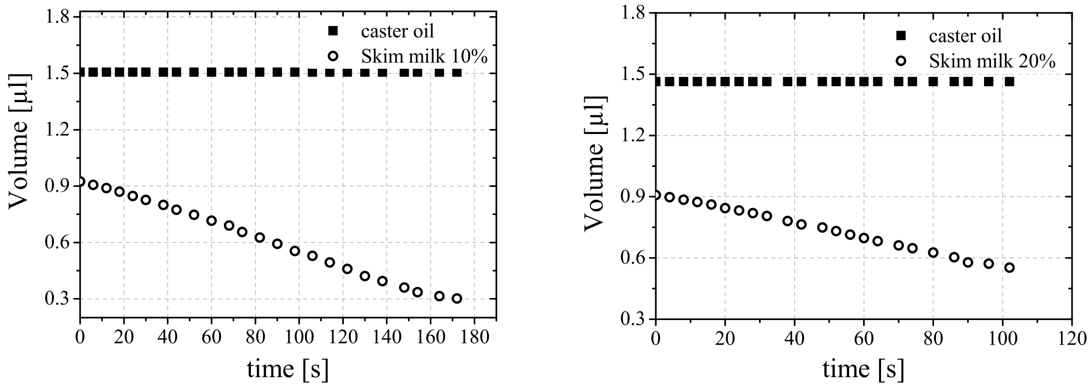

(a) Skim milk 10%

(b) Skim milk 20%

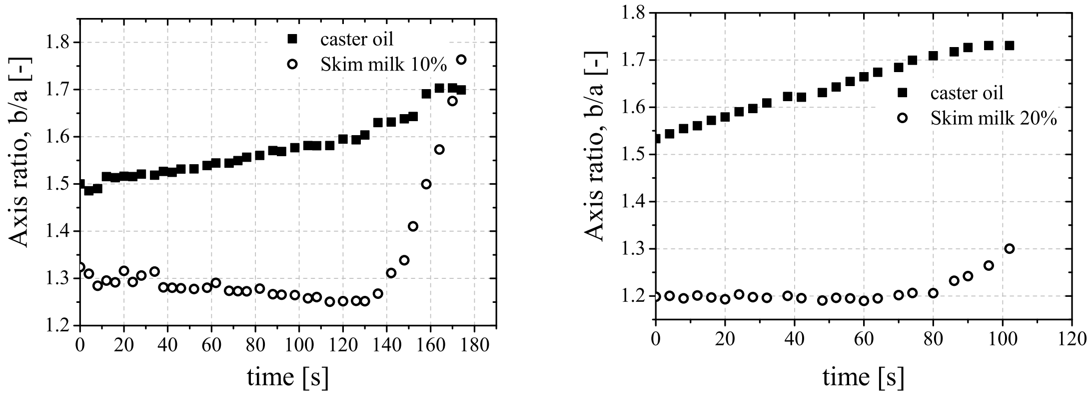

(c) Skim milk 10%

(d) Skim milk 20%

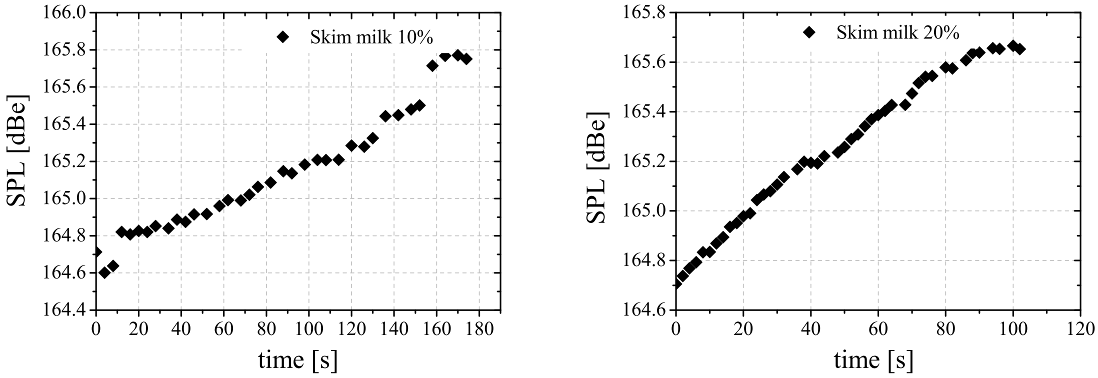

(e) Skim milk 10%

(f) Skim milk 20%

Figure 5.19: Calculated SPL for suspension of skim milk at initial solid concentration of 10% and 20% mass fraction, respectively, caster oil droplet is set as a control droplet with an initial volume of 1.5 μl.

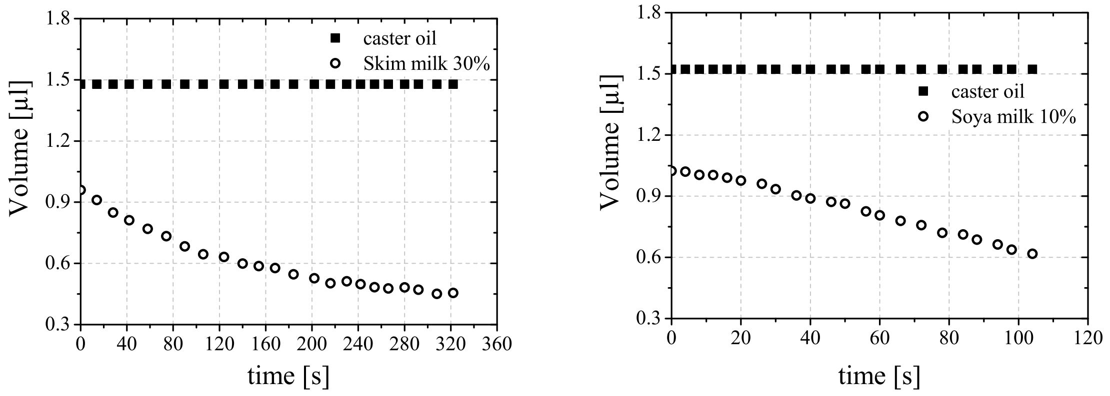

(a) Skim milk 30%

(b) Soyabase 10%

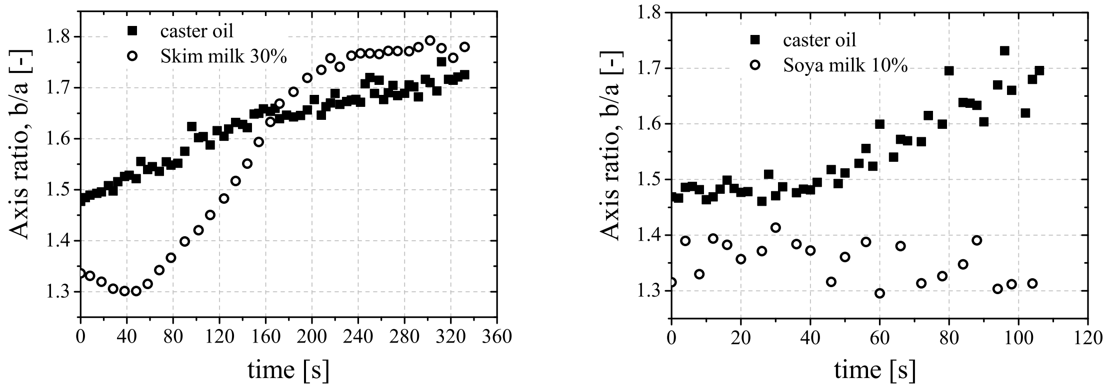

(c) Skim milk 30%

(d) Soyabase 10%

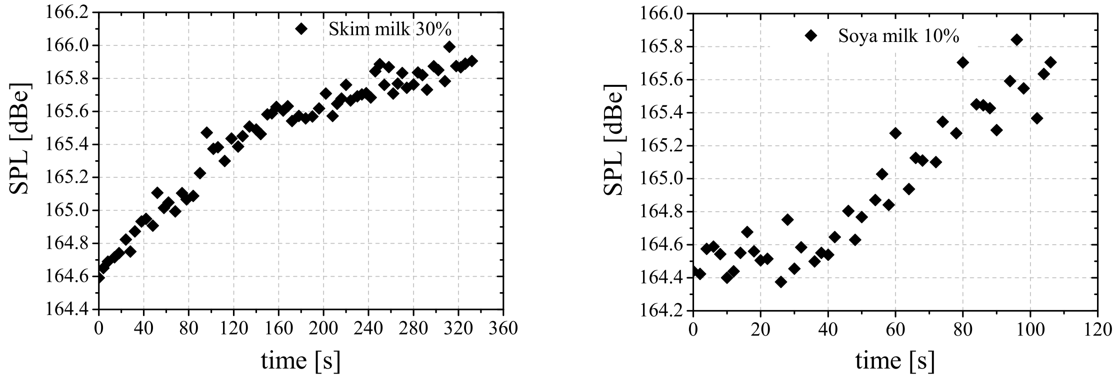

(e) Skim milk 30%

(f) Soyabase 10%

Figure 5.20: Calculated SPL for suspension of skim milk at initial solid concentration of 30% wt., and soyabase of 10 % wt. caster oil droplet is set as a control droplet with an initial volume of 1.5 μl.

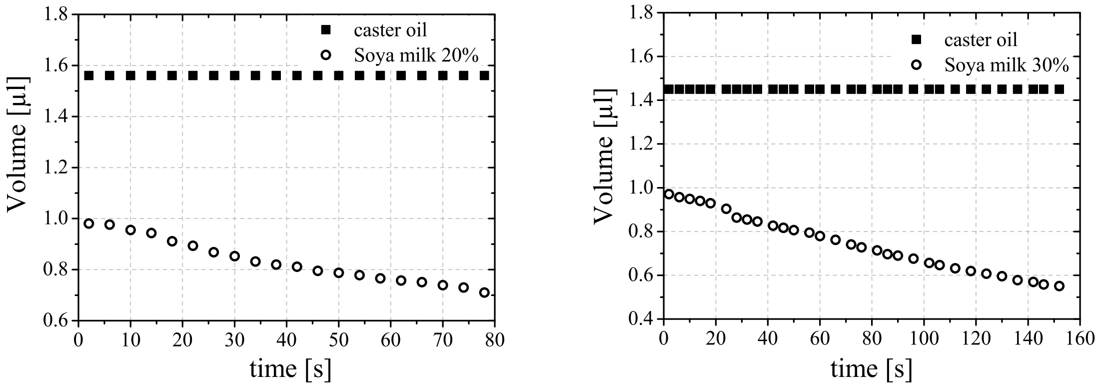

(a) Soyabase 20%

(b) Soyabase 30%

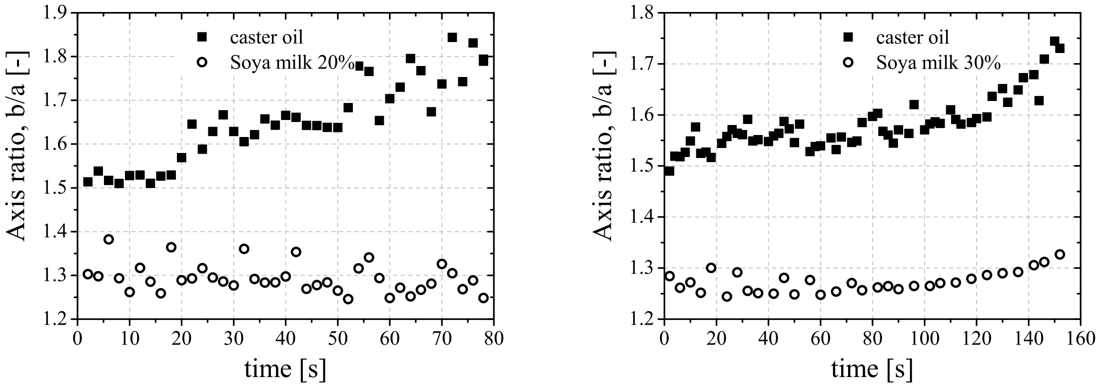

(c) Soyabase 20%

(d) Soyabase 30%

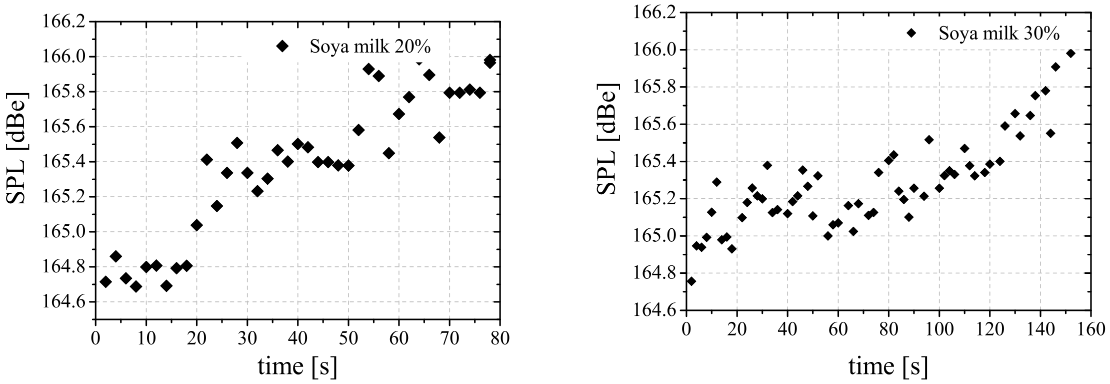

(e) Soyabase 20%

(f) Soyabase 30%

Figure 5.21: Calculated SPL for suspension of soyabase at initial solid concentrations of 20% and 30% wt. caster oil droplet is set as a control droplet with an initial volume of 1.5 μl.

Chapter 6

Drying of Single Droplets: Modelling

6.1 Perfect mixing model (PPM): Crust thickness estimation

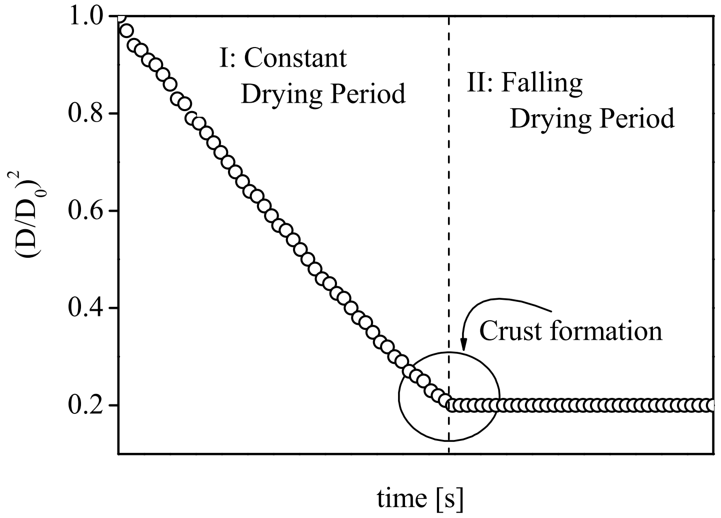

Figure 6.1: Drying curve of multiphase droplet represented by temporal evolution of the normalized surface area of the droplet. Once the crust is formed, the droplet keeps a constant volume.

The prediction of the drying of droplets depends on the type of material, dissolved solids such as salts, or suspensions such as milk or sugar like materials, i.e. Dextrine. Many parameters should be taken into account besides the process parameters (temperature, initial concentration or gas velocity), in particular the material properties i.e. the activity coefficient, mutual diffusion coefficient and thermal sensitivity.

A 1-D model to describe the drying of dissolved salts assuming perfect mixing, in which the solid concentration inside the droplet is homogeneous and increases as droplet evaporates, assumes the following:

- Uniform temperature distribution, temperature gradient is neglected.
- Mass and heat transfer parameters are assumed to be valid, in the case of inner acoustic boundary layer, Sh and Nu number proposed by Yarin et al. will be implemented. Other wise, for forced convection, Sh and Nu numbers from Ranz and Marshall are used.
- An equilibrium is assumed to exist between the vapor and the surrounding air i.e. evaporation is instantaneous.
- Uniform solid concentration is assumed though the droplet.
- The evaporation process is assumed to be spherically symmetric and the asymmetric convective effects are included implicitly.

The rate of change of droplet mass is equal to the rate of the vapor leaving the droplet surface evaporated from the droplet:

$$\frac{dm_v}{dt} = \rho_g \pi D \mathscr{D}_g Sh \cdot B_M \tag{6.1}$$

where, D is droplet diameter, $\mathscr{D}_g$ is the vapor air binary diffusion coefficient and B_M is Spalding mass transfer coefficient. Eqn. (6.1) predicts the mass loss of the droplet in the constant rate period, the presence of the dissolved solids will decrease the vapor pressure of the solution; hence decreasing the evaporation rate. Rault's Law is used to calculate the influence of the existing solute concentration:

$$P^v_{sol} = X_{liquid} \cdot P^v_{liq} \tag{6.2}$$

where, P^v_{liq} is the vapor pressure of the solvent and X_{liquid} is the molar fraction of solvent. Heat balance is calculated analogous to pure liquid evaporation:

$$Q_C = Q_{vap} + Q_L \tag{6.3}$$

where Q_C is the convective heat flux exchanged with the gaseous environment, Q_L is the heat flux entering into the liquid phase and Q_{vap} is the heat flux due to vaporization. The thermal properties of the droplet are calculated using the Ansatz:

$$\psi_{drop} = C_w \cdot \psi_{water} + (1 - C_w) \cdot \psi_{solids} \tag{6.4}$$

where ψ is the thermal property of water and solid material, i.e. heat capacity, heat conductivity and droplet density. ψ is function of temperature. Mass and heat transfer parameters are calculated using the Sh and Nu defined by eqn. (4.42) or eqn. (4.44). As depicted in fig. 6.2, the drying of an aqueous solution of Na_2SO_4 (initial solid mass fraction is 20%) is calculated at ambient gas temperature of 25 °C. The normalized surface is plotted versus time, the drying of multiphase droplet still follow the well known D^2-law. The temperature of the droplet during the evaporation falls down to the wet bulb temperature, here most of the heat delivered to the droplet from the gas phase is devoted to evaporating the water. It can be seen that the drying of pure liquid droplet is faster, this is due to the presence of the solids inside the multiphase droplet which hinder the evaporation.

Criterion to determine the end of the constant rate period

The loss of the water from the droplet bring the drying curve towards the end of the constant rate period, this can be easily seen in the sharp deflection point in fig.5.3 or fig. 6.1. Once the falling period starts, it's accompanied by constant volume evaporation. However, different criteria may describe how the droplet moves into the falling rate period. Basically the type of the droplet i.e. solution or suspension must be addressed. Kastner et al. (2001) proposed a model to describe the drying of a glass beads suspension which has small diameter aprox. $12\mu m$.

As the drying process goes on, the concentration of the solids on the surface increases and at later stages, due to the capillary mechanisms in the pores, the surface wetness can no longer be maintained (Masters, 1991). Handscomb et al. (2008) assumed that a shell is formed once the particle volume fraction becomes larger than a critical predefined value. This point corresponds to the state where the particles can no longer move

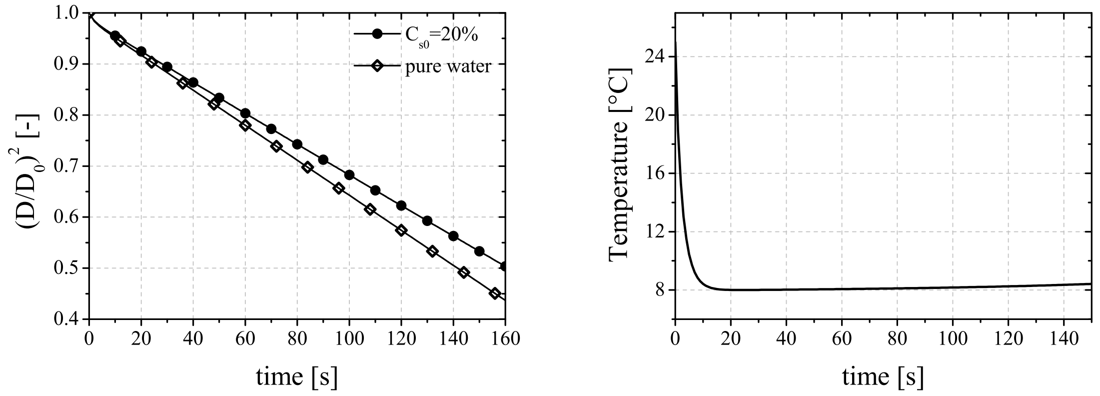

(a) D^2 law

(b) Drying at wet bulb temperature

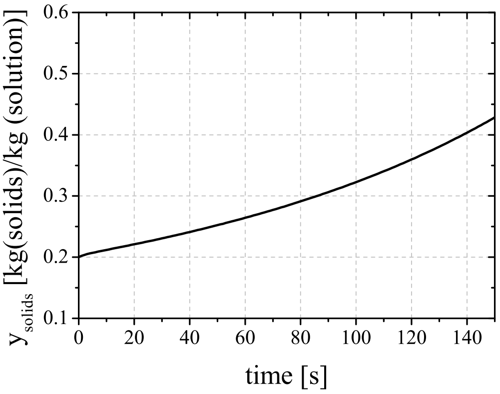

(c) Average concentration of solids

Figure 6.2: Drying of multiphase droplet of water and Na_2SO_4, initial solid content is wt. 20%, T_{gas} = 25 °C, the drying curve is calculated in the constant rate period.

toward the droplet center.

In materials like coffee extract or milk the transition from constant rate period to falling rate period seems to be difficult to be determined. The shell will form also if the droplet reaches it critical moisture content (Cheong et al., 1986, Mujumdar, 2006). For a droplet containing dissolved solids, the solute concentration increases, until it reaches the saturation point (Nesic and Vodnik, 1991). The crust will build up as long as a stable and rigid layer from the solids forms at the surface (Ford, 1996).

As the shell start to grow it adds a new resistance to the vapor diffusion into the existing mass transfer resistance in the diffusion boundary layer surrounding the particle. In order to incorporate these resistances into eqn. (6.1), K_g which is the mass transfer

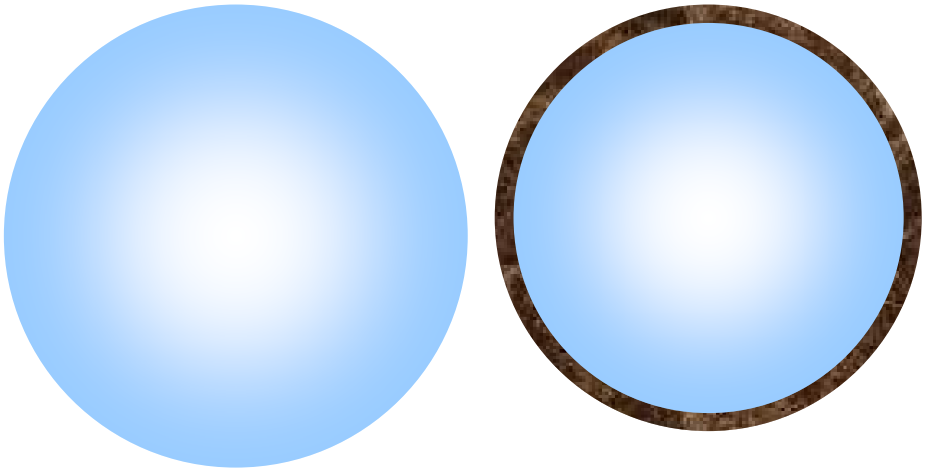

(a) Constant rate period (b) Falling rate period

Figure 6.3: Sketch of a) droplet in the constant rate period b) droplet surrounded by the shell right after the beginning of the falling rate period.

coefficient in the gas phase, is defined as (Incropera and Dewitt, 1996):

$$K_g = \frac{D}{Sh \cdot \mathscr{D}_g} \tag{6.5}$$

and the mass transfer coefficient due to crust resistance is defined as (Audu and Jeffreys, 1975):

$$K_{crust} = \frac{\delta}{\mathscr{D}_{crust}} \tag{6.6}$$

where δ is the crust thickness, $\mathscr{D}_{crust}$ is the effective diffusion coefficient in the crust, typically determined from the experiments. $\mathscr{D}_{crust}$ is also a function of the crust porosity and tortuosity of the porous crust. The effective diffusion coefficient is related to the vapor diffusion coefficient, (Audu and Jeffreys, 1975):

$$\mathscr{D}_{crust} = \mathscr{D}_g \cdot \varepsilon^{1.5} \tag{6.7}$$

or it's defined as a function of the porosity and the tortuosity (Cussler, 1997) :

$$\mathscr{D}_{crust} = \frac{\mathscr{D}_g \cdot (1-\varepsilon)}{\tau} \tag{6.8}$$

where τ is the tortuosity, which relates the actual distance the vapor must diffuse

through to a linear distance between the edges of the crust.
The overall vapor transfer resistance is then defined as:

$$K_{gc} = K_g + K_{crust} \tag{6.9}$$

The new mass transfer resistance is substituted into eqn. (6.1):

$$\frac{dm_v}{dt} = \rho_g \pi D_{drop}^2 \cdot \frac{B_M}{K_{gc}} \tag{6.10}$$

In the absence of the crust $\delta = 0$, the second term of the right-hand side of eqn. (6.9) cancel out and eqn. (6.10) is reduced to eqn. (6.1).

The crust thickness is calculated assuming that the evaporated water will be compensated by solid precipitation in the crust and the crust stays dry. The total mass of the solids is expressed as (Nesic and Vodnik, 1991):

$$\begin{aligned} m_s &= m_{s,core} + m_{s,crust} \\ &= \frac{\pi}{6}\rho_{core} \cdot y_s (D_{core})^3 + m_t - \frac{\pi}{6}\rho_{core} \cdot (D_{core})^3 \end{aligned} \tag{6.11}$$

Rearranging eqn. (6.11) and substituting $D_{core} = D - 2\delta$:

$$m_t - m_s = -\frac{\pi}{6}\rho_{core} \cdot y_s (D - 2\delta)^3 + \frac{\pi}{6}\rho_{core} \cdot (D - 2\delta)^3 \tag{6.12}$$

Equation (6.12) is divided by $m_{sat} - m_s$:

$$\frac{m_t - m_s}{m_{sat} - m_s} = \frac{-\frac{\pi}{6}\rho_{core} \cdot y_s (D - 2\delta)^3 + \frac{\pi}{6}\rho_{core} \cdot (D - 2\delta)^3}{m_{sat} - m_s} \tag{6.13}$$

where m_{sat} is the mass of the droplet just before the crust formation begins, the term $(m_{sat} - m_s)$ represents the mass of the water in the droplet. Then eqn. (6.13) becomes:

$$\frac{m_t - m_s}{m_{sat} - m_s} = \frac{-\frac{\pi}{6}\rho_{core} \cdot y_s (D - 2\delta)^3 + \frac{\pi}{6}\rho_{core} \cdot (D - 2\delta)^3}{\frac{\pi}{6}\rho_{core} \cdot y_w \cdot D^3} \tag{6.14}$$

with $y_s + y_w = 1$, eqn. (6.14) is solved for δ :

$$\delta = \frac{D}{2} \cdot \left(1 - \left(\frac{m_t - m_s}{m_{sat} - m_s}\right)^{1/3}\right) \tag{6.15}$$

To account for porous crust formation, ε is defined as the average crust porosity, the crust volume is calculated as :

$$\begin{aligned} v_c &= \frac{\pi}{6} \cdot \left(D_p^3 - (D_p - 2 \cdot \delta)^3\right) \\ v_{c,porous} &= \frac{v_c}{1 - \varepsilon} \end{aligned} \tag{6.16}$$

where v_c is the volume of compact crust, D_p is the diameter of the particle after crust formation. solving eqn. (6.16) for δ_{porous}:

$$\delta_{porous} = \frac{D_p}{2} - \left(\frac{D_p^3}{8} - \frac{6}{8\pi} \cdot v_{c,porous}\right)^{1/3} \tag{6.17}$$

Crust thickness calculated using eqn. (6.17) are schematically shown in fig. 6.5 respectively; a porous shell thickness is larger than a compact shell with $\varepsilon = 0$.

In the model, an average porosity is assumed throughout the drying process. Eqn. (6.17) is calculated at each time step. Knowing the crust thickness enables us to calculate the diameter of the core. In this model the crust is assumed to be dry; that means the evaporation occurs at the core-crust interface and the vapor diffuses through pores.

Drying of multiphase droplets of sodium sulfate and water at 28 °C and 12% relative humidity are depicted in fig. 6.5. The constant rate period ends up at 170 s, the falling rate period then starts. This can be easily seen as the diameter of the droplet, which is monitored using a CCD camera, doesn't change throughout the falling rate period.

Assuming a crust porosity of 20%, which is typical in detergent products, the modeled crust thickness reaches approx. 60 μm. The modeling in the constant rate is in good agreement with the experiment results. The model is initiated with the same experimental parameters, an initial SPL of 164.25 is assumed. It can bee seen that just before

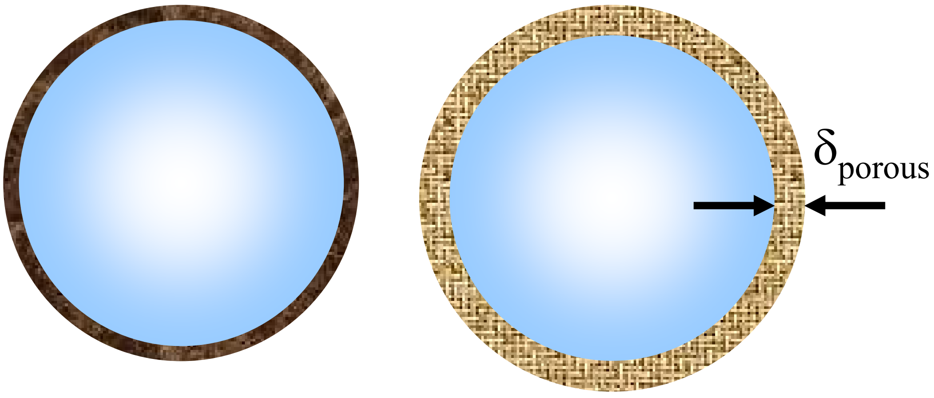

(a) Crust thickness, δ at $\varepsilon = 0$ (b) Crust thickness, δ_{porous} at ε_{ave}

Figure 6.4: Schematic of the crust thickness, a porous crust has larger thickness δ_{porous} comparing to crust thickness at $\varepsilon = 0$.

the crust formation the model deviates from the experiment, this can be explained by the existence of the salt, which hinder the evaporation of the water. However, Rault's law, which is being used to calculate the effective mole fraction at the surface, fails to predict the actual contribution of the sodium sulfate.

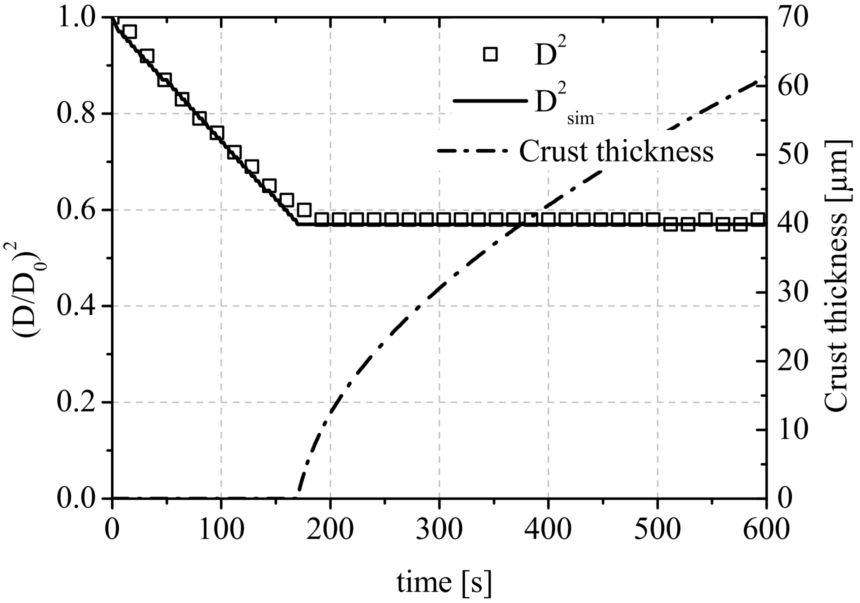

Figure 6.5: Drying of aqueous solution of Na_2SO_4 at 28 °C and 12% relative humidity, the initial droplet diameter is 1.0 mm, the crust thickness begins to increase in the falling rate period.

6.2 Diffusion mixing model (DMM)

Another approach to describe the drying behavior of the multiphase materials is to consider the internal distribution of the solids in radial direction. Different models exist in the literature to solve such systems (Kastner, 2001, Sano and Keey, 1982, Schiffter and Lee, 2007b).

The knowledge of the mutual diffusion coefficient is essential to run the model, mutual diffusion coefficients are typically a function of temperature and concentration of the water (Wijlhuizen et al., 1979). Estimation of the diffusion coefficient results from a comparison between the experimental results and the model; hence, experimental investigation of a single droplet drying in an acoustic levitator offers the ability to determine the diffusion coefficient by comparing the drying curve in order to determine the unknown parameters.

Diffusion Model formulation

In order to model the physical process in the droplet and to calculate the time dependent concentration distribution, a one dimensional, radial symmetric model is assumed, the droplet is assumed to be spherical. Sano and Keey (1982) accounted for bubble formation; here, we neglect this and no air bubble will form inside the droplet during the drying process. The diffusion equation and the continuity equation will be considered for the liquid component (Bird et al., 1960). Then the equation of the liquid concentration reads as (Sano and Keey, 1982):

$$\frac{\partial(\rho \cdot y_w)}{\partial t} + \underbrace{\frac{1}{r^2}\frac{\partial}{\partial r}\left(r^2\rho \cdot y_w V_r\right)}_{convection} = \underbrace{\frac{1}{r^2}\frac{\partial}{\partial r}\left(r^2\rho\mathscr{D}_{ws}\frac{\partial y_w}{\partial t}\right)}_{diffusion} \tag{6.18}$$

where, y_w is the mass fraction of the liquid component $y_w = \frac{\rho_w}{\rho}$, V_r is the radial bulk velocity of the of the liquid/solid mixture and ρ is the mixture concentration (kg/m^3). If the Rule of Amagat for a liquid solid mixture is applied (volume addivity) (Verdurmen et al., 2004):

$$\rho = \frac{\rho_s \hat{Y}}{y_w + \hat{Y}} \tag{6.19}$$

where $\hat{Y}$ is the density ratio and defined as:

$$\hat{Y} = \frac{\acute{\rho_w}}{\acute{\rho_s} - \acute{\rho_w}} \tag{6.20}$$

where $\acute{\rho_w}$, $\acute{\rho_s}$ are the density of the pure liquid and the solids, respectively. The continuity equation of mixture reads as:

$$\frac{\partial \rho}{\partial t} + \frac{1}{r^2}\frac{\partial}{\partial r}\left(r^2 \rho V_r\right) = 0 \tag{6.21}$$

applying partial derivative to RHS of eq. (6.18) yields:

$$\rho \frac{\partial y_w}{\partial t} + y_w \frac{\partial \rho}{\partial t} + \rho \cdot V_r \frac{\partial y_w}{\partial r} + \frac{y_w}{r^2}\frac{\partial}{\partial r}\left(r^2 \cdot \rho \cdot V_r\right) = \frac{1}{r^2}\frac{\partial}{\partial r}\left(r^2 \rho \mathscr{D}_{ws} \frac{\partial y_w}{\partial t}\right) \tag{6.22}$$

collecting similar terms :

$$\rho \frac{\partial y_w}{\partial t} + \rho \cdot V_r \frac{\partial y_w}{\partial r} + y_w \left[\frac{\partial \rho}{\partial t} + \frac{1}{r^2}\frac{\partial}{\partial r}\left(r^2 \cdot \rho \cdot V_r\right)\right] = \frac{1}{r^2}\frac{\partial}{\partial r}\left(r^2 \rho \mathscr{D}_{ws} \frac{\partial y_w}{\partial t}\right) \tag{6.23}$$

by substituting eqn. (6.21) into eqn. (6.23) we get:

$$\rho \frac{\partial y_w}{\partial t} + \rho \cdot V_r \frac{\partial y_w}{\partial r} = \frac{1}{r^2}\frac{\partial}{\partial r}\left(r^2 \rho \mathscr{D}_{ws} \frac{\partial y_w}{\partial t}\right) \tag{6.24}$$

combining eqn. (6.18) with eqn. (6.21) leads to the convective mass transport in the droplet, V_r:

$$V_r = \frac{\mathscr{D}_{ws}}{y_w + \hat{Y}} \frac{\partial y_w}{\partial r} \tag{6.25}$$

The Fickian transport equation of the time dependent concentration distribution is found by substituting eqns. (6.19),(6.20) and (6.25) into eqn. (6.24):

$$\frac{\partial y_w}{\partial t}+2\frac{\mathscr{D}_{ws}}{y_w+\hat{Y}}\frac{\partial y_w}{\partial r}=\frac{1}{r^2}\frac{\partial}{\partial r}\left(r^2\rho\mathscr{D}_{ws}\frac{\partial y_w}{\partial t}\right) \tag{6.26}$$

The initial conditions at time, t=0 is

$$y_w = y_{w_0} \quad \text{for r} \quad \in [0\ r_s] \tag{6.27}$$

Two boundary conditions are required to solve eqn. (6.26), at the center and at the surface of the droplet:

$$\begin{aligned}\frac{\partial y_w}{r} &= 0\\ \frac{\partial m}{\partial t} &= -\rho\cdot y_w\frac{\partial r}{\partial t}-\rho\frac{\hat{Y}}{y_w+\hat{Y}}\mathscr{D}_{ws}\frac{\partial y_w}{\partial r}\end{aligned} \tag{6.28}$$

where $\frac{\partial m}{\partial t}$ is the mass flow rate from the droplet surface eqn. (6.1). However, the presence of the solid components lead to a decrease of the vapor pressure of the liquid component at the droplet surface; thus, decreasing the evaporation rate.

In order to bridge the gap between phenomena occurring inside and outside the droplet, a new parameter is introduced to calculate $\dot{m}_v$. The activity coefficient a_w accounts for the influence of the solid component on the vapor pressure at the droplet surface, it depends on both concentration and the type of the solid material. a_w can be obtained from sorption isotherms (Gekas, 1992, Mujumdar, 2006). The mass fraction of the vapor at the droplet surface assuming thermodynamic equilibrium, is calculated using the following relation:

$$\begin{aligned}X_w &= a_w\cdot\frac{P_{sat}}{P^*_{liq}}\\ Y_{vap} &= \frac{X_w\cdot M_w}{X_w\cdot M_w+(1-X_w)\cdot M_{air}}\end{aligned} \tag{6.29}$$

Table 6.1: Estimated values of A, B and C used in eqn. (6.31)

Material	A	B	C
Soyabase	13.02	38.91	262.75
Skim milk	6.41	38.91	103.48

where, X_w is the mole fraction of the vapor. M_w, M_{air} are the molar mass of the water and the air, respectively. The correlation of activity given by Wijlhuizen et al. (1979) was employed:

$$a_w = \exp\left(-3.106 \times 10^{-3}\left(\frac{y_w}{1-y_w}\right)^{-2.18}\right) \tag{6.30}$$

The diffusion coefficient for milk and whey based products (Sano and Keey, 1982) depends on the concentration of the solvent, temperature and the activation energy. It normally take the general form:

$$\mathscr{D}_{ws} = \exp\left(-\frac{B + C \cdot y_w}{1 + A \cdot y_w}\right) \cdot \exp\left(-\frac{\Delta H}{R_G}\left[\frac{1}{T} - \frac{1}{303}\right]\right) \tag{6.31}$$

where, ΔH is the activation energy, and A, B and C are constants depends on the material and will be determined from the drying curve of the drying experiment. Experimental results of the drying kinetics of skim milk and soyabase suspensions are compared with model predictions described in §6.2, eqns. (6.26)-(6.28) are solved numerically to obtain the drying curve. The model implements a diffusion dependent concentration coefficient, eqn. (6.31), where A, B, C are adjustable parameters depending on the material. Figure 6.6 depicts the evolution of D^2 curves predicted by eqns. (6.26)-(6.28). Three different initial concentration were tested for both skim milk and soyabase.

The comparison between model and prediction and experimental results provides an estimation of the adjustable parameters A, B and C implemented in the diffusion coefficient. In table 6.1 the values of A, B and C for skim milk and soyabase powders are listed.

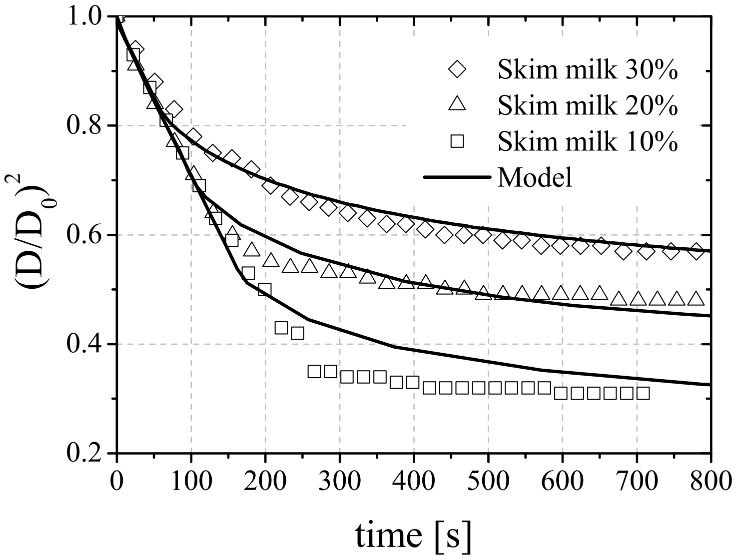

(a)

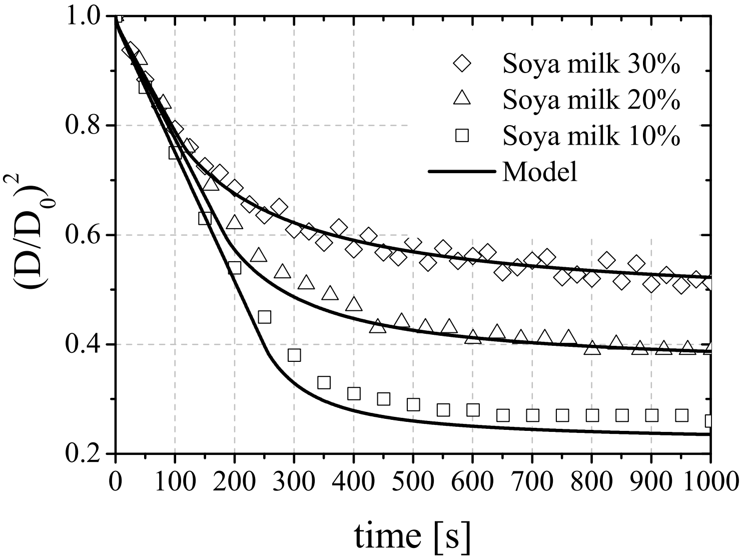

(b)

Figure 6.6: Drying rates of skim milk and soyabase suspensions. Drying parameters are 28 °C and 12 % relative humidity, the drying curves represent three different initial concentrations of the solid material 0.1, 0.2 and 0.3 wt%. Solid lines correspond to the predicted values by Sano and Keey Model.

6.3 Two-dimensional modelling

In chapter 5, the drying of multiphase droplets consisting of sodium sulfate solutions has been investigated experimentally. A 1-D model is presented to estimate the crust thickness. As mentioned previously, the drying process can be divided in principle into at least two drying steps i.e. the constant rate drying and falling rate drying. The first step is characterized by a volume decrease due to the evaporation of the solvent. The concentration of the solute increases as time proceeds, and when the concentration of the solute exceeds the critical concentration, crystallization starts at the droplet surface. However, in spray drying processes the heated air flows against the droplets with a relative velocity creating a stagnation point.

The formation of shell at the droplet surface can be significantly influenced by the flow of the drying gas. The evaporation rate is maximum at the stagnation point and it decreases around the surface as it reaches the rear stagnation point. That means the critical concentration of the solute occurs first at the front stagnation point (the crystallization start here first), and propagates towards the rear stagnation point.

Figure 6.7 shows the crystallization of an aqueous solution. A sequence of pictures were taken with a CCD camera and a long-distance microscope while the droplet was illuminated with front light. As long as there are no solids on the surface, the light passes through the droplet and once the crystals forms on the surface they reflect the light back, which is seen as a bright region in the pictures. The crust forms through crystallization, beginning at the south pole and progressing up around the equator of the drop. The evaporation of the moisture at the beginning of the drying is similar to the evaporation of pure liquid droplet of the same volume and follows the D^2-law. However, once the crust is formed, the liquid must pass through the pores of the crust and then by diffusion to the surrounding bulk gas, resulting in decrease of evaporation rate.

In the experiment shown in fig. 6.7, the air flow hits the droplet from the bottom, in the spray dryer the droplets trajectories follow different paths and the direction of these trajectories will determine the location of the stagnation point; hence, the point where the crystallization begins. As depicted in fig. 6.8 another configuration was tested. The

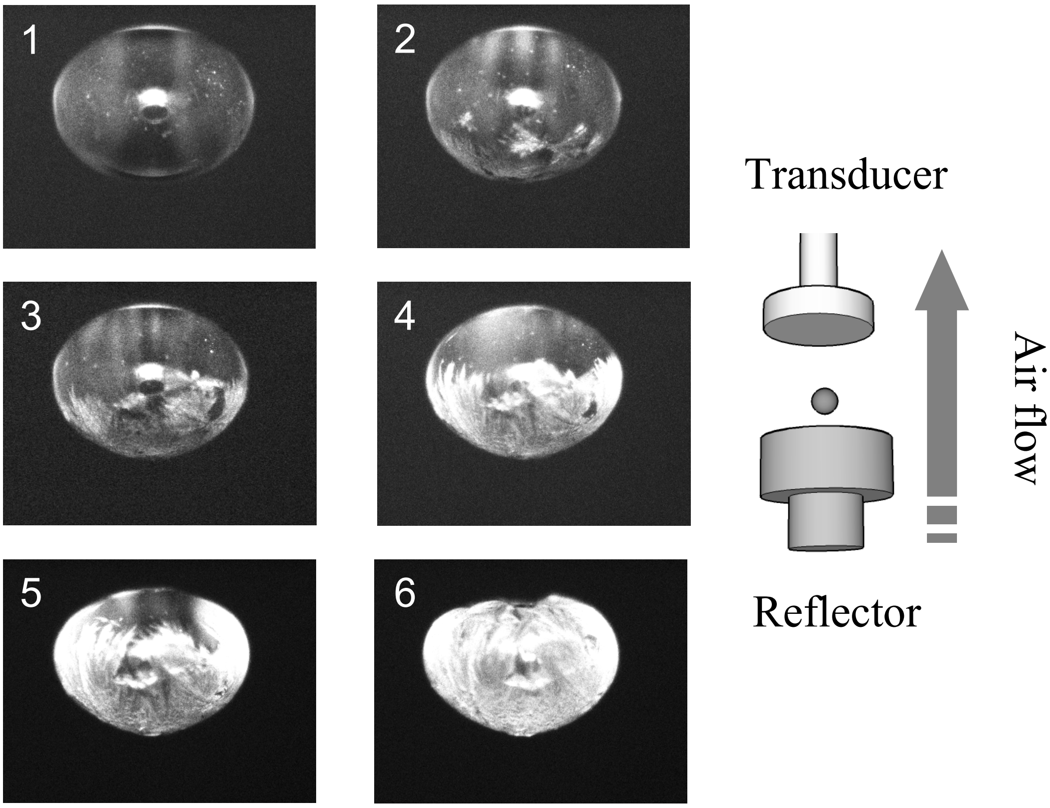

Figure 6.7: Crust formation at the end of constant rate period of a multiphase droplet of 20% initial mass concentration. Droplet volume 1.0 μl; the air flow comes from the bottom, a reflector of a central hole of diameter of 1.35 mm is used. Air flow at V_{air}=1.2 m/s.

air flows form the top and hits the droplet at the north pole. The pictures show clearly that the crystallization is initiated at the top of the droplet and then propagates towards the south pole.

Finally the levitator is mounted in horizontal orientation as shown in fig. 6.9, the levitaion of the droplet is achieved now by the radial acoustic force (F_r) in order to counteract the gravity force i.e. droplet weight. The radial acoustic force is smaller than the axial acoustic force. According to Lierke (1996b) the relation between both forces $F_{ac} : F_r$ is 5:1. As depicted in fig. 6.10 the droplet shape is more oblate than the droplet in fig. 6.7, which is due to the large driving voltage applied to the piezocrystal to increase the radial acoustic force. Moreover, the air flow coming from the reflector pushes the droplet near to the pressure node causing it to become more oblate.

an air flow of 0.4 l/min is induced from the reflector equipped with a nozzle having a diameter of 1.35 mm. The air velocity near the droplet surface is then 3.1 m/s. According to Yarin et al. (1999), this velocity is larger than the gas characteristic velocity, B_s. This air flow will blow out not only the outer acoustic streaming but it will also cause

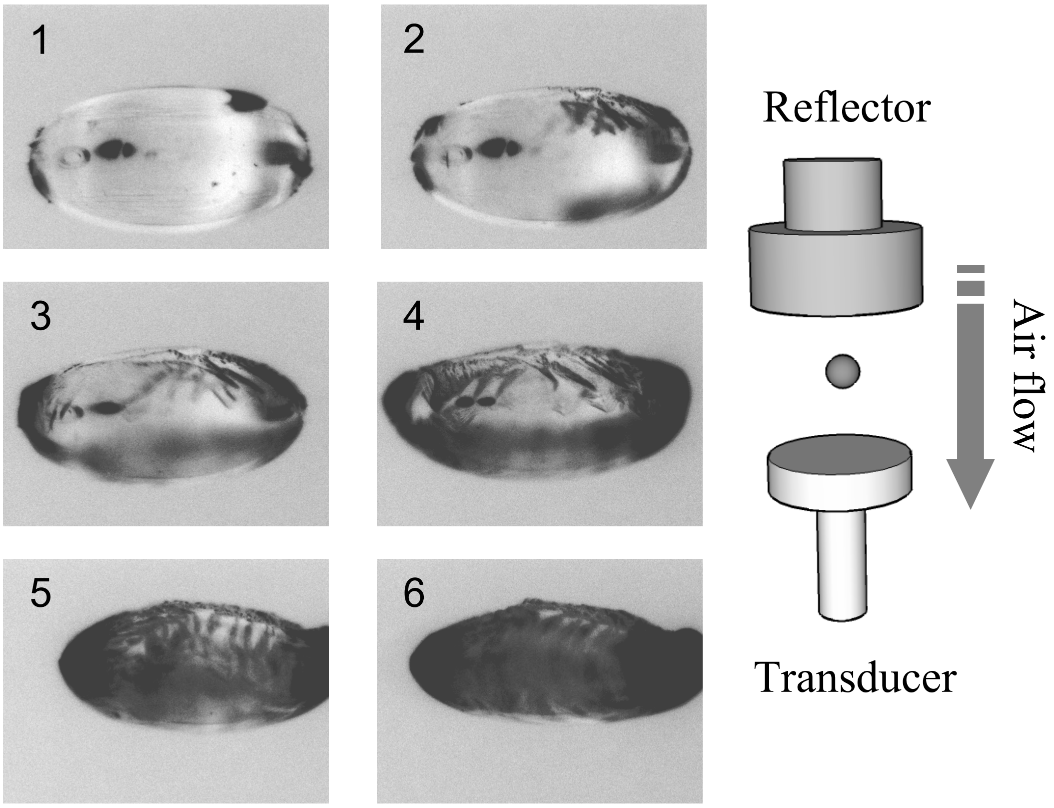

Figure 6.8: Crust formation at the end of constant rate period of a multiphase droplet of 20% initial mass concentration. Droplet volume 1.0 μl; the air flow comes from the top, a reflector of with central hole of diameter of 1.35 mm is used. Air flow at V_{air}=3.1 m/s.

the inner boundary layer to be destroyed, meaning that the evaporation is then driven by forced convection.

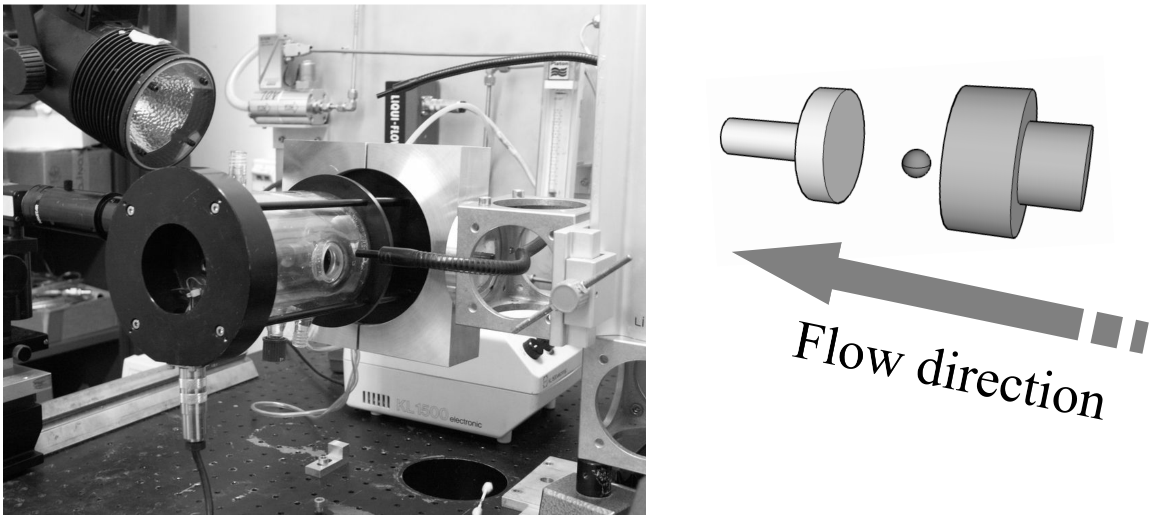

Figure 6.9: Experimental setup showing the levitator mounted in horizontal orientation, a strobe light is used to illuminate the droplet.

A mathematical model that describes the crystallization on the surface of the droplet

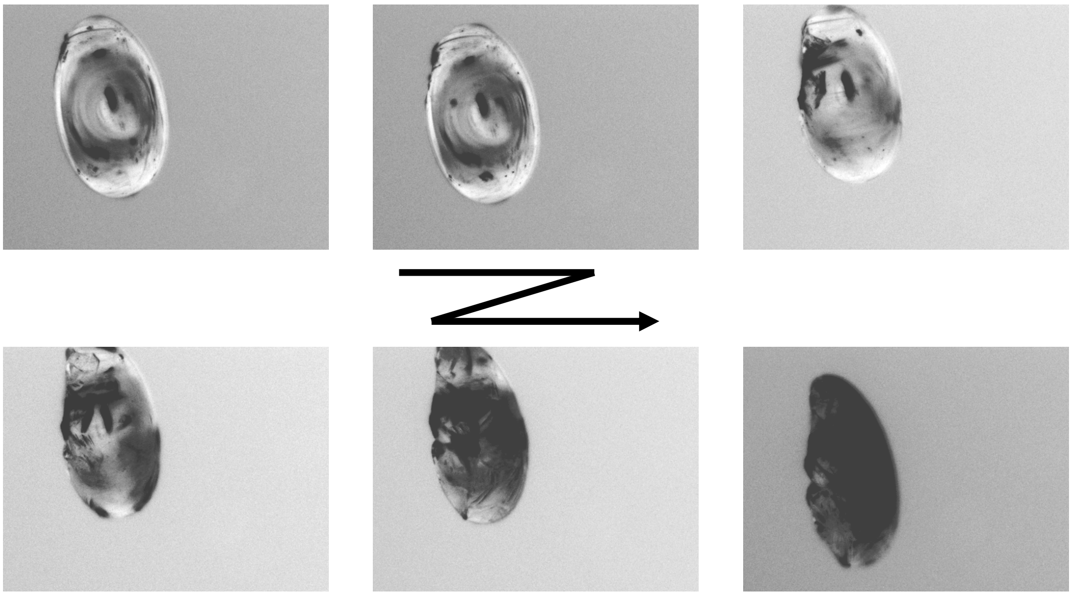

Figure 6.10: Crust formation at the end of constant rate period of a multiphase droplet of 20% initial mass concentration. Droplet volume 1.0 μl; the air flow comes from the side, a reflector of with central hole of diameter of 1.35 mm is used. An air flow at V_{air}=1.3 m/s.

as a function of the flow around the droplet is beneficial. In the following sections the development and the mathematical derivation of a 2-D drying model will be presented and the concentration of solid material will be calculated along the radius and over the droplet surface.

6.3.1 Model formulation

The drying model that can be used to describe the drying of a multiphase droplet is based on the continuity equation. The droplet consists of an evaporating component i.e. water and non-evaporation component i.e solids. Upon evaporation, the mass of the liquid decreases while the solids mass stays constant, which leads to a radial concentration gradient of both components. Here a 1-D dimensional model is assumed. The prediction of the concentration gradient along droplet radius and surface, can be formulated by a 2-D model. The main assumption of the model is that diffusion coefficient is uniform in both orientations. During the first drying period, the droplet has a spherical shape, heat conduction is the mechanism of heat transfer within the droplet; the droplet surface recedes as a result of the liquid component evaporation. The internal circulation will be neglected, air-water vapor mixture obeys the ideal gas law, and finally, evaporation occurs instantly so that a thermal and concentration equilibrium condition is established on droplet surface.

During evaporation, the droplet is assumed to be motionless and the stream of air flow of defined temperature, humidity and velocity surround the droplet.

At the beginning of the evaporation, the heating of the droplet is unsteady Fo<0.1; it last only for milliseconds during spray drying in industrial processes, therefore, the temperature profile will be calculated inside the droplet. Using spherical coordinates, the equation of energy conservation:

$$\begin{aligned}\frac{\partial T}{\partial t}+V_r\frac{\partial T}{\partial r}+\frac{V_\theta}{r}\frac{\partial T}{\partial \theta}=\frac{1}{r^2}\frac{\partial}{\partial r}\left(\alpha_d\cdot r^2\frac{\partial T}{\partial r}\right) &+ \frac{\alpha_d}{r^2\sin(\theta)}\frac{\partial}{\partial \theta}\left(\sin(\theta)\frac{\partial T}{\partial \theta}\right)\\ &+ \frac{\alpha_d}{r^2\sin\theta^2}\frac{\partial T}{\partial \phi}\end{aligned} \tag{6.32}$$

the corresponding Neumann boundary conditions at droplet surface and center:

$$\frac{\partial T}{\partial r}=0, \qquad \text{r=0} \tag{6.33}$$

$$4\pi r_s^2 K_d \frac{\partial T}{\partial r}\bigg|_{r=r_d}=4\pi r_s^2 h_g(T_g-T_d), \qquad \text{r=}r_s \tag{6.34}$$

Where α_d is the thermal diffusivity of the droplet and h_g is heat transfer coefficient. The continuity equation described by Bird et al. is used as the basis of this model.

The continuity equation for a binary liquid mixture reduces to the diffusion equation. In spherical polar coordinates this is :

$$\begin{aligned}\frac{\partial C_w}{\partial t}+V_r\frac{\partial C_w}{\partial r}+\frac{V_\theta}{r}\frac{\partial C_w}{\partial \theta}=\frac{1}{r^2}\frac{\partial}{\partial r}\left(\mathscr{D}_{ws}\cdot r^2\frac{\partial C_w}{\partial r}\right) &+ \frac{\mathscr{D}_{ws}}{r^2\sin(\theta)}\frac{\partial}{\partial \theta}\left(\sin(\theta)\frac{\partial C_w}{\partial \theta}\right)\\ &+ \frac{\mathscr{D}_{ws}}{r^2\sin\theta^2}\frac{\partial C_w}{\partial \phi}\end{aligned} \tag{6.35}$$

here C_w is mass fraction of the liquid component, $C_w+C_s=1$, $\mathscr{D}_{ws}$ is the binary diffusion coefficient which assumed to be spatially invariant, r,θ and ϕ are the radial, polar angle (rad) and azimuthal angle (rad) in spherical coordinates, respectively.

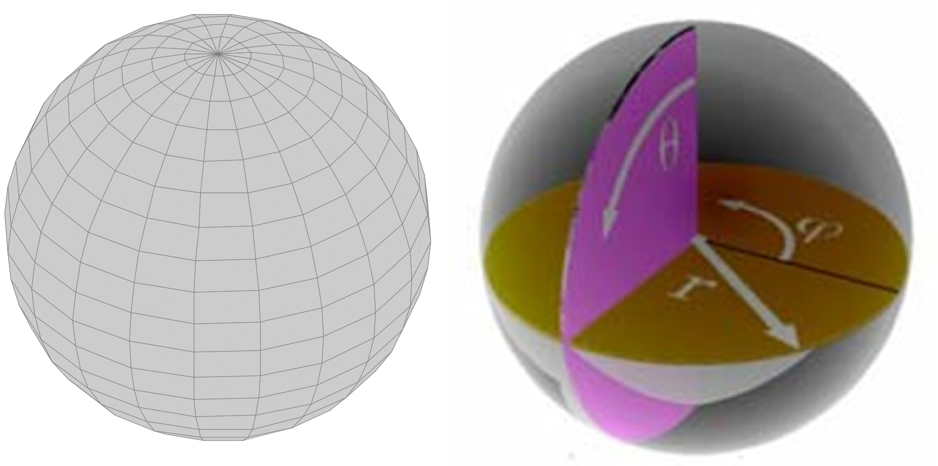

Figure 6.11: Spherical coordinate system used to solve the diffusion equation.

6.3.2 Coordinate system normalization

The evaporation of multiphase droplet is accompanied by a volume reduction and a change in the solids concentration inside the droplet and at its surface. The formation of the shell will add another difficulty as this creates a fixed outer diameter with core of moving interface. This results in a system of PDE with moving boundary conditions and, therefore, a normalization of the coordinate system in radial orientation should be implemented to solve the diffusion equation.

In order to track the moving front, the following coordinate transformation is applied to all equations:

- Dimensionless radial coordinate, ξ

$$\alpha = \frac{r_s(t)}{r_0} \tag{6.36}$$

$$\xi = \frac{r}{r_s(t)} \tag{6.37}$$

$$\frac{\partial}{\partial r} = \frac{1}{r_s}\frac{\partial}{\partial \xi} \tag{6.38}$$

where $r_s(t)$ is the droplet radius, for $0 < r < r_s$, the dimensionless coordinate $\xi \in [0:1]$

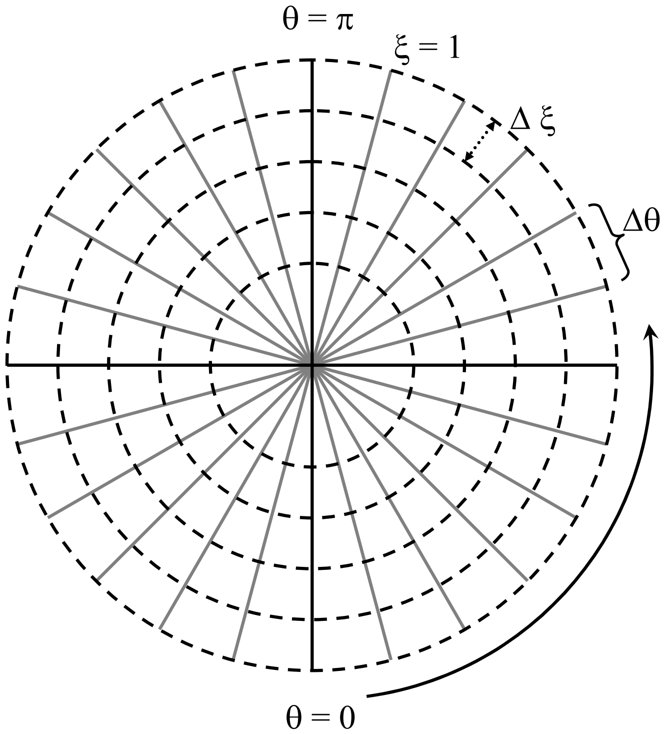

Figure 6.12: 2-D grid implemented to solve the diffusion equation, radial coordinate, $\xi \in [0,1]$ and $\Delta\xi$ step, the azimuthal coordinate θ start from $\theta = 0$ to $\theta = \pi$ with step of $\Delta\theta$.

- Dimensionless time, τ

$$\tau = t/t^* \tag{6.39}$$

where t^* is the total time needed to evaporate the liquid. For a function $\Phi = f(\xi(r_s(t)),t)$, when applying Landaus's transformation, (Crank, 1984), we have:

$$\left.\frac{\partial\Phi}{\partial t}\right|_r = \frac{\partial\Phi}{\partial\xi}\frac{\partial\xi}{\partial r_s}\frac{\partial r_s}{\partial t} + \left.\frac{\partial\Phi}{\partial t}\right|_\xi \tag{6.40}$$

the partial derivative $\frac{\partial\xi}{\partial r_s}$ with the help of eqn. (6.37) may rewritten as:

$$\frac{\partial\xi}{\partial r_s} = -\frac{r}{r_s^2} = -\frac{\xi}{r_s} \tag{6.41}$$

The time derivatives in ξ coordinate system are then related to those in r coordinate system by:

$$\left.\frac{\partial}{\partial t}\right|_r = \left.\frac{\partial}{\partial t}\right|_\xi - \frac{\xi}{r_s}\frac{\partial}{\partial\xi}\frac{\partial r_s}{\partial t} \tag{6.42}$$

when eqns. (6.37) and (6.42) are substituted into eqn. (6.35), we get:

$$\begin{aligned} \left.\frac{\partial C_w}{\partial t}\right|_{\xi} - \frac{\xi}{r_s}\frac{\partial C_w}{\partial \xi}\frac{\partial r_s}{\partial t} &= \frac{\mathscr{D}_{ws}}{r_s^2\xi^2}\frac{\partial}{\partial \xi}\left(\xi^2\frac{\partial C_w}{\partial \xi}\right) \\ &+ \frac{\mathscr{D}_{ws}}{r_s^2\xi^2}\left[\frac{1}{\sin(\theta)}\frac{\partial}{\partial \theta}\left(\sin(\theta)\frac{\partial C_w}{\partial \theta}\right) + \frac{1}{\sin\theta^2}\frac{\partial C_w}{\partial \phi}\right] \end{aligned} \tag{6.43}$$

Rearrange eqn. (6.43) and render $r_s(t),t$ by r_0 and t^*,the total time to evaporate the whole amount of the liquid eqn. (6.39), respectively yields:

$$\begin{aligned} \alpha^2\frac{\partial C_w}{\partial \tau} &= \frac{\xi}{2}\frac{t^*}{r_0^2}\frac{\mathrm{d}r_s^2}{\mathrm{d}t}\frac{\partial C_w}{\partial \xi} + \frac{\mathscr{D}_{ws}}{\xi^2}\frac{\partial}{\partial \xi}\left(\xi^2\frac{\partial C_w}{\partial \xi}\right) \\ &+ \frac{\mathscr{D}_{ws}\cdot t^*}{r_0^2\xi^2}\left[\frac{1}{\sin(\theta)}\frac{\partial}{\partial \theta}\left(\sin(\theta)\frac{\partial C_w}{\partial \theta}\right) + \frac{1}{\sin\theta^2}\frac{\partial C_w}{\partial \phi}\right] \end{aligned} \tag{6.44}$$

The concentration profile along ϕ coordinate is assumed to be uniform; hence the third term of RHS drops out:

$$\begin{aligned} \alpha^2\frac{\partial C_w}{\partial \tau} &= \frac{\xi}{2}\frac{t^*}{r_0^2}\frac{\mathrm{d}r_s^2}{\mathrm{d}t}\frac{\partial C_w}{\partial \xi} + \frac{\mathscr{D}_{ws}}{\xi^2}\frac{\partial}{\partial \xi}\left(\xi^2\frac{\partial C_w}{\partial \xi}\right) \\ &+ \frac{G_{ws}}{\xi^2}\left[\frac{1}{\sin(\theta)}\frac{\partial}{\partial \theta}\left(\sin(\theta)\frac{\partial C_w}{\partial \theta}\right)\right] \end{aligned} \tag{6.45}$$

where G_{ws} is the non-dimensional diffusion time introduced first by (Brenn, 2004):

$$G_{ws} = \frac{\mathscr{D}_{ws}\cdot t^*}{r_0^2} \tag{6.46}$$

6.3.3 Initial and boundary conditions

The solution of eqn. (6.45) which is a PDE of second order in two spatial coordinates requires an initial and two boundary conditions in each direction, namely r and θ. In order to calculate the concentration profiles of both components in dynamic or acoustic field, different boundary conditions will be used in each case to solve eqn. (6.45).

Initial conditions

The multiphase droplet is assumed to have a homogeneous concentration distribution of solid component inside the droplet, and the initial concentration c_{w0} at τ_0 is known. The initial condition of each coordinate system is given by:

$$C_w = C_{w0}, \quad \xi \in [0:1] \quad \text{at} \quad t = 0 \tag{6.47}$$

$$C_w = C_{w0}, \quad \theta \in [0:2\pi] \quad \text{at} \quad t = 0 \tag{6.48}$$

Boundary conditions

r-coordinate

The first boundary condition for the radial coordinate defined at droplet center arises from symmetry considerations:

$$\frac{\partial C_w}{\partial \xi} = 0, \quad \tau \in [0:1] \quad \text{at} \quad \xi = 0 \tag{6.49}$$

At droplet surface the mass balance of the evaporating component is given by:

$$\frac{\dot{m}}{4 \cdot \pi \cdot r_s(t)^2} = -\rho_d \mathscr{D}_{ws} \frac{\partial C_{wi}}{\partial r} + \rho_d \cdot C_{wi} \frac{\partial r_s}{\partial t} \tag{6.50}$$

rearrange eqn.(6.50) for $\frac{\partial C_w}{\partial r}$:

$$\frac{\partial C_w}{\partial r} = \frac{C_w}{\mathscr{D}_{ws}} \frac{\partial r_s}{\partial t} - \frac{\dot{m}_w}{4 \cdot \pi r_s(t)^2 \rho_d \mathscr{D}_{ws}} \tag{6.51}$$

In dimensionless form, the corresponding transformation of eqn. (6.51) reads for all times, t at $\xi = 1$:

$$\frac{\partial C_w}{\partial \xi} = r_s(t)^2 \frac{C_w}{\mathscr{D}_{ws}} \frac{\partial \xi}{\partial t} - \frac{\dot{m}_w \cdot r_s(t)}{4\pi \cdot r_s(t)^2 \rho_d \mathscr{D}_{ws}} \tag{6.52}$$

where $\dot{m}$ is the mass flux of the liquid component across droplet surface, ρ_d is the droplet density. Eqn. (6.52) will be solved pointwise on the droplet surface $\theta \in [0:\pi]$;

a simplified form is given by:

$$\frac{\partial C_w}{\partial \xi}(\theta) = C_w(R,\theta)\cdot A_t(\theta) - G_t(\theta) \tag{6.53}$$

where

$$A_t = \frac{r_s(t)^2}{\mathscr{D}_{ws}}\frac{\partial \xi}{\partial t} \quad \text{and} \quad G_t = \frac{\dot{m}_w(\theta) r_s(t)}{\mathscr{D}_{ws}} \tag{6.54}$$

The boundary condition in eqn. (6.52) can be rewritten for the solid component. In this case the second term of the RHS drops out and there is no mass flux of the solid component, $\dot{m}_s = 0$. The droplet density ρ_d is calculated at every time step assuming volume additivity (Sano and Keey, 1982):

$$\rho_d(r,\theta,t) = \frac{\rho_s \cdot \hat{Y}}{\hat{Y} + C_w(r,\theta,t)} \tag{6.55}$$

where $\hat{Y}$ is the density ratio and defined in eqn. (6.20), and ρ_s is the density of solids.

θ-coordinate

The concentration profile is solved over the θ domain, which starts from the front stagnation point ($\theta = 0$) to the rear stagnation point ($\theta = \pi$); the differential equation results form the symmetry condition at both points:

$$\frac{\partial C_w}{\partial \theta} = 0, \quad \theta = 0 \quad \text{for all times t} \tag{6.56}$$

$$\frac{\partial C_w}{\partial \theta} = 0, \quad \theta = \pi \quad \text{for all times t} \tag{6.57}$$

6.3.4 Transfer parameters

The boundary conditions depends on the species and thermal gradients at the droplet surface, deduced from the external flow computation by implementing an adequate mesh in the vicinity of the droplet. Indeed the droplet is considered as a mass flow inlet for the external flow, and the vapor flow rate corresponds also to a boundary condition. An iterative process must be consequently performed for the external flow to calculate the vapor flow rate profile. For a small droplet at low air velocity a laminar flow is

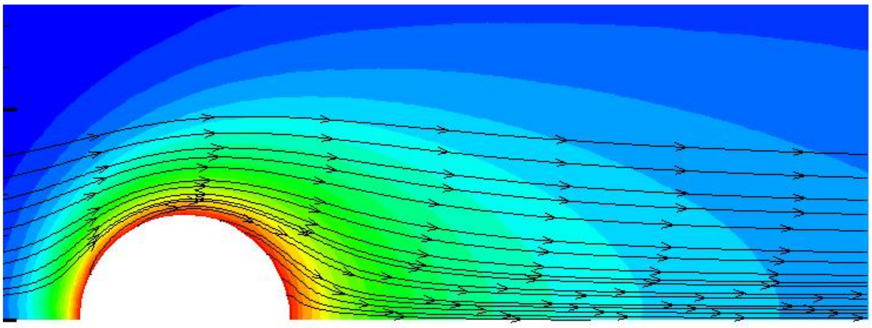

Figure 6.13: Flow past spherical droplet, flow direction from left to right.

established around the droplet. Fig. 6.13 shows the stream lines of such a flow.

The complete evaporation model implies an unsteady two-way coupling between the gas phase and the liquid phase assuming a quasi-steady evaporation. Nevertheless, after a short transient stage, the droplet reaches a uniform steady surface temperature, whereas the vapor flow rate and total heat flux depend mostly on the convection in the gas phase.

In the first approximation, computations are performed for different cases considering the droplet surface temperature as being uniform. As depicted in 6.15, three different cases are considered corresponding to different operational parameters, from the droplet lowest temperature at the end of the evaporation to its highest injection temperature.

These steady computations result in similar boundary conditions profiles (Frackowiak, 2007), which are converted into Nusselt and Sherwood number profiles. Here also Sh and Nu numbers present a maximum at the stagnation point on the leading edge, and decrease until the rear of the droplet on the trailing edge. Their minimal values are close to 2, due to the weak velocity in this area, reducing strongly the convection. Whereas their average values are close to the Ranz Marshall correlation. A refined correlation is consequently proposed, considering the diffusive part uniform on the droplet surface, whereas the convective part, decreasing from the leading edge to the trailing edge, was modelled by a cosinus term.

$$Sh(\theta) = 2 + 2 \times 0.3 \times \sqrt{Re} \cdot Sc^{1/3} \times (1 + \cos(\theta)) \tag{6.58}$$

The same correlation applies in case of the Nusselt number. The mass flux over the

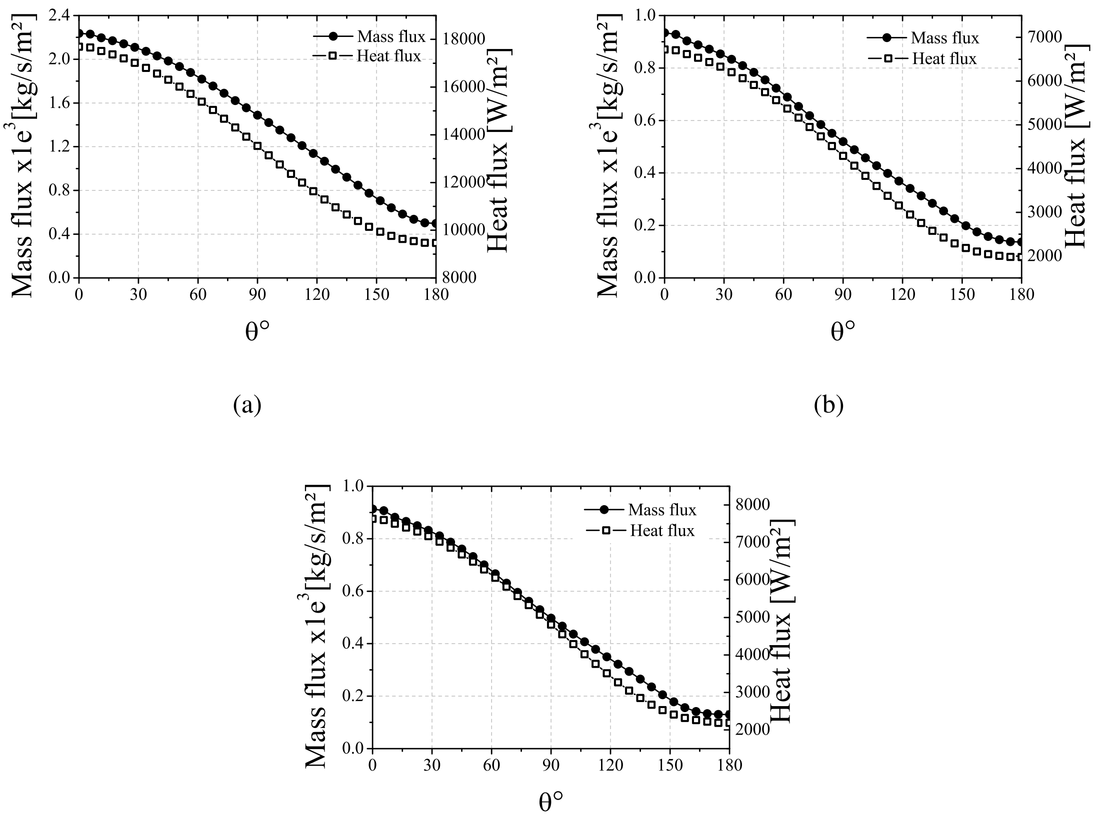

(a)

(b)

(c)

Figure 6.14: Calculated heat and mass fluxes of single droplet at different experimental parameters. a) liquid droplet of 100 μm and ambient air at 1 m/s and 40 °C. b) initial diameter is 500 μm and ambient air at 1 m/s and 40 °C. c) initial diameter is 500 μm and ambient air at 1 m/s and 10 °C.

droplet surface can be the calculated as:

$$\frac{dm}{dt}(\theta) = \pi D \rho_g \mathscr{D}_g B_M Sh(\theta) \tag{6.59}$$

For evaporation driven by the acoustic field, the Sherwood number proposed by (Yarin et al., 1999) will be used:

$$Sh(\theta) = 2 \cdot K_{ac} \frac{B}{(\omega \mathscr{D}_g)^{1/2}} \frac{\cos^2\theta}{(1+\cos^2\theta)^{1/2}} \tag{6.60}$$

6.3.5 Numerical implementation

An alternating direction implicit (ADI) scheme developed by Douglas and Gunn (1955) with a truncating error of 2nd order in time and spatial dimensions, was employed to

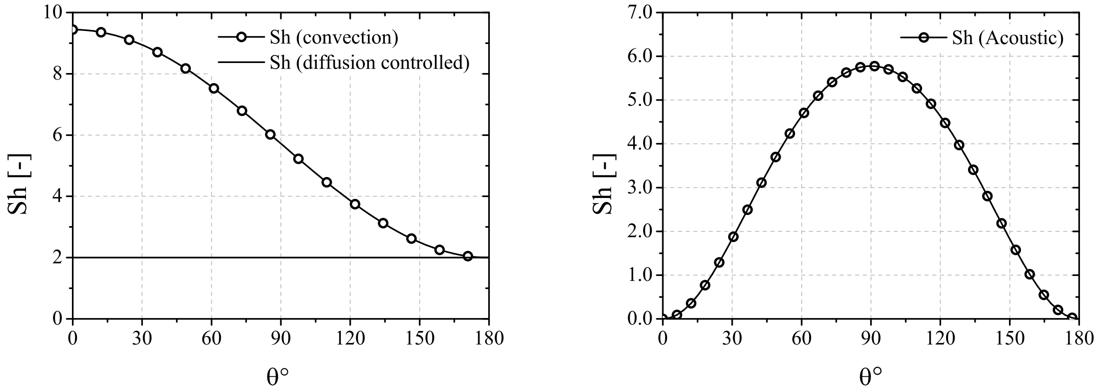

(a) (b)

Figure 6.15: Calculated Sh number according to a) eqn. (6.58), initial diameter is 1 mm and ambient air at 1 m/s and 25 °C. b) eqn. (6.60), initial diameter is 1 mm, SPL =162.5 dBe and air temperature = 25 °C.

find the distribution of solid concentration profiles. The governing eqn. (6.45) subject to the boundary conditions eqns. (6.49)-(6.52) can be expressed in a simpler form by introducing the following transformation, the time step is split into two sub-steps. In the first half time step, the system of equations are solved for each row (radial direction) of the grid points, while in the second half time steps the system of equations are solved for each column (azimuth direction) of grid points. The ADI process for the approximate solution of eqn. (6.43) (Carnahan et al., 1969, Moin, 2001) is:

$$
\begin{aligned}
(1 - S_2^i \delta_\theta^2)\, c_{i,j}^{(k+1/2)^*} &= (1 + S_1 \cdot \frac{1}{r_i^2} \delta_r^2)\, c_{i,j}^{k} \\
(1 - S_1^i \delta_r^2)\, c_{i,j}^{(k+1)} &= (1 - S_2^i \cdot \frac{1}{r_i^2} \delta_\theta^2)\, c_{i,j}^{(k+1/2)^*}
\end{aligned}
\qquad (6.61)
$$

in order to develop the numerical scheme eqn. (6.43) is transformed to the gird equation as follows:

r-terms

The second term of RHS of eqn. (6.45) is subjected to finite difference method:

$$
\begin{aligned}
\cdots &= \frac{\mathscr{D}_{ws}}{r_s^2 \xi^2} \frac{\partial}{\partial \xi} \left(\xi^2 \frac{\partial C_w}{\partial \xi} \right) + \cdots \\
\cdots &= \frac{\mathscr{D}_{ws}}{r_s^2} \left[\frac{2}{\xi} \frac{\partial C_w}{\partial \xi} + \frac{V_r r_s}{\mathscr{D}_{ws}} \frac{\partial C_w}{\partial \xi} + \frac{\partial^2 C_w}{\partial \xi^2} \right] + \cdots
\end{aligned}
\qquad (6.62)
$$

collect the similar terms in eqn. (6.62):

$$\cdots \quad = \quad \frac{\mathscr{D}_{ws}}{r_s^2}\Big[\Big(\frac{2}{\xi}+\frac{r_s}{\mathscr{D}_{ws}}V_r\Big)\frac{\partial dC_w}{\partial \xi}+\frac{\partial^2 C_w}{\partial \xi^2}\Big]+\cdots \tag{6.63}$$

A central difference scheme is applied to eqn. (6.62):

$$\cdots = \frac{\mathscr{D}_{ws}}{a_t^2}\left[\left(\frac{2}{\xi}+\frac{a_t}{\mathscr{D}_{ws}}V_r\right)\frac{c_{i+1}-c_{i-1}}{2\Delta\xi}+\frac{c_{i+1}-2c_i+c_{i-1}}{\partial \xi^2}\right]+\cdots \tag{6.64}$$

Multiplying eqn. (6.64) by $\frac{\Delta\xi^2\xi}{\Delta\xi^2\xi}$

$$\cdots = \frac{\mathscr{D}_{ws}}{a_t^2}\frac{1}{\Delta\xi^2\cdot\xi_i}\left[\Big(\Delta\xi+\gamma_{vr}\xi_i+\xi_i\Big)c_{i+1}-2\xi c_i+\Big(\xi_i-\gamma_{vr}\xi_i-\Delta\xi\Big)\,c_{i-1}\right] \tag{6.65}$$

where γ_{vr} is defined as:

$$\gamma_{vr} = \frac{r_s V_r}{2\cdot\mathscr{D}_{ws}}\Delta\xi \tag{6.66}$$

θ-terms

The same procedure applies in the θ direction and the final results reads:

$$\begin{aligned}\cdots = \frac{\mathscr{D}_{ws}}{r_s^2\Delta\theta^2}\frac{1}{\xi_i^2} \quad &\Big[\Big(1+cot(\theta_j)\frac{\Delta\theta}{2}+\gamma_{v\theta}\frac{\Delta\theta}{2}\Big)c_{j+1}-2c_i \\ &+\Big(1-\cot(\theta_j)\frac{\Delta\theta}{2}-\gamma_{v\theta}\frac{\Delta\theta}{2}\Big)c_{j-1}\Big]\end{aligned} \tag{6.67}$$

where γ_{vr} is defined as:

$$\gamma_{v\theta} = \frac{V_\theta r_s \xi_i}{\mathscr{D}_{ws}} \tag{6.68}$$

t-terms

The pseudo-convection terms results from coordinate transformation is given by:

$$\begin{aligned} \frac{\partial C_w}{\partial t} - \frac{\xi_i}{a_t^2} a_t \frac{da_t}{dt} \cdot \frac{dC_w}{d\xi} \\ \frac{(c^*_{i,j} - c_{i,j})}{\Delta t} - \frac{\xi_i}{2a_t^2}\frac{da_t^2}{dt} \cdot \frac{\partial C_w}{\partial \xi} \end{aligned} \tag{6.69}$$

From eqn. (4.34) the vapor flow across droplet surface is:

$$\dot{m}_v = -2\pi r_s K_L \tag{6.70}$$

where K_L defined as

$$K_L = \rho_g Sh B_m \mathscr{D}_g \tag{6.71}$$

but $\dot{m}_d = -\dot{m}_v$

$$\frac{4}{3}\pi\rho_d \frac{\partial a_t^3}{\partial t} = -2\pi a_t \cdot K_L \tag{6.72}$$

hence, rewrite eqn. (6.72) for $\frac{\partial a_t^2}{\partial t}$:

$$\frac{\partial a_t^2}{\partial t} = -\frac{K_L}{\rho_L} \tag{6.73}$$

and substitute back into eqn. (6.69):

$$\frac{(c^*_{i,j} - c_{i,j})}{\Delta t} - \frac{\xi}{2r_s^2} \cdot \frac{-K_L}{\rho_L} \cdot \frac{\partial C_w}{\partial \xi} \tag{6.74}$$

equations (6.65, 6.67 and 6.74) will be coupled according to ADI-scheme, eqn. (6.61), the first half time step will be implicit in θ direction and explecit in r direction:

$$\begin{aligned}
\frac{(c^*_{i,j}-c_{i,j})}{\Delta t/2} &= \frac{\xi}{2r_s^2}\cdot\frac{-K_L}{\rho_L}\cdot\frac{c^*_{i,j+1}-c^*_{i,j-1}}{\Delta\xi} \\
&+ \frac{\mathscr{D}_{ws}}{r_s^2}\frac{1}{\Delta\xi^2\cdot\xi_i}\left[\left(\Delta\xi+\gamma_{vr}\xi_i+\xi_i\right)c_{i+1}-2\xi c_i+\left(\xi_i-\gamma_{vr}\xi_i-\Delta\xi\right)c_{i-1}\right] \\
&+ \frac{\mathscr{D}_{ws}}{r_s^2\Delta\theta^2}\frac{1}{\xi_i^2}\left[\left(1+cot(\theta_j)\frac{\Delta\theta}{2}+\gamma_{v\theta}\frac{\Delta\theta}{2}\right)c^*_{i,j+1}-2c^*_{i,j}\right. \\
&\qquad\left.+\left(1-\cot(\theta_j)\frac{\Delta\theta}{2}-\gamma_{v\theta}\frac{\Delta\theta}{2}\right)c^*_{i,j-1}\right]
\end{aligned} \tag{6.75}$$

Multiplying eqn. (6.75) by $\xi_i^2\cdot\Delta t/2$ and collecting similar terms:

$$\begin{array}{ccc}
\left[-\mu_\theta\left(1+cot(\theta)\frac{\Delta\theta}{2}+\gamma_{v\theta}\frac{\Delta\theta}{2}\right)+KK_L\right]c^*_{i,j+1} & & \mu_r\xi\left[\left(\Delta\xi+\frac{a_tV_r}{2\mathscr{D}_{ws}}\Delta\xi\,\xi_i+\xi_i\right)c_{i+1}\right. \\
+\left(\xi_i^2+2\mu_\theta\right)c^*_{i,j}+ & = & -2\xi c_i \\
\left[-\mu_\theta\left(1-\cot(\theta)\frac{\Delta\theta}{2}-\gamma_{v\theta}\frac{\Delta\theta}{2}\right)+KK_L\right]c^*_{i,j-1} & & \left.+\left(\xi_i-\frac{a_tV_r}{2\mathscr{D}_{ws}}\cdot\Delta\xi\,\xi_i-\Delta\xi\right)c_{i-1}\right]
\end{array} \tag{6.76}$$

where

$$\begin{aligned}
\mu_r &= \frac{\mathscr{D}_{ws}}{a_t^2}\frac{\Delta t/2}{\Delta\xi^2} \\
\mu_\theta &= \frac{\mathscr{D}_{ws}}{a_t^2}\frac{\Delta t/2}{\Delta\theta^2} \\
KK_L &= \frac{\xi\Delta t/2K_L\xi_i^2}{2a_t^2\rho_L2\Delta\xi}
\end{aligned} \tag{6.77}$$

explicit θ, implicit r

Rewrite the first term of RHS of eqn. (6.75) for r-direction

$$\frac{\xi}{2r_s^2}\cdot\frac{-K_L}{\rho_d}\cdot\frac{c_{i+1,j}-c_{i+1,j}}{\Delta\xi} \tag{6.78}$$

multiply eqn. (6.75) by $\xi_i^2\cdot\Delta t/2$ and collect similar terms:

$$\begin{array}{ccc} \Big[-\mu_r\xi_i(\xi_i+\Delta\xi+\frac{\gamma_{v_r}}{2})+KK_L\Big]c_{i+1,j} & & \left[-\mu_\theta\left(1+cot(\theta)\frac{\Delta\theta}{2}+\gamma_{v\theta}\frac{\Delta\theta}{2}\right)\right]c^*_{i,j+1} \\ \Big[\xi_i^2+2\mu_r\xi_i^2\Big]c_{i,j} & = & +\left(\xi_i^2+2\mu_\theta\right)c^*_{i,j}+ \\ \Big[-\mu_r\xi_i(\xi_i-\Delta\xi-\frac{\gamma_{v_r}}{2})-KK_L\Big]c_{i-1,j} & & \Big[-\mu_\theta\Big(1-\cot(\theta)\frac{\Delta\theta}{2}-\gamma_{v\theta}\frac{\Delta\theta}{2}\Big)\Big]c^*_{i,j-1} \end{array} \tag{6.79}$$

Boundary conditions

The first set of boundary conditions for θ orientation at $\theta = 0$ $\theta = \pi$, the set of PDE will be solved for a half of the domain. Boundary conditions will be applied for both half-time steps i.e. implicit θ-explicit r ($\theta - r$ step) and implicit r-explicit θ ($r - \theta$ step). from eqn. (6.56) at $\theta = 0$, using central difference scheme

$$\begin{aligned} \frac{\partial c}{\partial \theta} &= \frac{c_{i,j+1}-c_{i,j-1}}{2\Delta\theta} = 0 \\ \Rightarrow &\quad c_{i,j+1} = c_{i,j-1} \end{aligned} \tag{6.80}$$

Substituting eqn. (6.80) into eqn. (6.76):

$$(\xi_i^2+2\mu_\theta)c^*_{i,j} - 2\mu_\theta c^*_{i,j+1} = \cdots \tag{6.81}$$

and substituting eqn. (6.80) into eqn. (6.79)

$$\cdots = (\xi_i^2-2\mu_\theta)c_{i,j} + 2\mu_\theta c_{i,j+1} \tag{6.82}$$

For $\theta = \pi$ eqn. (6.80) is substituted into eqn. (6.76) and eqn. (6.79), respectively:

$$2\mu_\theta c_{i,j-1} + (\xi_i^2+2\mu_\theta)c^*_{i,j} = \cdots \quad \text{implicit } \theta\text{-explicit } r \tag{6.83}$$

$$\cdots = -2\mu_\theta c_{i,j-1} + (\xi_i^2-2\mu_\theta)c_{i,j} \quad \text{implicit } r\text{-explicit } \theta \tag{6.84}$$

Two more boundary conditions are required in r-direction, the first one at $r = 0$, eqn. (6.49) is discretized using the central difference scheme:

$$\begin{aligned}\frac{\partial c_w}{\xi} &= \frac{c_{i+1,j} - c_{i-1,j}}{2\Delta\xi} = 0 \\ &\Rightarrow \quad c_{i+1,j} = c_{i-1,j} \end{aligned} \tag{6.85}$$

eqn. (6.85) is substituted into eqn. (6.76) and eqn. (6.79), respectively:

$$\cdots = (\xi_i^2 - 2\xi_i^2) c_{i,j} + 2\xi_i^2 \mu_r c_{i+1,j} \qquad \text{implicit } \theta\text{-explicit } r \tag{6.86}$$

$$-2\mu_r \xi_i^2 c_{i-1,j} + (\xi_i^2 + 2\xi_i^2 \mu_r) c_{i,j} = \cdots \qquad \text{implicit } r\text{-explicit } \theta \tag{6.87}$$

The second boundary condition results from the mass balance at droplet surface, eqn. (6.52). Applying central difference to eqn. (6.53) yields:

$$\begin{aligned}\frac{c_{i+1,j} - c_{i-1,j}}{2\Delta\xi} &= c_{i,j} \cdot A_t(\theta) - G_t(\theta) \\ \Rightarrow c_{i+1,j} - c_{i-1,j} &= 2\Delta\xi \cdot c_{i,j} \cdot A_t(\theta) - 2\Delta\xi \cdot G_t(\theta) \end{aligned} \tag{6.88}$$

For the the case implicit θ-explicit r, substitute eqn. (6.88) into eqn. (6.76)

$$\begin{aligned}\cdots &= \xi_i \mu_r \left(\xi_- \Delta\xi - \frac{\gamma_{vr}}{2} \right) c_{i-1,j} \\ &+ \xi_i^2 (1 - 2\mu_r) c_{i,j} \\ &+ \xi_i \mu_r \left(\xi_+ \Delta\xi + \frac{\gamma_{vr}}{2} \right) c_{i-1,j} \\ &+ 2\Delta\xi_i \cdot \xi_i A_t \mu_r \left(\xi_+ \Delta\xi + \frac{\gamma_{vr}}{2} \right) c_{i-1,j} \\ &- 2\Delta\xi_i \cdot \xi_i \mu_r \left(\xi_+ \Delta\xi + \frac{\gamma_{vr}}{2} \right) \cdot G_t \end{aligned} \tag{6.89}$$

rearrange eqn. (6.89) :

$$\begin{aligned}\cdots &= 2\xi_i^2 \mu_r c_{i-1,j} + \xi_i^2 (1 - 2\mu_r \cdot K A_t) c_{i,j} \\ &- 2\Delta\xi \, \xi_i \mu_r \left(\xi_+ \Delta\xi + \frac{\gamma_{V_r}}{2} \right) \cdot G_{term} \end{aligned} \tag{6.90}$$

where as for the case implicit r-explicit θ, eqn. (6.88) is substituted into eqn. (6.79):

$$\begin{aligned}
&- \left[\mu_r \xi_i (\xi_i + \Delta\xi + \frac{\gamma_{vr}}{2}) - KK_L\right] c^*_{i-1,j} \\
&- 2\Delta\xi A_t \left[\mu_r \xi_i (\xi_i \Delta\xi + \frac{\gamma_{vr}}{2}) - KK_L\right] c^*_{i,j} \\
&- \left[\mu_r \xi_i (\xi_i - \Delta\xi - \frac{\gamma_{vr}}{2}) + KK_L\right] c_{i-1,j} \\
&+ 2\Delta\xi \left[\mu_r \xi_i (\xi_i \Delta\xi + \frac{\gamma_{vr}}{2}) - KK_L\right] \cdot G_t \\
&+ \xi_i^2 (1 + 2\mu_r) c^*_{i,j} = \cdots
\end{aligned} \tag{6.91}$$

rearrange and collect similar terms:

$$-\mu_r \xi_i^2 \cdot c^*_{i-1,j} - \xi_i^2 \left[1 + 2\mu_r \cdot KA_t\right] c^*_{i,j} = 2\Delta\xi \left[\mu_r \xi_i (\xi_i \Delta\xi + \frac{\gamma_{vr}}{2}) - KK_L\right] \cdot G_t + \cdots \tag{6.92}$$

where KA_t:

$$KA_t = 1 - \Delta\xi A_t - \frac{\Delta\xi^2}{\xi} A_t - \frac{\Delta\xi}{\xi_i} \frac{\gamma_{V_r}}{2} \tag{6.93}$$

6.3.6 Accuracy and error criterion

The ADI-scheme accuracy is second order in the spatial orientation and time coordinate. The mass of solids is constant and a relative error of $1e^{-6}$ is maintained:

$$err = abs\left(\frac{M_{s0} - M_{st}}{M_{s0}}\right) \cdot 100\% \quad \lessapprox 1e^{-6} \tag{6.94}$$

6.4 Implementation for different boundary conditions

The solution of eqn. (6.45) applying the boundary conditions eqns. (6.56)-(6.47) will be solved for by considering the diffusion terms, and neglecting the advection part. The drying of droplets in the dynamic field and acoustic field will be presented. The model predicts the drying rate as well as the solid distribution profiles of both components

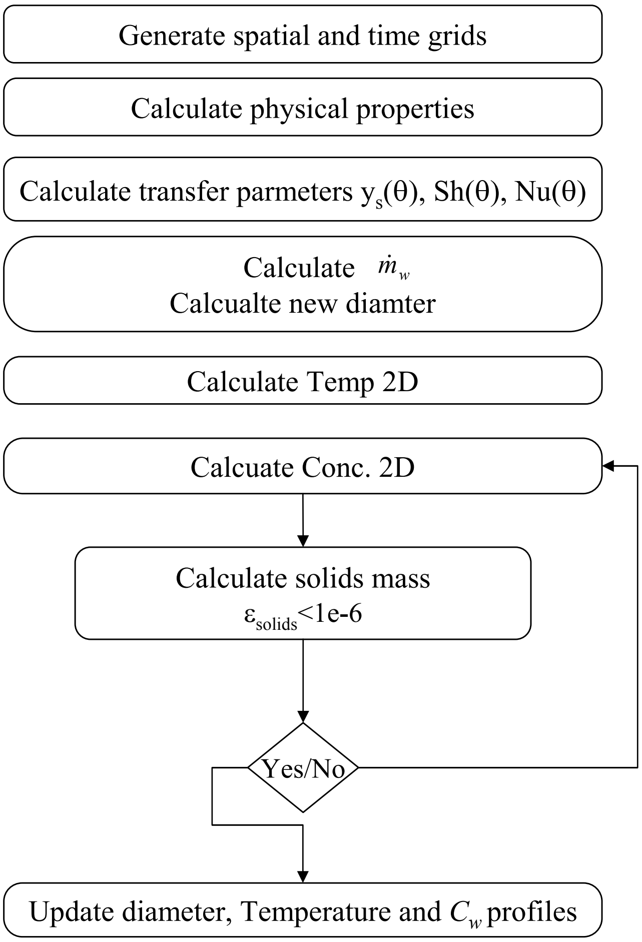

Figure 6.16: Flow diagram of the numerical scheme

and the solid concentration in radial direction and on the droplet surface i.e. azimuthal direction is calculated at every time step. The modeled droplet is an aqueous solution of Na_2SO_4 and water at 20% initial solids concentration.

6.4.1 Drying in a convective flow

In spray drying the droplet is moving down against the heated air. A relative velocity is assumed in the model which corresponds to the relative droplet velocity, and the temperature and the relative humidity can be set to any desired value. As depicted in fig. 6.17, the normalized droplet surface is plotted versus time. Using the D^2-Law, the evaporation rate β is calculated from the slope of the line. The evaporation of rate of multiphase droplet is lower compared to a pure liquid droplet of the same size. Using eqn. (4.37), $\beta = 4.459 \cdot 10^{-3} (mm^2/s)$, in terms of Peclet number (which is a dimensionless mass transport number that characterizes the relative importance of diffusion and convection), is defined as ratio of diffusive to convictive flow. A small Peclet number ($Pe = 3.5$), indicates the formation of full particle. The concentration of solid component at the droplet surface is calculated form $\theta = 0$ to the rear stagnation point $\theta = \pi$. Fig. 6.18-a shows the concentration profile at various time steps. It can clearly be seen that the highest concentration occurs at the front stagnation point, and as time proceeds, the solid concentration builds up. The radial distribution of the concentration is displayed in fig. 6.18-b. In this figure, the profiles are plotted at different time steps. It can be seen that the concentration of the solid component increased as it get closer to the surface.

The average solid concentration is depicted in fig. 6.17, and $C_{s,ave}$ is calculated at every time step using the following equation:

$$C_{s,ave} = \frac{1}{N_r} \sum_{r=0}^{r=R} \frac{\int_0^{2\pi} \int_0^{\pi} r^2 \cdot C_s(\theta) \sin(\theta) \partial\theta \partial\phi}{\int_0^{2\pi} \int_0^{\pi} r^2 \cdot \sin(\theta) \partial\theta \partial\phi} \tag{6.95}$$

where N_r is the number of radial grid points.

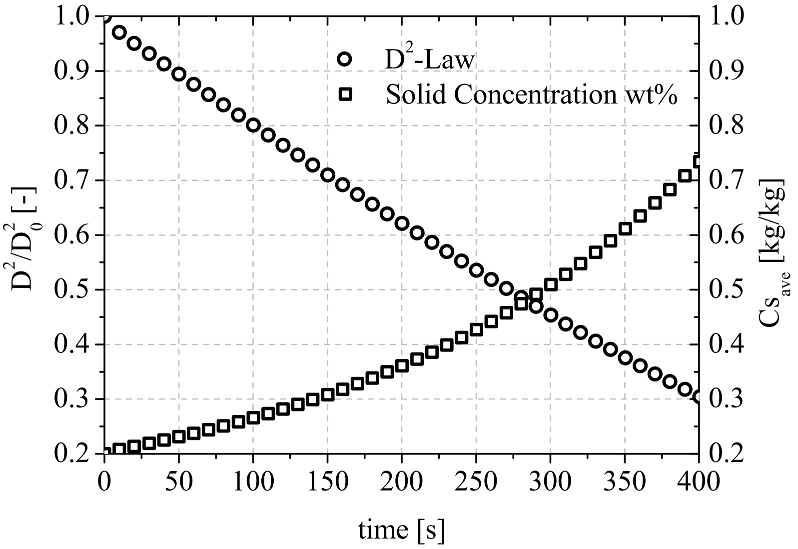

Figure 6.17: Normalized surface evolution of the droplet versus time, initial diameter = 1.0, $C_{s0} = 20\%$, the average solid concentration is calculated according to eqn. (6.95).

The radial concentration of the solid component is plotted in fig. 6.18b, representing the concentration gradient from the droplet center towards the surface. The calculation presented in fig. 6.18 shows the concentration profiles from $\tau = 0$ until $\tau = 1$, during

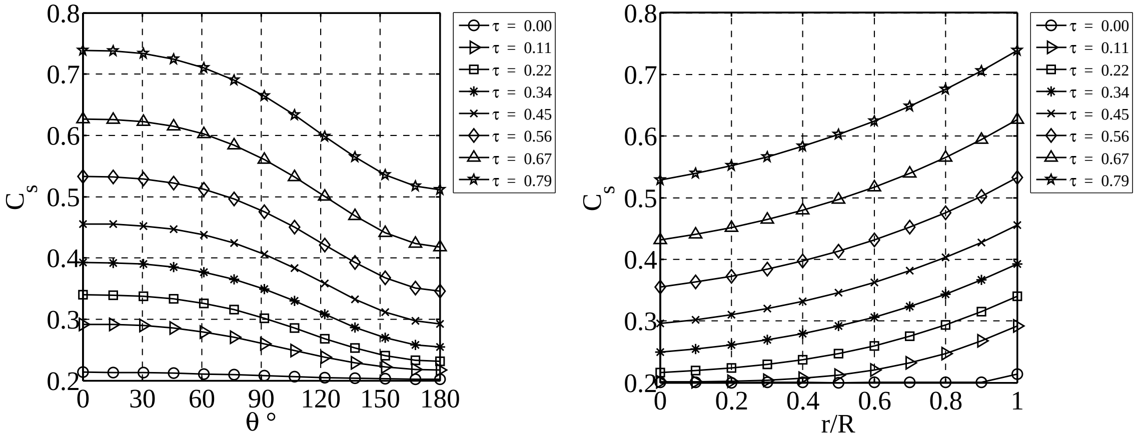

(a) Surface solid distribution (b) Radial solid distribution

Figure 6.18: Drying multiphase droplet of 20% initial concentration and diameter of 1.0 mm, Ambient gas temperature is 25 °C, concentration profiles are plotted at different time steps, τ.

the course of drying when almost the whole amount of the liquid is evaporated. The crust formation starts actually when the critical concentration in the stagnation point exceeds a critical value (saturation is reached), then concentration profiles over the surface become irrelevant.

A two-dimensional visualization of the concentration profiles is shown in fig. 6.19, where the drying profiles of the solid material show that the solid concentration builds up as the time proceeds. The air flow hits the droplet from the bottom; hence, the concentration is maximum at the front stagnation point and decreases as we move toward the rear stagnation point. The crust formation will start as soon as the surface concentration of solid material exceeds the critical concentration. Ford (1996) suggested that the formation of crust will start as soon as the first crust layer is 3 times larger than crystal size. In this 2-D model, the binary diffusion coefficient of the electrolyte material is set to a constant value of $9 \cdot 10^{-10}$, (Buchwald and Kaps, 1999). Results presented in fig. 6.20 are from another simulation run that was performed at an ambient gas temperature of 90 °C. Here, the evaporation rate is much faster that at an ambient temperature of 25 °C, calculated Pecelt number $Pe = 14.148$. According to Vehring et al. (2007) at larger Pecelt numbers the possibility of the formation of a hollow sphere is increased due to the increased of the evaporation rate of the droplet surface when compared to the convection inside the droplet.

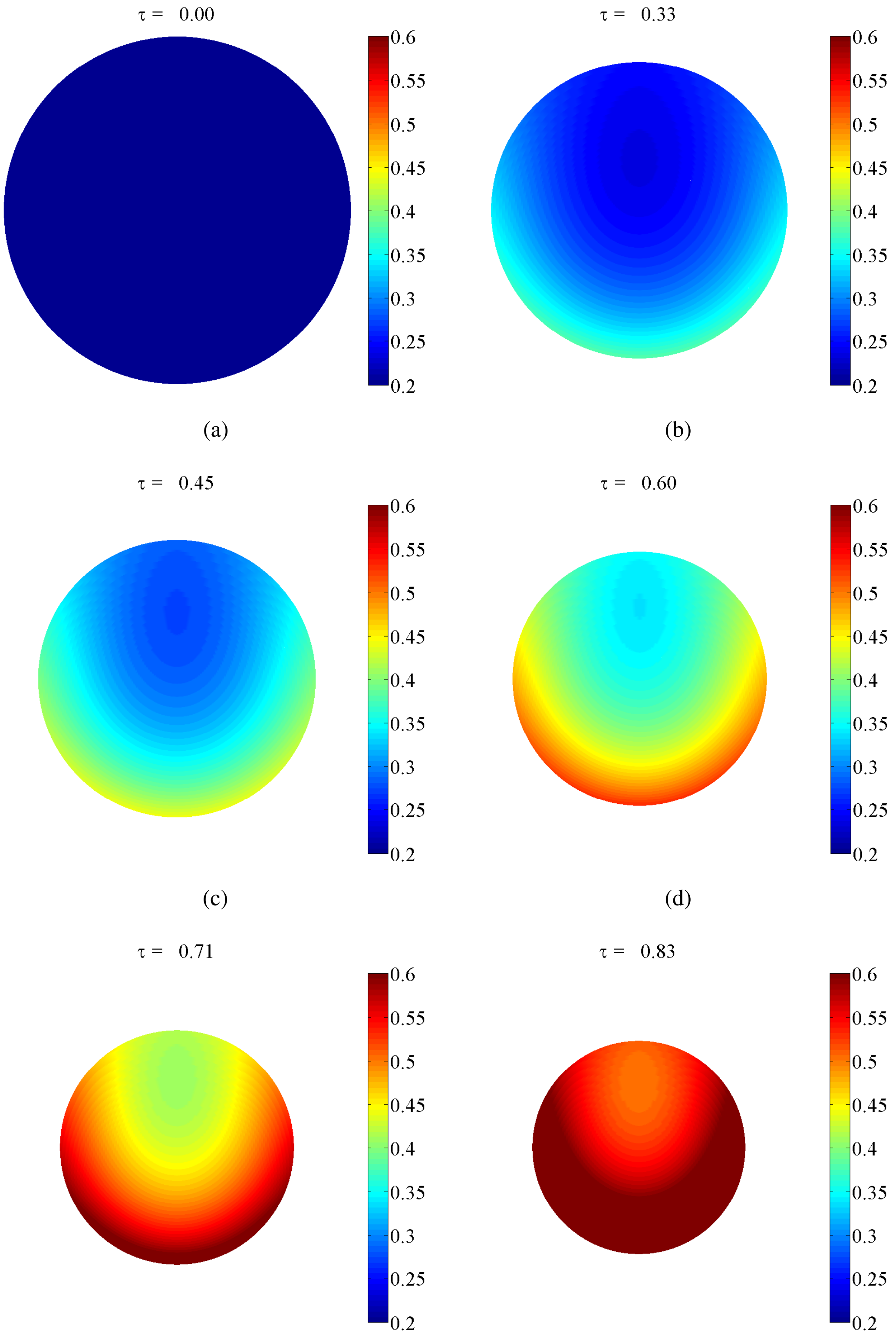

(a) (b) (c) (d) (e) (f)

Figure 6.19: Two-dimensional visualization of solid concentration over the droplet surface for a multiphase droplet of Na_2SO_4 aqueous droplet of 20% initial concentration, air velocity is 1 m/s and air temperature T_g = 25 °C.

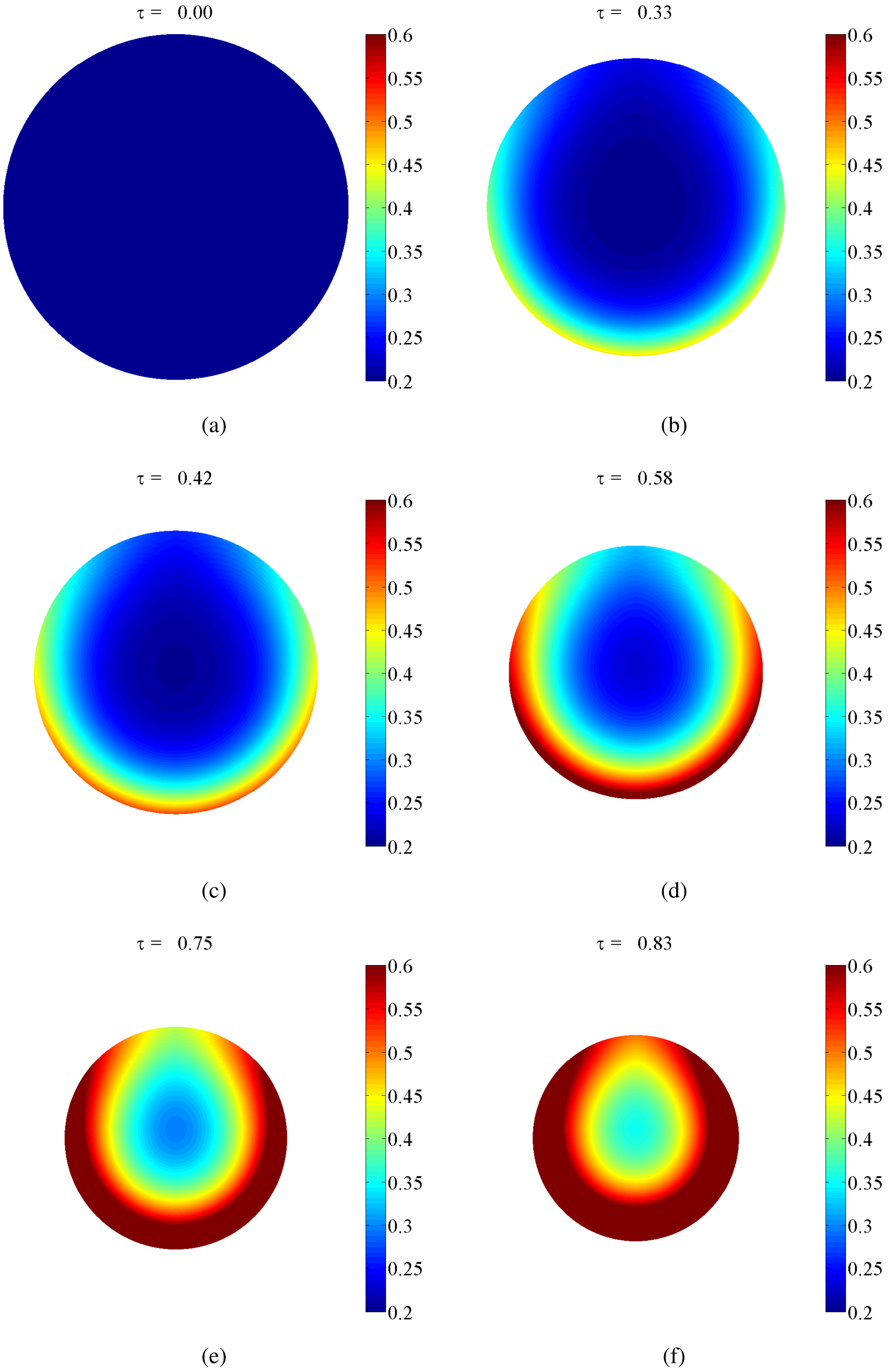

(a) (b) (c) (d) (e) (f)

Figure 6.20: Two-dimensional visualization of solid concentration over the droplet surface for a multiphase droplet of Na_2SO_4 aqueous droplet of 20% initial concentration, air velocity is 1 m/s and air temperature T_g = 90 °C.

6.4.2 Drying in the acoustic field

In the absence of air flow, the evaporation is driven by the inner acoustic streaming As displayed in fig. 6.21, the crystallization occurs first on the equator of the droplet then propagates towards the poles, where the maximum evaporation rated is at $\pi = 90$ degree. Yarin et al., derived the transfer parameters Sh and Nu number for the inner acoustic boundary layer. From his theory, it's expected that the maximum evaporation rate will occur near the equator of the droplet, this can be seen from fig. 6.21. When the transfer parameters eqn. (6.60), together with the boundary conditions, are imposed into eqn. (6.45), the concentration profile over the surface were calculated as displayed in fig. 6.22. The concentration profiles over droplet surface are plotted at different time steps, and the maximum concentration is calculated to be the maximum at $\theta = \pi/2$, which agrees with the experimental results obtained in fig. 6.21.

As depicted in fig. 6.22a, the normalized surface evolution of the droplet is calculated in the first drying period, i.e. constant rate period. The evaporation rate $\beta = 2.49 \cdot$

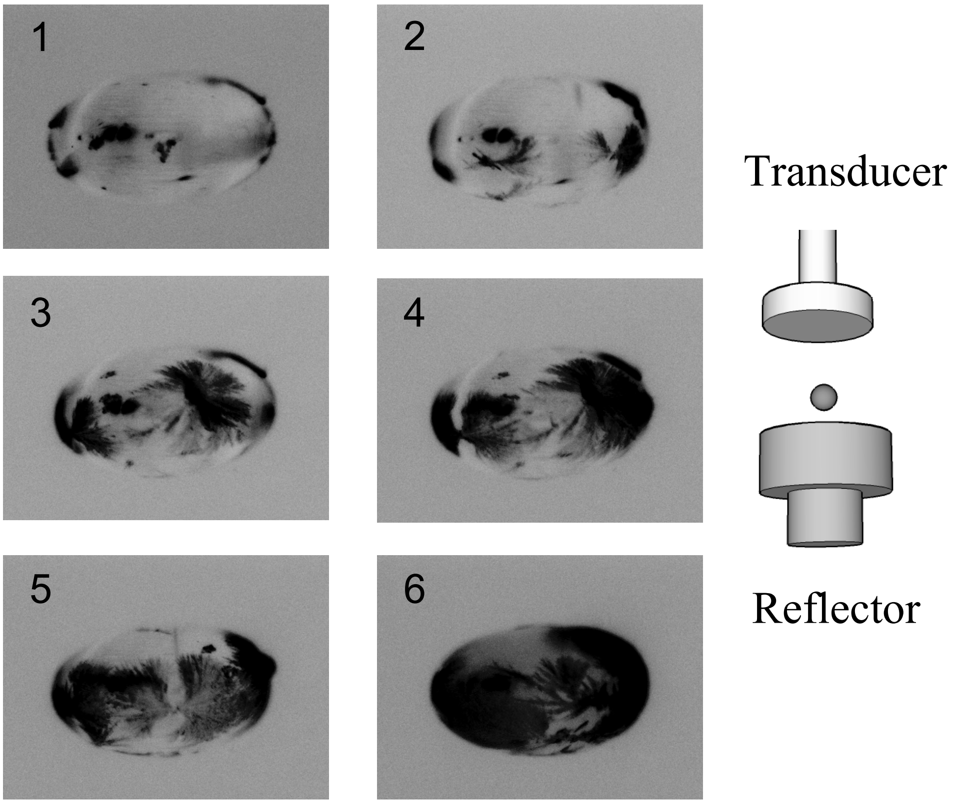

Figure 6.21: Crust formation of multiphase droplet, the evaporation here is driven by the acoustic inner boundary layer, the droplet volume is 1 μl and $SPL = 164.3$.

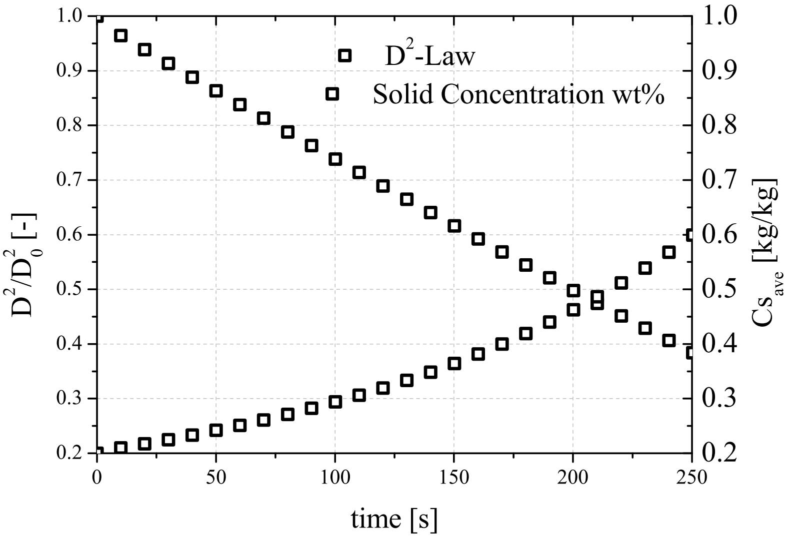

(a) Normalized surface evolution of the droplet versus time.

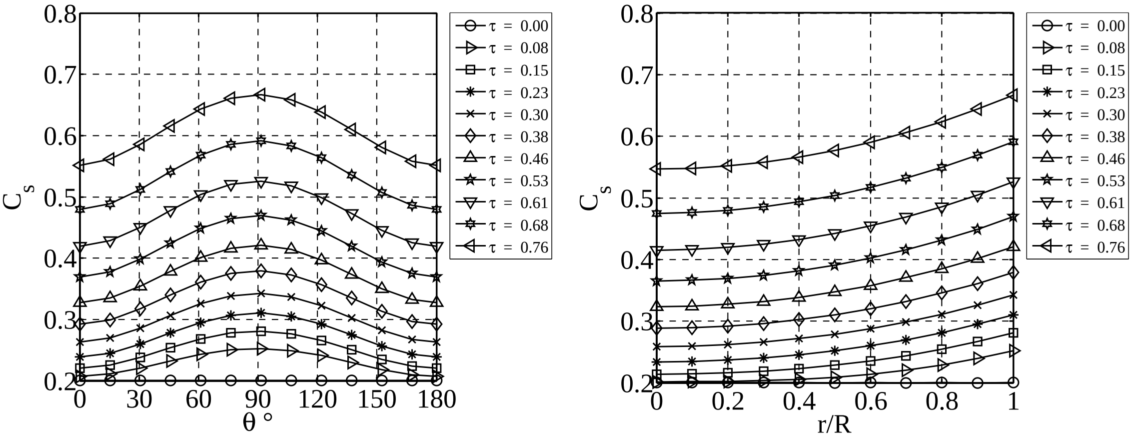

(b) Surface solid distribution. (c) Radial solid distribution.

Figure 6.22: Drying multiphase droplet of 20% initial concentration and diameter of 1.0 mm, Ambient gas temperature is 25 , $SPL_{eff} = 164.3$. a) Normalized surface evolution of the droplet versus time, The average solid concentration is calculated according to eqn. (6.95). b) Concentration profiles over droplet surface from $\theta = 0$ to $\theta = \pi$ and c) average radial concentration are plotted at different time steps, τ.

$10^{-3} mm^2/s$, and Pecelt number of 2. The concentration profiles in the radial direction are averaged over the surface at each radial shell, as depicted in fig. 6.22c, having made the assumption that no circulation is implemented, and the concentration of the solid component as well as the liquid will accumulate at each time step. The solid concentration will keep increasing. At the critical concentration the first crust layer forms. This denotes the end of the constant rate period, and the evaporation is now driven by the acoustic boundary layer and the crust resistance to vapor diffusion.

The drying model in the acoustic field serves only as a test for the model assumptions and parameters. The comparison with the experimental results obtained in the acoustic levitator serves as a validation of the model. In spray drying apparatus, CFD models are used to predict the whole drying process and the influence of each droplet on the evaporation of the neighbors drops or even the coagulation and agglomeration of small particles. Different models exist in the literature that attempt to simulate the 2-D or 3-D drying of bulk of droplets.

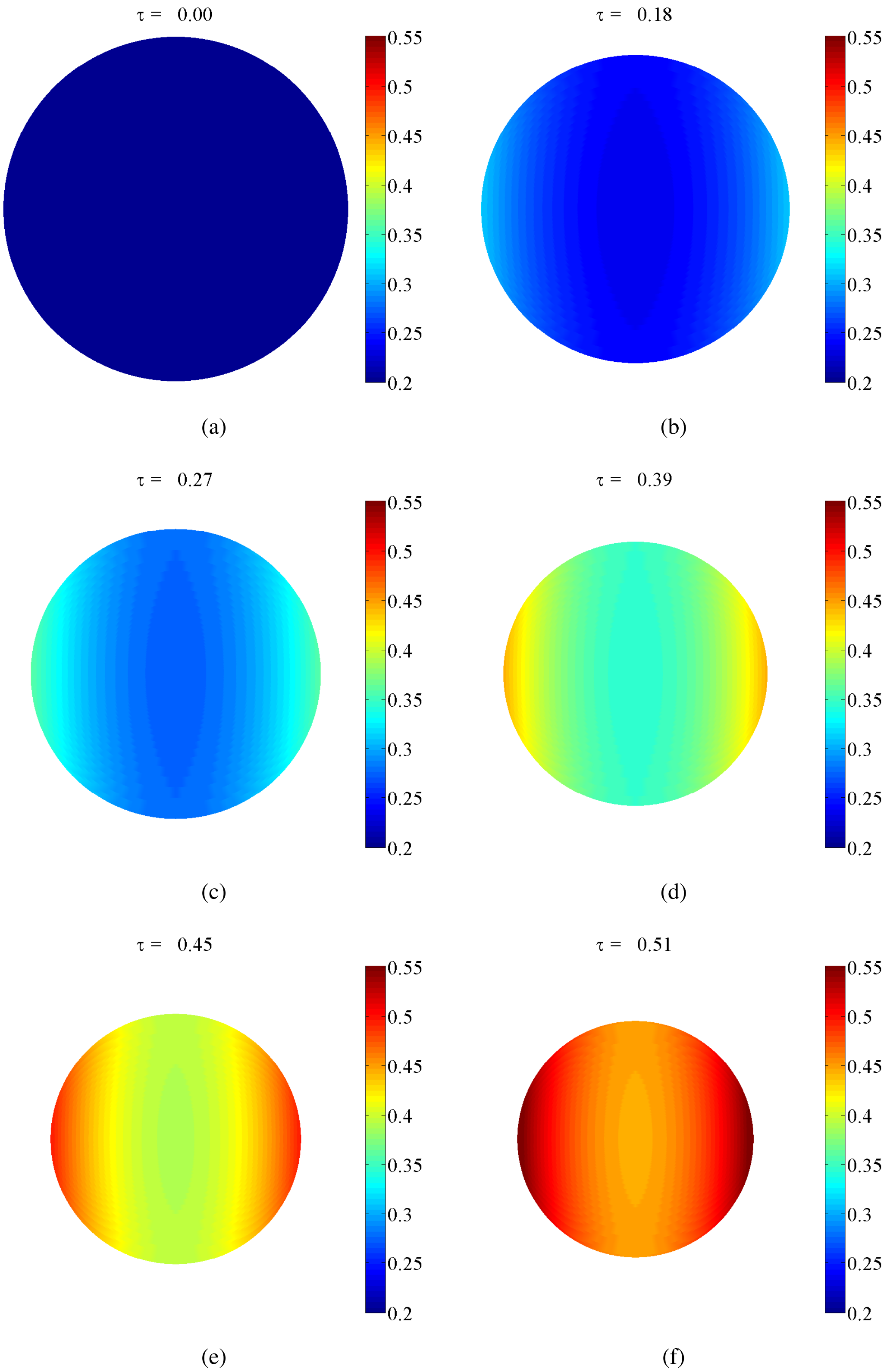

(a) (b) (c) (d) (e) (f)

Figure 6.23: Two-dimensional visualization of solid concentration over the droplet surface for a multiphase droplet of Na_2SO_4 aqueous droplet of 20% initial concentration. Air temperature T_g = 25 °C. SPL is 162.5 dBe.

Chapter 7

Conclusions

The aim of this thesis was to investigate the drying of single multiphase droplets under various process parameters. To accomplish this goal an experimental setup consisting of an acoustic levitator and other auxiliary units were used, due to its ability to levitate materials of different types, solids, liquids, multiphase droplets.

Experiments of pure liquid evaporation were performed to characterize the experimental setup and validate the existing models already published in the literature. Temporal evolution of normalized droplet surface and evaporation rate extracted from the meridian cross-section of the captured images during the droplet evaporation experiments serves to prepare a calibration curve to operate the acoustic leviator and to study the evaporation of droplets of pure liquids and compare them with the theoretical models that describe the evaporation in the acoustic field.

A comparison between evaporation in the acoustic levitator and another method called "drop on pin" that was implemented to study the evaporation and drying of single droplets reveals good agreement when the air velocity increased to the limit that destroys the inner acoustic streaming and the evaporation becomes a convective driven evaporation.

Next, the drying behavior of multiphase single droplets has been investigated. Using an aqueous solution of sodium sulfate. Experiments were conducted by varying the gas temperature, relative humidity and initial concentration of the solid content. Experimental results show the influence of the SPL on the drying rate. In order to achieve repeatable results, the applied acoustic force and the distance between the transducer and reflector were the same for all experiments.

The temporal evolution of the normalized surface show that the drying of multiphase droplets is divided into different drying stages; the constant rate period, when the diameter is decreasing. A classical D^2-law is used to describe this period. The second period is falling rate period; a shell is formed on the droplet surface and the diameter remains constant. The images fail to provide any information about the drying rate. The rise of the droplet in the acoustic field is used then to extract the drying rate in this period, this is a clear advantage of the acoustic levitator over other levitation techniques.

As the gas temperature is increased, the drying rate become higher and the constant rate period is shortened. However the size of the grain at the end of the drying process is identical. Higher relative humidities force the drying rate to become slower. Experiments with sodium sulfate show that the length of the constant rate period is a function of operating parameters and the initial concentration.

In addition, two other materials have been studied, skim milk and soya base. Both form a suspension when mixed with water. Results of drying show that drying kinetics can be estimated by a 1-D drying model, where the diffusion coefficient is a function of the solid material. The experiment in the acoustic levitator can be used to estimate the diffusion coefficient by fitting the drying curve and the predicted drying curves.

The morphological structure of the dried particle was investigated by the SEM technique. Images of the internal cross section of skim milk particles reveals a full particle formation at the end of the drying process. In the case of sodium sulfate, a crust is forming on the surface and ends up being a hollow particle.

In addition to experimental investigations, numerical models for evaporation and drying were developed, A classical D^2- law is used to predict the evaporation of pure liquid droplet. The validation of evaporation of pure liquids droplets when applying mass and heat transfer parameters developed by Yarin et al. reveals good agreement between theory and experiment when the ventilation of the outer acoustic streaming was applied.

A modified perfect mixing model to predict the drying rate and the crust thickness of the dried particles is presented. This model accounts for the crust resistance to the evaporation of the liquid. As the second drying stage begins, the crust thickness increases, the final crust thickness being dependent on the process parameters and mainly on the initial solid content.

A 2-D model was developed to describe the crust formation just before the end of the constant rate period when the solid concentration accumulates on the surface. The model assume a uniform diffusion coefficient in both orientation and solves for the concentration profiles along the radial and azimuthal directions.

Experimental results show that the crust initiates from the front stagnation point and propagate to the opposite pole. The crust will start to grow as soon as the mechanical stability is enough to hold. Crust formation depends on the flow direction of the drying gas. Experiments also provided an interesting validation of Yarin model that states that the inner acoustic streaming will lead to crust formation near the equator, as predicted by the mass and heat transfer model.

In summary, the acoustic levitator serves as suitable experimental set up for studying the drying kinetics of a single droplets. The possibility to vary process conditions helps to mimic the spray drying and to provide data for validation and development of new mathematical models.

Further development is suggested to improve the experimental setup in order to reach higher temperatures without harming the piezoceramic transducer. The coupling with drop-on-demand systems will enable to study the micro-encapsulation which arises as an important application in pharmaceutical or detergent industry.

Improving the 2-D mathematical model to account for the internal circulation in multiphase droplets is beneficial to improve the understanding of particle formation at various process parameters.

The predication of droplets morphological changes during the drying process for different operational parameters will help to improve a new design concepts for an engineered particle production, which enable to tailor the dried particles properties i.e. density, porosity, solubility and shape.

References

Abramzon, B. and Sirignano, W. A., *Droplet vaporization model for spray combustion calculations.* Int. J. Heat Mass Transfer, 32: 1605–1618, **1989**.

Adhikari, B., Howes, T., Bhandari, B., and Truong, V., *Experimental studies and kinetics of single drop drying and their relevance in drying of sugar-rich foods: A review.* International Journal of Food Properties, 3: 323–351, **2000**.

Audu, T. O. K. and Jeffreys, G. V., *The drying of drops of particulate slurries.* Trans. Instn. Chem. Engrs., 53: 165–172, **1975**.

Benenson, W., Harris, J., Stocker, H., and Lutz, H., Handbook of Physics. Springer, **2006**.

Bird, R. B., Stewart, W. E., and Lightfood, E. N., Transport Phenomena. Wiley International Edition, NewYork, **1960**.

Brenn, G., *Concentration fields in drying droplets.* Chem. Eng. Technol., 27, **2004**.

Brenn, G., Wiedemann, T., Rensink, D., Kastner, O., and Yarin, A. L., *Modeling and experimental investigation of the morphology of spray dryed particles.* Chem. Eng. Technol., 24: 1113–1116, **2001**.

Buchwald, A. and Kaps, C., *Zur Diffusion des Ionenpaares Na^+ und SO_4^{-2} in wassergesättigten Ziegelmaterialien Modellexperimente zur Mauerwerksentsalzung.* GDCH-Monographie, 15, **1999**.

Bücks, K. and Müller, H., *Über einige Beobachtungen an schwingenden Piezoquarzen und ihrem Schallfeld.* Zeitschrift für Physik, 84(1): 75–86, **1933**.

Cai, R. and Zhang, N., *Explicit analytical solutions of linear and nonlinear interior heat and mass transfer Equation Sets for Drying Process.* Journal of Heat Transfer, 125: 175–203, **2003**.

Carnahan, B., Luther, H. A., and Wilkes, J. O., Applied Numerical Methods. John Wiley & Sons, New York, **1969**.

Charlesworth, D. H. and Marshall, W. R., *Evaporation from droplets containing dissolved solids.* AIChE J., 6: 9–23, **1960**.

Chen, X. D. and Lin, S. X. Q., *Changes in milk droplet diameter during drying under constant drying conditions investigated using the glass-filament method.* Trans IChemE, Part C, Food and Bioproducts Processing, 82: 213–218, **2004**.

Chen, X. D. and Xie, G. Z., *Fingerprints of the drying behaviour of particulate or thin layer food materials established using a reaction engineering model.* Trans IChemE, 75: 213–222, **1997**.

Cheong, H. W., Jeffreys, G. V., and Mumford, C. J., *A receding interface model for the drying of slurry droplets.* AIChE Journal, 32: 1334–1346, **1986**.

Chung, J., *The motion of particles inside a droplet.* Journal of Heat Transfer, 104: 438–445, **1982**.

Crank, J., Free and Moving Boundary Problems. Clarendon Press, Oxford, **1984**.

Cussler, E. L., Diffusion Mass Transfer in Fluid Systems. Cambridge University Press, 2nd edition, **1997**.

Dalmaz, N., Ozbelge, H. O., Eraslan, A. N., and a, Y. U., *Heat and mass transfer mechanisms in drying of a suspension droplet: A new computational model.* Drying Technology, 25: 391–400, **2007**.

El-Sayed, T. M., Wallack, D. A., and King, C. J., *Changes in particle morphology during drying of drops of carbohydrate solutions and food liquids. 1. Effects of composition and drying conditions.* Ind. Eng. Chem. Res., 29, **1990**.

Eslamian, M., Ahmed, M., and Ashgriz, N., *Modelling of nanoparticle formation during spray pyrolysis.* Institute of Physics Publishing, Nanotechnology, 17: 1674–1685, **2006**.

Faeth, G. M., *Current status of droplet and liquid combustion.* Prog. Energy Combustion Sci., 3: 191–224, **1977**.

Farid, M., *A new approach to modelling of single droplet drying.* Chemical Engineering Science, 58: 2985–2993, **2003**.

Felder, R. M. and Rousseau, R. W., Elementary Principles of Chemical Processes. John Wiley & Sons. Inc., New York, **1986**.

Ferrari, G., Meerdink, G., and Walstra, P., *Drying kinetics for a single droplet of skim-milk.* Journal of Food Engineering, 10: 215–230, **1989**.

Ford, I., *Models of crystallisation in evaporating droplets.* Thermodynamics and Kinetics of Phase Transformations, Materials Research Society Symposium Proceedings, 398: 637–642, **1996**.

Frackowiak, B., Approche experimentale et simulation numeerique des effets dínteractions entre gouttes en evaporation. Ph.D. thesis, Auditorium de lÓNERA Centre de Toulouse,, **2007**.

Frey, D. D. and King, C. J., *Experimental and theoretical investigation of foam-spray drying. 2. Experimental investigation of volatiles loss during foam-spray drying.* Industrial & Engineering Chemistry Fundamentals, 25: 730–735, **1986**.

Frössling, N., *Über die Verdunstung fallender Tropfen.* Gerlands Beitr. Geophys, 52: 170–216, **1938**.

Fuchs, N. A., The Mechanics of Aerosols. Pergamon Press, New York, **1964**.

Furuta, T., Okazaki, M., Toei, R., and Crosby, E. J., *Formation of crystals on the surface of non-supported droplet in drying.* In “International Drying Symposium,” pages 157–164. Hemisphere-McGraw-Hill:New York, **1982**.

Gekas, V., Transport Phenomena of Foods and Biological Materials. CRC Press, Boca Raton, **1992**.

Handscomb, C., Kraft, M., and Bayly, A., *A new model for the drying of droplets containing suspended solids after shell formation.* Chemical Engineering Science, 64(2), **2008**.

Hecht, J. P. and King, C. J., *Spray drying: Influence of developing drop morphology on drying rates and retention of volatile substances. 1. Single-drop experiments.* Ind. Eng. Chem. Res., 39: 1756–1765, **2000**.

Incropera, F. P. and Dewitt, D. P., Fundamentals of Heat and Mass Transfer. John Wiley & Sons, New York, 4th edition, **1996**.

Jaeschke, L., *Mechanismus der Feuchtigkeitsbewegung bei der Trocknung von Gütern mit verkrustenden OberflÄchen.* Chem. Ing. Tech., 36: 449–455, **1964**.

Kastner, O., Theoretische und experimentelle Untersuchungen zum Stoffübergang von Einzeltropfen in einem akustischen Rohrlevitator. Ph.D. thesis, Universität Erlangen-Nürnberg, **2001**.

Kastner, O., Brenn, G., Rensink, D., and Tropea, C., *Mass transfer from multiple droplets during drying in a tube levitator.* In “International Conference on Liquid Atomization and Spray Systems,” Pasadena, CA, USA, **2000**.

Kastner, O., Brenn, G., Rensink, D., and Tropea, C., *The acoustic tube levitator: A novel device for determining the drying kinetics of single droplets.* Chem. Eng. Technol., 24: 335–339, **2001**.

Keey, R. B., Drying, Principles and Practice. Pergamon Press, **1972**.

King, L., *On the acoustic radiation pressure on spheres.* Proc. Roy. Soc., 147: 212–240, **1934**.

Kuts, P., Strumillo, C., and Zbicinski, I., *Evaporation kinetics of single droplets containing dissolved biomass.* Drying Technology, 14: 2041 – 2060, **1996**.

Law, C. K., *Recent advances in droplet vaporisation and combustion.* Prog. Energy Combustion Sci., 8(3): 171–201, **1982**.

Lee, A. and Law, C. K., *Gasification and shell characteristics in slurry droplet burning.* Combustion and Flame, 85: 77–93, **1991**.

Lee, C. P., Anilkumar, A. V., and Wang, T. G., *Static shape and instability of an acoustically levitated liquid drop.* Phys. Fluids, 3(11), **1991**.

Lierke, E., *Vergleichende Betrachtungen zur berührungslosen Positionierung von Einzeltropfen in aerodynamischen, akustischen und elektrischen Kraftfeldern.* Engineering Research, 61: 201–215, **1995**.

Lierke, E., *Akustische Positionierung Ein umfassender überblick über Grundlagen und Anwendungen.* Acustica, 82: 220–237, **1996**a.

Lierke, E., *Kontrollierte Massenänderung von Tropfen in einem akustischen Stehwellen Positionierer.* Engineering Research, 62: 20–30, **1996**b.

Lin, J.-C. and Gentry, J. W., *Spray drying drop morphology: Experimental study.* Aerosol Science and Technology, 37: 15–32, **2003**.

Lin, S. X. and Chen, X. D., *Improving the glass filament method for accurate measurement of drying kinetics of liquid droplets.* Trans IChemE, 80: 401–410, **2002**.

Luikov, A. V., *Systems of differential equations of heat and mass transfer in capillary-porous bodies (review).* International Journal of Heat and Mass Transfer, 18: 1–14, **1975**.

Masters, K., Spray Drying Handbook. Longman Scientific & Technical, Essex, Great Britain, **1991**.

Mezhericher, M., Levy, A., and Borde, I., *Theoretical drying model of single droplets containing insoluble or dissolved solids.* In “15th International Drying Symposium (IDS 2006),” Budapest, Hungary, **2006**.

Miura, K., Miura, T., and Ohtani, S., *Heat and mass transfer to and from droplets.* AIChE Symp. Ser., 73(163): 95–102, **1977**.

Moeser, C., Groenewold, C., Groenewold, H., and Tsotsas, E., *Untersuchung der Kinetik von Trennprozessen im akustischen Levitator: Vor- und Nachteile.* Chemie Ingenieur Technik, 73: 1012–1017, **2001**.

Moin, P., Fundamentals of Engineering Numerical Analysis. Cambridge University Press, London, **2001**.

Mujumdar, A., Handbook of Industrial Drying. CRC Press, New York, 3rd edition, **2006**.

Nesic, S. and Vodnik, J., *Kinetics of droplet evaporation.* Chemical Engineering Science, 46: 527–537, **1991**.

Nonhebel, G. and Moss, A. A. H., Drying of Solids in the Chemical Industry. Butterworths, **1971**.

Ranz, W. E. and Marshall, J. R., *Evaporation from drops 1.* Chem. Eng. Progr., 48: 141–146, **1952**a.

Ranz, W. E. and Marshall, J. R., *Evaporation from drops 2.* Chem. Eng. Progr., 48: 173–180, **1952**b.

Rensink, D., Verdunstung akustisch levitierter schwingender Tropfen aus homogenen und heterogenen Medien. Ph.D. thesis, Universität Erlangen-Nürnberg, Technischen Fakultät, **2004**.

Rohling, O., Weitkamp, C., and Neidhart, B., *Experimental setup for the determination of analytes contained in ultrasonically levitated drops.* Fresenius J. Anal. Chem., 368: 125–129, **2000**.

Sacher, S. and Krammer, G., *Untersuchung von Kristallisationsprozessen in einem Ultraschal-Levitator.* Chemie Ingenieur Technik, 77, **2005**.

Sano, Y. and Keey, R. B., *The drying of a spherical particle containing colloidal material into a hollow sphere.* Chemical Engineering Science, 37: 881–889, **1982**.

Schiffter, H. and Lee, G., *Single-droplet evaporation kinetics and particle formation in an acoustic levitator. part 1: Evaporation of water microdroplets assessed using* *boundary-layer and acoustic levitation theories.* Journal of Pharmaceutical Sciences, 96(9): 2274–2283, **2007**a.

Schiffter, H. and Lee, G., *Single-droplet evaporation kinetics and particle formation in an acoustic levitator. part 2: Drying kinetics and particle formation from microdroplets of aqueous mannitol, trehalose, or catalase.* Journal of Pharmaceutical Sciences, 96(9): 2284–2295, **2007**b.

Schiffter, H. A., Single droplet drying of proteins and protein formulations via acoustic levitation. Ph.D. thesis, Friedrich-Alexander-University Nuremberg-Erlangen, Department of Pharmaceutical Technology, **2005**.

Schlichting, H., Boundary Layer Theory. McGraw-Hill, Inc., **1978**.

Schoeber, W. A. H., Regular regime in sorption processes. Ph.D. thesis, University of Eindhoven, **1976**.

Schuck, P., *Spray drying of dairy products: State of the art.* 1st International Symposium on Spray Drying of Milk Products, 82: 375–382, **2002**.

Sckuhr, S. P. W., Simulation des thermodynamischen Verhaltens von Lackpartikeln bei der Spritzapplikation. Ph.D. thesis, TU Darmstadt, **2001**.

Seydel, P., Sengespeick, A., Blömer, J., and Bertling, J., *Experiment and mathematical modeling of solid formation at spray drying.* Chemical Engineering & Technology, 27: 505 – 510, **2004**.

Shabde, V. S., Emets, S. V., Mann, U., Hoo, K. A., Carlson, N. N., and Gladysz, G. M., *Modeling a hollow micro-particle production process.* Computers & Chemical Engineering, 29: 2420–2428, **2005**.

Sirignano, W. A., Fluid Dynamics and Transport of Droplets and Sprays. Cambridge University Press, **1999**.

Sloth, J., Kiil, S., Jensen, A. D., Andersen, S. K., Jorgensen, K., Schiffter, H., and Lee, G., *Model based analysis of the drying of a single solution droplet in an ultrasonic levitator.* Chemical Engineering Science, 61: 2701–2709, **2006**.

Strutt, J. W., Rayleich, B., D, S., and S., F. R., The Theory of Sound. Dover Publications, 2nd edition, **1945**.

Sunkel, J. M. and King, C. J., *Influence of the development of particle morphology upon rates of loss of volatile solutes during drying of drops.* Ind. Eng. Chem. Res., 32: 2357–2364, **1993**.

Tian, Y. and Apfel, R., *A novel multiple drop levitator for the study of drop arrays.* Journal of Aerosol Science, 27: 721–737, **1996**.

Trinh, E. H., Holt, R. G., and Thiessen, D. B., *The dynamics of ultrasonically levitated drops in an electric field.* Phys. Fluids, 8(1): 43–61, **1996**.

Trinh, H. E. and Hsu, C.-J., *Equilibrium shapes of acoustically levitated drops.* J. Acoust. Soc. Am., 79: 1335–1338, **1986**.

Tuckermann, R., Gase, Aerosole, Tropfen und Partikel in stehenden Ultraschallfeldern: Eine Untersuchung zur Anreicherung schwerer Gase, Verdampfung levitierter Tropfen, Kristall- und Partikelbildung. Ph.D. thesis, Technischen Universität Carolo-Wilhelmina Gemeinsamen Naturwissenschaftlichen Fakultät, **2002**.

Vehring, R., *Pharmaceutical particle engineering via spray drying.* Pharmaceutical Research, 25: 999–1022, **2007**.

Vehring, R., Foss, W. R., and Lechuga-Ballesteros, D., *Particle formation in spray drying.* Journal of Aerosol Science, 38: 728–746, **2007**.

Verdurmen, R. E., Verschueren, M., Gunsing, M., Straatsma, H., Blei, S., and Sommerfeld, M., *Simulation of agglomeration in spray dryers: The EDECAD project.* Drying Technology, 22: 1403–1461, **2004**.

Wallack, D. A., El-Sayed, T. M., and King, C. J., *Changes in particle morphology during drying of drops of carbohydrate solutions and food liquids. 2. Effects on drying rate.* Ind. Eng. Chem. Res., 29: 2354–2357, **1990**.

Weber, J. K. R., Hampton, D. S., Merkley, D. R., Rey, C. A., Zatarski, M. M., and Nordinea, P. C., *Aero-acoustic levitation: A method for containerless liquid-phase processing at high temperatures.* Rev. Sci. Instrum., 65(2): 456–465, **1993**.

Welter, E. and Neidhart, B., *Acoustically levitated droplets : A new tool for micro and trace analysis.* Fresenius J. Anal. Chem., 357: 345–350, **1997**.

Wijlhuizen, A. E., Kerkhof, I. A. M., and Bruin, S., *Theoretical study of the inactwation of phosphatase during spray drying of skim-milk.* Chemical Engineering Science, 34: 651–660, **1979**.

Wilms, J., Evaporation of Multicomponent Droplets. Ph.D. thesis, Universität Stuttgart, Fakultät für Luft- und Raumfahrttechnik und Geodäsie, **2005**.

Xie, W. J., Cao, C. D., Lü, Y. J., and Wei, B., *Levitation of Iridium and Liquid Mercury by Ultrasound.* Physical Review Letters, 89: 1–4, **2002**.

Xie, W. J. and Wei, B., *Parametric study of single-axis acoustic levitation.* Applied Physics Letters, 79: 881–883, **2001**.

Yarin, A., Brenn, G., Kastner, O., Rensink, D., and Tropea, C., *Evaporation of acoustically levitated droplets.* Fluid Mech., 399: 151–204, **1999**.

Yarin, A. L., Brenn, G., and DirkRensink, *Evaporation of acoustically levitated droplets of binary liquid mixtures.* International Journal of Heat and Fluid Flow, 23: 471–486, **2002**a.

Yarin, A. L., Brenn, G., Kastner, O., and Tropea, C., *Drying of acoustically levitated droplets of liquid-solid suspensions: Evaporation and crust formation.* Phys. Fluids, 14(7): 2289–2298, **2002**b.

Yarin, A. L., Brenn, G., Keller, J., Pfaffenlehner, M., Ryssel, E., and Tropea, C., *Flow-field characteristics of an aerodynamic acoustic levitator.* Phys. Fluids, 9(11): 3300–3314, **1997**.

Yarin, A. L., Pfaffenlehner, M., and Tropea, C., *On the acoustic levitation of droplets.* Fluid Mech., 356: 65–91, **1998**.

Zaitone, B., Frackowiak, B., and Tropea, C., *Drying of multiphase single droplets: two dimensional modelling*. In “16th International Drying Symposium,” Hyderabad, India, **2008**.

Zaitone, B., Hunsmann, S., Castanet, G., Damaschke, N., Ebert, V., and Tropea, C., *Evaporation of acoustically levitated droplets.* In “10th International Congress on Liquid Atomization and Spray Systems,” Kyoto, Japan, **2006**.

List of Figures

List of Tables

Appendix A

Property Data

Latent heat of vaporaisation

Latent heat of vaporisation L_v [kJ/kg] for water is calculated by :

$$\begin{aligned} L_v = & - 1.82631 \cdot 10^{-10} \cdot T(K)^5 + 3.36188 \cdot 10^{-7} \cdot T(K)^4 \\ & - 2.61892 \cdot 10^{-4} \cdot T(K)^3 + 1.03636 \cdot 10^{-1} \cdot T(K)^2 \\ & - 2.27549 \cdot T(K) + 4727.58 \end{aligned}$$

Saturation pressure

Vapor pressure for water and other liquids will be calculated using Antoine equation (Reid et al. 1987):

$$P^* = 133.0 \cdot \exp\left(A - \frac{B}{C + T(K)}\right) \qquad [\text{Pa}]$$

physical property	material	A	B	C
Vapor pressure P^*	Water	18.3036	3816.44	-46.13
	Ethanol	18.9119	3803.98	-41.68
	Methanol	18.5875	3626.55	-34.29

physical property	material	used correlation
Density, [kg/m^3]	Water	$\rho = -2.59286 \cdot 10^{-9} \cdot T(K)^5 + 3.848926 \cdot 10^{-6} \cdot T(K)^4 - 2.24256 \cdot 10^{-3} \cdot T(K)^3 + 6.34677 \cdot 10^{-1} \cdot T(K)^2 - 86.2753 \cdot T(K) + 5431.3$
	Ethanol	$\rho = -1.40223 \cdot 10^{-5} \cdot T(K)^3 + 1.23254 \cdot 10^{-2} \cdot T(K)^2 - 4.44571 \cdot T(K) + 1.38634e03$
	Methanol	$\rho = -1.94786 \cdot 10^{-5} \cdot T(K)^3 + 1.85736 \cdot 10^{-2} \cdot T(K)^2 - 6.82465 \cdot T(K) + 1687.39$
Liquid heat capacity, [kJ/kg.K]	Water	$C_p = 8.08081 \cdot 10^{-8} \cdot T(K)^3 - 6.95948 \cdot 10^{-5} \cdot T(K)^2 + 1.9734 \cdot 10^{-2} \cdot T(K) + 2.34527$
	Ethanol	$C_p = 1.57289 \cdot 10^{-7} \cdot T(K)^3 - 1.2474 \cdot 10^{-4} \cdot T(K)^2 + 4.34267 \cdot 10^{-2} \cdot T(K)^{-3} - 3.54314$
	Methanol	$C_p = 1.43333 \cdot 10^{-5} \cdot T(K)^2 - 2.66697 \cdot 10^{-3} \cdot T(K) + 2.04506$
Diffusion coefficient, [m^2/s]	Water	$\mathscr{D} = 0.1237565348 \cdot 10^{-3} \cdot \frac{T(K)^{1.75}}{P(pa)}$
	Ethanol	$\mathscr{D} = 5.8516 \cdot 10^{-5} \cdot \frac{T(K)^{1.75}}{P(pa)}$
	Methanol	$\mathscr{D} = 18.102 \cdot 10^{-6} \cdot \frac{T(K)^2}{P(pa)}$

Solid materials properties

Material properties for solid materials at 25 °C. (Wijlhuizen et al., 1979), (DETHERM Dechema)

material	density [kg/m^3]	heat capacity [kJ/kg/K]	heat conductivity [w/m/K]
Na_2SO_4	2680	3.5-4.2	0.6
Skim milk	1520	3.854	0.21
Soyabase	1165	3.354	0.25

Curriculum Vitae

Personal data

Name	Belal Ali Al Zaitone
Date of Birth	April 20, 1979
Place of Birth	Souf, Jordan
Nationality	Jordanian
Marital status	Single

Education

2005–2009	Doctoral research Technischen Universität Darmstadt, Darmstadt, Germany
2002–2005	M.Sc. in Chemical Engineering Universität Erlangen-Nürnberg, Erlangen, Germany
1997 – 2002	B.Sc. in Chemical Engineering University of Jordan, Amman, Jordan
1996 – 1997	High School: Souf Secondary School
1985 – 1996	Primary School